Description and simulation of the physics of Resistive Plate Chambers

Vincent Français

To cite this version:

Vincent Français. Description and simulation of the physics of Resistive Plate Chambers. Nuclear Experiment [nucl-ex]. Université Clermont Auvergne [2017-2020], 2017. English. ⟨NNT : 2017CLFAC035⟩. ⟨tel-01727712⟩

HAL Id: tel-01727712
https://theses.hal.science/tel-01727712v1

Submitted on 9 Mar 2018

Numéro d'ordre: 2822 PCCF T 1704

UNIVERSITÉ CLERMONT AUVERGNE
U.F.R. Sciences et Technologies

ECOLE DOCTORALE DES SCIENCES FONDAMENTALES
N^{o} 913

THÈSE
présentée pour obtenir le grade de

Docteur d'Université
SPÉCIALITÉ : PHYSIQUE DES PARTICULES

par

Vincent Français

Description and simulation of the physics of Resistive Plate Chambers

Soutenue publiquement le 4 juillet 2017, devant la commission d'examen :

Président :	Pascal ANDRE	
Examinateurs :	Didier MIALLIER	Directeur
	Alessandro FERRETI	Rapporteur
	Georges VASILEIADIS	Rapporteur
	Djamel BOUMEDIENE	
	Laurent MIRABITO	
	Lydia MAIGNE	
	Fabienne LEDROIT	

Sixty percent of the time, it works all the time.
A very wise man

Remerciements

Ces remerciements seront courts et concis, un peu à l'image de cette thèse. Pas besoin d'un long discours pour dire ce qui est évident.

Je tiens à remercier tout particulièrement Alain Falvard sans qui cette thèse n'aurait jamais pu aboutir, ainsi que Djamel-Eddine Boumediene pour son aide.

Je remercie aussi les amis, sans les citer, ils se reconnaitront tous.

Bien sûr mes pensées vont à ma chère et tendre qui m'a supporté et soutenu pendant les périodes fastidieuses de la rédaction de cette thèse.

Enfin je remercie la Mama et la Tata qui sont bourrées mais qu'on aime bien quand même !

Abstract

The 20th century saw the development of particle physics research field, with the fundation of the famous Standard Model of particle physics. More specifically during the past 70 years numerous particles have been detected and studied. Alongside those discoveries, the experimental means and detectors has greatly evolved. From the simple Gargamel bubble chamber, which lay the first brick to the Standard Model theory, to the nowadays complex detectors such as the LHC.

In the development of newer particles detector, one can distinguish two big categories: the solid state detectors et the gaseous detectors. The former encompass detectors such as Cherenkov and scintillator counters while the later make use of gases as detection medium. The gaseous detectors have also greatly evolved during the past century from the Geiger-Muller tube to the spark or Pestov chambers, which can cope with the increasing detection rate of particles accelerator. The Parallel Plate Avalanche Chamber is a similar gaseous detector but operates in avalanche mode, where the detected signal is produced by a controlled multiplication of electrons in the gas. The aforementioned detectors were operated in spark mode, where the detection is made through a spark discharge in the gas. The avalanche mode allows even greater detection rates at the expense of signal amplitude.

In early 80s a new gaseous detector design began to emerge: the Resistive Plate Chambers. This detector has the particularity to operates in spark or avalanche mode depending on its design. Operated in avalanche mode, they present an impressing detection rates at the expense of very small electric signals, requiring dedicated amplification circuitries. Nowadays the Resistive Plate Chambers are widely used in numerous experiments worldwide, because of their interesting performances and relatively small price.

Despite their widespread usage, the Resistive Plate Chambers have not been extensively studied from a simulation and modelisation point of view. Simulation of a detector is an essential tool for its development and construction, as it allows to test a design and predict the performances one may get.

In this work we focused on the description of the physics phenomenons occuring during an electronic avalanche inside a Resistive Plate Chambers operated in avalanche mode, in order to properly modelise and simulate them. We review a detailed model of the ionisation process, which is the fundamental event in any gaseous particle detector, alongside the Riegler-Lippmann-Veenhof model for the electronic avalanche. A `C++` simulation has been produced in the context of this work and some results are presented.

Keywords: Resistive Plate Chambers, RPC, simulation, modelisation, ionisation

Résumé

Le siècle dernier a vu le développement de la physique des particules, avec la fondation du célèbre modèle Standard de la physique des particules. Plus spécifiquement, durant les 70 dernières années de nombreuses particules ont été détecté et étudié. Parallèlement à ces découvertes, les moyens experimentaux et les détecteurs ont grandement évolué. de la simple chambre à bulles de l'expérience Gargamel, qui a posé la première brique expérimentale du modèle standard, aux détecteurs complexes d'aujourd'hui tel que le LHC.

Durant le développement de nouveaux détecteurs, nous pouvons distinguer deux grandes catégories: les détecteurs dits *Solid State* et les détecteurs gazeux. La première englobe les détecteurs tels que les Cherenkov ou les scintilateurs tandis que les derniers utilisent un gaz comme moyen de détection. Les détecteurs gazeux ont aussi grandement évolué durant le siècle dernier, des tubes Geiger-Muller au chambres à étincelles ou Pestov, qui peuvent faire face aux taux de détections toujours grandissant des accélérateurs de particules. The Parallel Plate Avalanche Chamber est un détecteur gazeux similaire mais fonctionne en mode avalanche, où les signaux électriques sont produits par une multiplication contrôlée des électrons dans le gaz. Les autres détecteurs sus-mentionnées fonctionnent eux en mode étincelle, où le signal détectée est produit par une décharge électrique dans le gaz. Le mode avalanche permets un taux de détection encore supérieur mais au prix de signaux électriques beaucoup plus faibles.

Au début des années 80 un nouveau type de détecteur gazeux commence à se développer, les Resistive Plate Chambers. Ce détecteur présente la particularité de pouvoir fonctionner en mode étincelle ou avalanche, selon le design. Utilisé en mode avalanche, ils présentent un taux de détection particulièrement intéressant au prix de signaux électriques faibles, nécessitant un circuit d'amplification dédié. De nos jours les Resistive Plate Chambers sont très largement utilisés dans de nombreuses expériences de physique des particules, notamment pour leurs performances intéressantes et leur prix contenu.

Malgré leur usage répandu, les Resistive Plate Chambers n'ont pas été beaucoup étudié d'un point de vue modélisation et simulation. La simulation d'un détecteur est un outil essentiel pour leur développement et leur fabrication, permettant de tester un design et calculer les performances que l'on est en droit d'attendre.

Dans les travaux présentés dans ce document nous nous sommes intéressés à la description des différents phénomènes physiques se produisant durant une avalanche électronique au sein d'un Resistive Plate Chambers fonctionnant en mode avalanche, dans le but de les modéliser et simuler. Nous décrivons un modèle détaillé pour le processus d'ionisation, qui est l'évènement fondamental pour tout détecteur gazeux. Nous décrivons aussi un modèle mis au point par Riegler-Lippmann-Veenhof pour le développement d'avalanche electronique. Une simulation `C++` a été produite dans le contexte de cette étude et quelques résultats sont présentés.

Mots-clés: Resistive Plate Chambers, RPC, simulation, modélisation, ionisation

Contents

Chapter 1

Introduction

The history of modern particle physics is highly marked by the evolution of the means and techniques to produce, accelerate and detect particles. More specifically, the past 50 years have witnessed a tremendous experimental work which culminates with the Higgs boson discovery [27, 1] after that numerous experiments have, step-by-step, contributed to the validation of the Standard Model of particle physics in the fields of the electroweak interaction on one hand, and strong interaction on the other hand.

In this chapter we will talk and detail some experiments and discoveries in both fields alongside the experimental techniques development that goes with them.

1.1 Experimental discoveries and tests of the electroweak theory of the Standard Model

The first important step in this uninterrupted quest since then was, without doubt, the discovery of neutral currents at CERN, in 1973 with the Gargamelle experiment [43], at a time when the first foundations of electroweak interaction of the Standard Model were laid (Glashow, Salam and Weinberg in 1967/68). One of the most widespread detection technique used then was the bubble chamber placed in a magnetic field which allowed to acquire, with a high granularity, the interactions of particles with target nucleus held in the chamber. The figure 1.1 shows the experimental setup of the Gargamelle experiment at CERN. Figure 1.2 exhibits the first track photography of a neutral current interaction in the Gargamelle bubble chamber.

At that time the production and acceleration of protons through big synchrotron, such as the Proton Synchrotron (PS) at CERN (see figure 1.3), were perfectly mastered and used to produce lines of neutrinos and anti-neutrinos which allowed this fundamental discovery. The discovery of neutral currents lead to the experimental demonstration that the Fermi model for the neutrino interaction was insufficient.

At the same epoch the most used gaseous detector in particle physics was certainly the spark chamber. This particular detector is perfectly suited to the use of read-out electronics instead of the old technique of photography on film, just like the streamer chamber or even the flash chamber (though of different kind). The idea behind this detector was to provide a lighter alternative than bubble chambers for the tracking of charged particles. The spark chamber technique, doubtless the most used at that time because of its ease of construction, was also associated to a fundamental discovery; this time in the field of particle flavours. A spark chamber is basically, in its most basic form, a stack of conducting plates with a ionising gas in-between. When a charged particle goes through, it ionises the gas between the plates. Ordinary the ionisation would remain invisible, but if a high enough voltage is applied between adjacent pair of plates, the liberated electrons

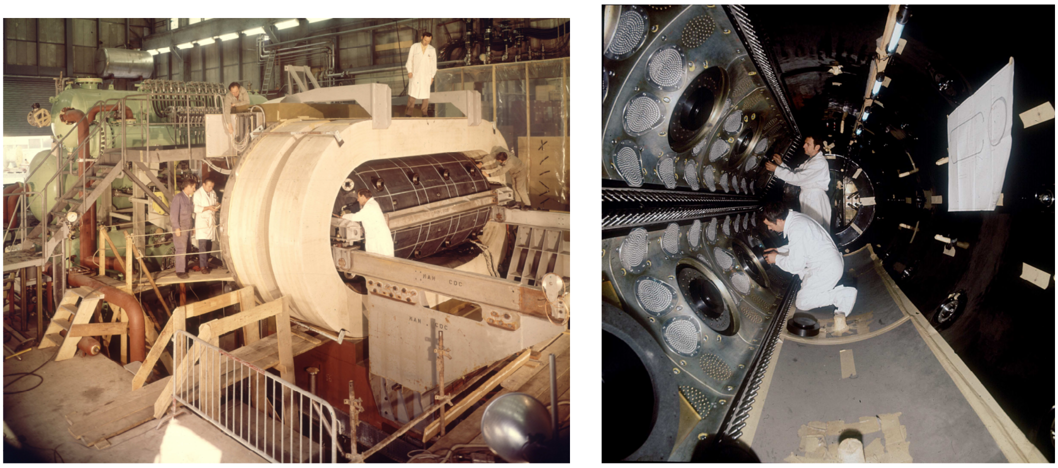

(a) The bubble chamber inside the magnetic coils. **(b)** Interior view of the bubble chamber.

Figure 1.1: The Gargamelle bubble chamber at CERN.

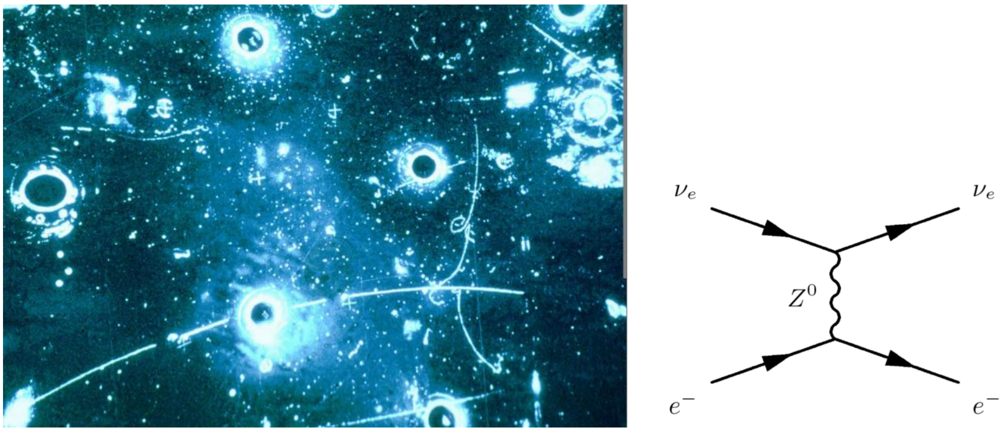

(a) Track photography in the Gargamelle chamber of a neutral current. An anti-neutrino enters from the top and knocks on an electron. **(b)** Feynman diagram of neutral neutrino-electron scattering.

Figure 1.2: The first weak neutral-current interaction observation in the Gargamelle bubble chamber.

multiplies in an exponential way and form a conductive channel between the plates thus provoking a spark discharge. Figure 1.4 exhibits schematically the operation of a spark chamber and the development of a spark. The SLAC/LBL experiment with the collision ring e^+e^- SPEAR used an internal tracker made of several cylindrical spark chambers inside a magnetic field used to bend the particle produced in the final state. They observed a sudden variation in the total hadronic cross-section above an energy of 3 GeV in the centre of mass [12]. In the same time, another experimental team at BNL (Berkeley National Laboratory) observed a very narrow resonance for the disintegration in pair $\mu^+\mu^-$ at a mass of 3.1 GeV/c^2 [11]. This discovery of the charmed quark was fundamental as it proved experimentally the existence of the second family of fermions that is formed by the charmed and strange quarks. At a theoretical point of view, this discovery validated the GIM (Glashow-Illiopoulous-Maiani) mechanism which solved the problem of the suppression of flavour changing neutral current, with a second complete family of quarks. Some

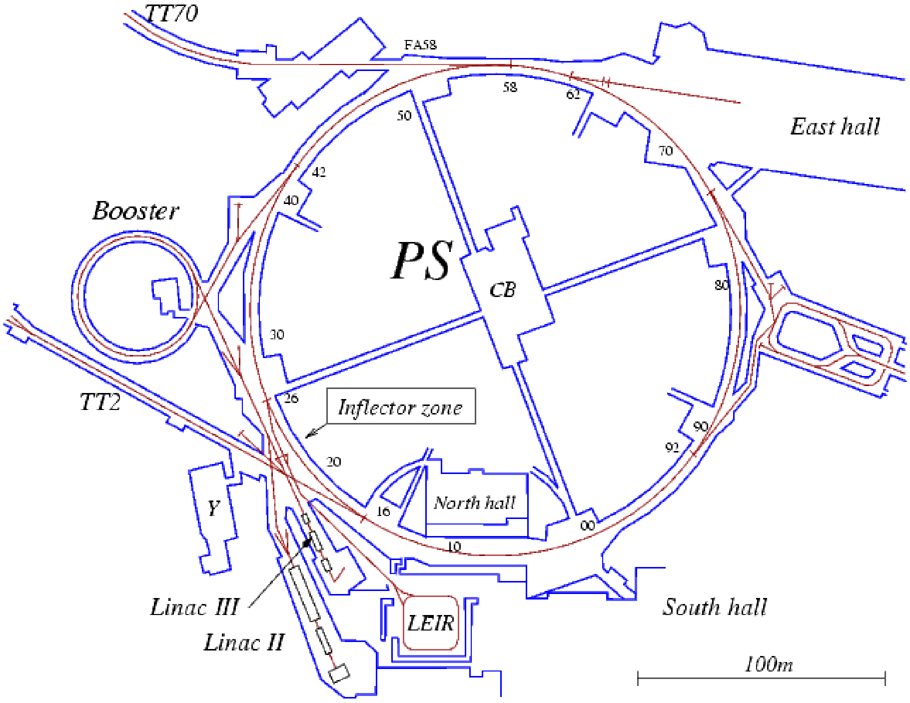

Figure 1.3: The Proton Synchrotron (PS) at CERN.

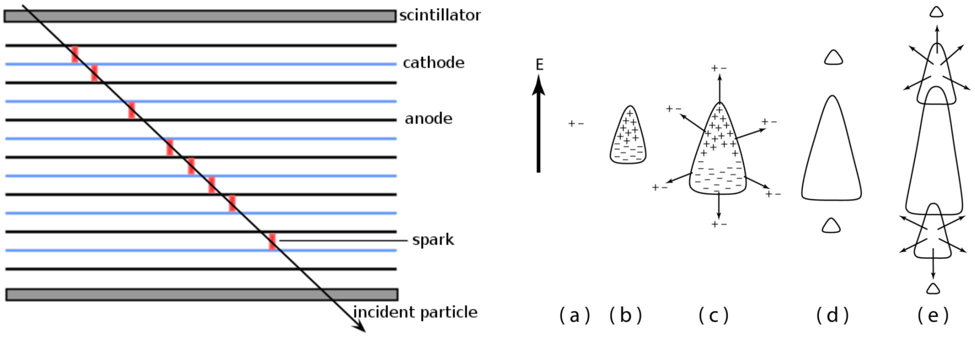

(a) **(b)** (From [30])

Figure 1.4: Working description of a spark chamber. (a) schematic view of a spark chamber, scintillators are used to trigger the high tension when a charged particle is detected. (b) Streamer formation process. (a) the particle has liberated an electron-ion pair; (b) The electrons multiplies during an avalanche; (c) emission of photons that produce new electron-ion pair through photo-ionisation; (d) secondary avalanches appear; (e) the avalanches merge together and further develop into a conductive channel

time later, in 1975, was observed the first sign of a third lepton family at the SPEAR collision ring with the observation of pair $e\mu$ resulting from the disintegration of τ lepton, whose properties was extensively studied as a test of the Standard Model.

The development of e^+e^- collision ring of increasing energy and luminosity has made older techniques of detection obsolete, like the bubble chamber which was capable to detect only some particles per second and whose analyse was done by hand on photographic films. With the development of fast electronics and the emergence of computer data analysis, coupled to the increasing need for detector of various geometries (plane or cylindrical for the most part) and of bigger size in order to instrument collisions vertex or spectrometer on beam target experiences, new detection techniques began to appear as spark chambers could not cope the increasing interaction rate.

The Multiwire Proportionnal Chambers (MWPC) invented in 1968 [26] allowed many laboratories, even the modestly small ones, to build extremely efficient equipments that have then been used on new e^+e^- colliding rings in the 70s (SPEAR, PEP at SLAC and DORIS, PETRA at DESY notably, but also DCI at Orsay and ADONE at Frascati) and on beam experiments, notably at CERN with its new synchrotron SPS but also BNL and Fermilab. A MWPC is basically a collection of thin and conductive anode wires, parallel and equally spaced, between two cathode plates as depicted schematically on figure 1.5a. A negative potential is applied to the cathode plates, with the anode wire being grounded, thus an electric field appears in the chamber following the equipotential lines shown on figure 1.5b. When charges are liberated after the ionisation of a charged particle, they will first drift along the equipotential lines until they reach the high field region, in the vicinity of the wire, where they develop into an avalanche and multiply (due to the $1/r$ field, r being the wire radius).

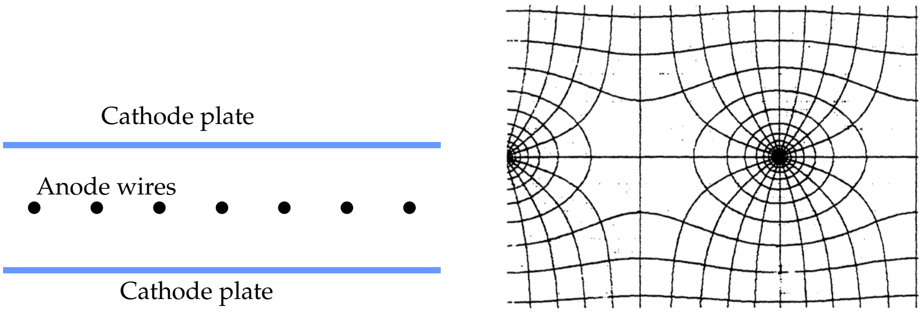

(a) Schematic view of a MWPC

(b) Electric equipotential lines around an anode wire. (From [94])

Figure 1.5: Multi Wire Proportional Chamber.

Based on the same principles than the MWPC, new detectors have been developed: the Drift Chamber and the Time Projection Chamber (TPC). The Drift Chamber (see figure 1.6a) is basically a MWPC but with more distant anode wires, and cathode wires placed in-between. A cathode and anode wire form together a drift cell. The cathodes

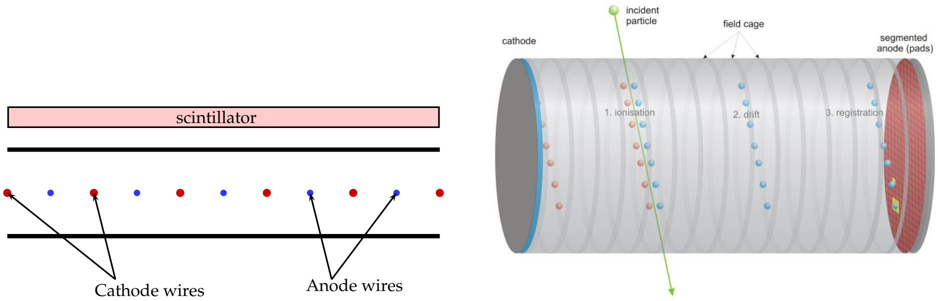

(a)

(b)

Figure 1.6: Drift Chamber and Time Projection Chamber

are positioned in such a way to produce a constant electric field between wires, and a constant drift velocity so that one may calculate the drift distance (using the timing provided by scintillators). The Time Projection Chamber (see figure 1.6b) is made of a central cathode that divides a volume into two identical halves. Field cages are used to maintain a constant electric field and anode end-caps enclose the volume. The anodes are usually made of detection pads in order to resolve the radial coordinates, the z-coordinate is inferred from the drift time.

After the discovery of the J/Ψ particle, and so of the charmed quark, the observation in 1977 of the quark b, forming the Y resonance in the E288 experiment at Fermilab [45], opens the hypothesis of the existence of a third quark family (penchant of the third leptons family discovered by the observation of the τ lepton). At that time, most detectors took use of the properties of the wire chambers.

Older detection techniques, such as the flash chambers [31] developed during the 1950s alongside the streamer and spark chambers, were continued to be used in specific instruments which do not need high acquisition rate. This was the case for several tracking experiments at the beginning of the 90s; like, for example, of the Frejus experiment which aimed to measure the proton time of life.

At the end of the 70s, several tasks needed to be done in order to validate the electroweak standard model: the validation of the number of families, the explicit observation of the Z and W bosons and, in fine, of the Higgs boson. The invention of the stochastic cooling of particle beams allowed the construction of the S$p\bar{p}$S at CERN and the observation of the W and Z bosons in 1983, which were out of reach of e^+e^- collider rings. Gaseous chambers based on the concept of Charpak et al. were extensively used in the UA1 and UA2 detectors of the S$p\bar{p}$S. For instance UA1 was equipped of 6 layers of drift chambers for the internal tracking, and also of drift chambers for the muons detectors.

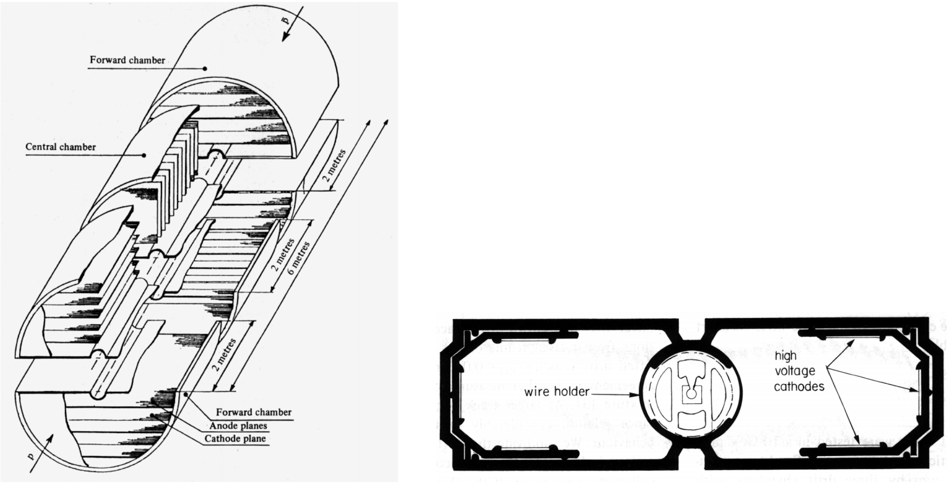

(a) Central tracker **(b)** Muon drift chamber cell

Figure 1.7: UA1 detector. (From [10])

It was with the operation of the LEP in 1989 to further experimentally validate the hypothesis of the three leptons families. The four experiments (ALEPH, DELPHI, OPAL, L3) were composed of gaseous detectors as internal trackers, either for the particle impulsion measurement (often with the use of TPC) or for the fine tracking close to the beam for the reconstruction of interaction and disintegration vertex (of beauty and charmed particle principally). The Higgs boson stayed out of reach but the LEP experiments undertook a thorough test of the Standard Model. Given the importance of the detection of beauty particles for these tests a new generation of detector were developed and used, the silicon trackers, which offered much better spatial resolution than gaseous detectors.

The quark top was discovered at Fermilab [5, 2], and thus completing the quark families. From then, physicists had to wait the operation of the LHC in order to reach the energy needed to finish the validation the Standard Model. The Resistive Plate Chambers began to appear quasi-systematically on big detectors as trigger chamber because of their high reactivity. They exhibit time resolutions such that they can be considered for Time-Of-Flight particle identification.

1.2 Emergence of the Quantum Chromodynamics as a theory of the strong interaction

In the treatment of the strong interaction, a perturbative approach to the Field Theory could not be considered; unlike the weak and electromagnetic interactions whose intensity allowed it. Although a perturbative approach to the Field Theory is excluded, some models have been elaborated anyway. For example the Nambu-Jona-Lasinio model where the pion played the role of force carrier, as a Goldstone boson, acquiring its mass through chiral symmetry breakdown.

The quark model, constituents of hadrons, was developed by Gell-Mann and Zweig but was perceived with suspicious because, despite experimental efforts, no particle with an electric charge of a fraction of the electron's has been observed. Yet, from the end of the 1960s, the deep inelastic scattering of electrons on protons has shown, on the SLAC's linear accelerator, that electrons behave like they were scattered on punctual target that are of much smaller dimension than the nucleus and free inside it: this was named the asymptotic freedom. The electromagnetic form factors satisfied the Callan-Gross relation, pointing to the fact that the sources of diffusion inside the nucleus was half-spin nature. Those were called partons, before the validation and acceptance of the quark model.

The Ω^- and Δ^{++} baryons are made of three quarks s and three quarks u respectively, and thus could not exist in their spin state (because of the Pauli exclusion principle) without the addition of a new quantum number that is carried by the quarks, which was later named "colour". This led to the development of Quantum Chromodynamics. It was demonstrated in 1970 that we may elaborate quark dynamics with the addition of colour vector bosons, gluons, that also possessed the asymptotic freedom property. However, in 1974, it was noticed that the disintegration width of the recently discovered J/Ψ was very small for a hadron. This was something perfectly explainable through the theory of coloured quarks but not directly understood at that time. Indeed, the coupling of the pair $c\bar{c}$ to lighter quarks is done through three gluons, as depicted on figure 1.8. Given this coupling intensity, typically given by α_S^3, the strong disintegration is not so much superior of the electromagnetic one defined by α. But at the time, the old OZI rule was invoked in order to explain this small disintegration width. This empirical rule dictates that the decay modes by strong interaction whose final states do not contain the initial quarks are heavily suppressed. This rule is perfectly explained by the Quantum Chromodynamics. In some way the discovery of J/Ψ, in addition to be the revealer of the charm, perfectly illustrates the colour mechanisms of the Quantum Chromodynamics.

It was with what followed this discovery that we had the clear proofs of the Quantum Chromodynamics, in particular on e^+e^- colliders PEP and PETRA. Figure 1.9 shows the TASSO detector installed at PETRA which played a part in the study of the Quantum Chromodynamics. The TASSO experiment was the first to observe three-jets events resulting from the fragmentation of quarks but also the radiation of gluons. This allowed to prove the existence of the gluons with spin 1.

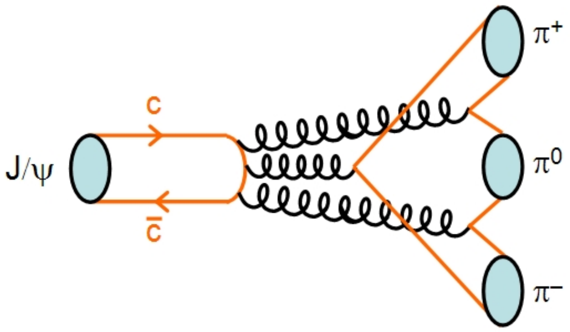

Figure 1.8: J/Ψ disintegration with three gluons.

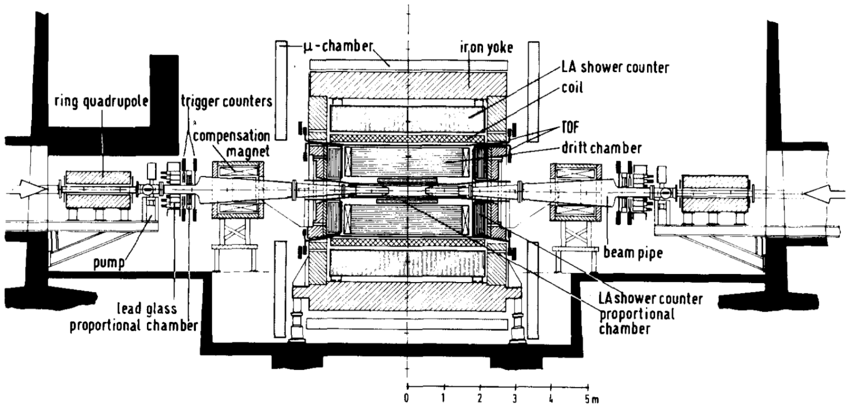

Figure 1.9: The TASSO detector, at PETRA. (From [53])

The performance of e^+e^- colliders allowed to validate the basis of the Quantum Chromodynamics without ambiguity, at least in the regime of the asymptotic freedom and quarks and gluons fragmentation. The heavy ions experiment were awaited to study the confinement/deconfinement phase transition of quarks and gluons, at RHIC (BNL) and SPS (CERN) in particular. Today this transition is extensively studied at LHC with the dedicated ALICE detector, but also with CMS, ATLAS and soon LHCb detectors.

1.3 Development of gaseous detector

In the last chapter we detailed the advancement of modern particle physics; the big discoveries were permitted by progress in the particle detection. Many detectors of different kind were investigated in the past, but we can distinguish two big families

1. the solid state detectors,
2. the gaseous detectors.

The solid state family encompass detectors such as Cherenkov and scintillator counters. The use of a gaseous medium as detection volume allows to take advantage of the high mobility of electrons, in order to eventually detect single electron (with an adapted amplification circuitry).

Maybe one the oldest gaseous detector is the basic ionisation chamber. A free-air ionisation chamber, which use the atmosphere as detection volume, was built in 1937 by

Herb Parker at th Swedish Hospital in Seattle to measure the exposure rate in an x-ray beam. Nowadays free-air ionisation chamber are mainly used in domestic smoke detector, they detect the subtle changes in ionic flow due to the passage of smoke. Since then, gaseous detector were actively studied and developed to be used in particle experiments, as we described in the previous chapter.

At first the detection technique were based on the reconstruction of emulsion tracks produced by a charged particle in a bubble or cloud chamber from photographic film. The development of amplification circuitry has permit to evolve to detection and acquisition system based on electric signal, which was first used on spark and streamer chambers. The wire based detectors, such as the Geiger-Muller tube that appeared at the end of the 1920s, even though easy and cheap to produce, could not cope with the time resolution of solid state detectors. This is because of the $1/r$ field that limits the amplification volume to the vicinity of the wire, and all electron needs to drift to this region before any amplification and signal induction may occur, as it is shown on figure 1.10.

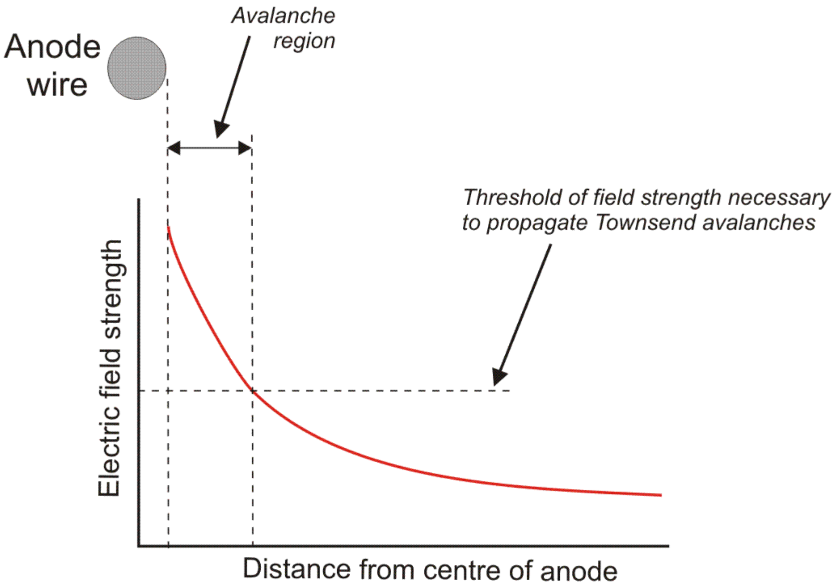

Figure 1.10: Electric field generated by a conducting wire.

The spark counter overcome this time resolution limitation by using parallel plates with a strong and uniform field in between produced by the application of a strong voltage on the electrodes, introduced by Keuffel in 1948 [59]. The operation principle is shown on figure 1.4. The passage of a charged particle ionises the gas freeing electrons, which immediately triggers a Townsend avalanche due to the high and uniform electric field. This avalanche grows until a streamer appears, due to photons contributing to the avalanche growth, and create a conducting channel between the electrodes. The electrodes are discharged through the stream producing a spark. The spark counter offered a time resolution of around 1 ns, far better that any Geiger-Muller tube used at that time (around 100 ns). However they are limited to an area of a few cm^2, because otherwise the discharge spark would carry enough energy to deteriorate the electrode plates. Furthermore the rate detection capability is limited by a dead time due to the recharge of the electrodes.

In the early 1970s was developed the Pestov chamber [86]. It is based on the same design as the spark counter but with the conductive anode replaced by a high resistivity glass, as depicted by figure 1.11. The high resistivity glass keeps contained the spark discharge around the avalanche and the drop on the high tension is only local, thus the

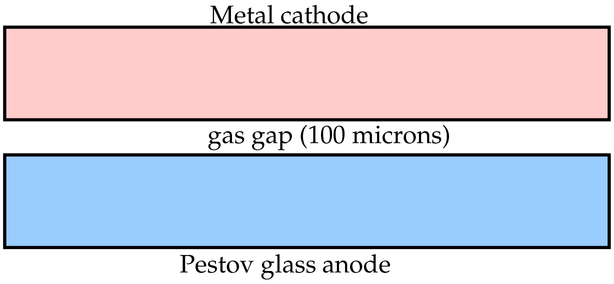

Figure 1.11: Basic layout of a Pestov spark chamber.

rest of the volume remains sensible to the passage of charged particle. However it limits the charge produced by a spark discharge and, coupled to a small gap of around 100 µm, needs a very high tension typically about $500\,\mathrm{kV\,cm^{-1}}$. Moreover the gas needs to be over-pressurised to 12 bar, ensuring a sufficient primary ionisation density to account for good detection efficiency.

Whereas the spark and pestov chamber were operated in streamer mode, the Parallel Plate Avalanche Chamber (PPAC) [25] are used in avalanche mode: the apparition of streamer and spark discharges are unwanted and suppressed. It consist in the same basic layout, where two planar electrodes encompass a gas gap ranging from 0.5 to 2 mm. It yields a very good rate capability of several $\mathrm{MHz/cm^2}$ and a time resolution of some hundreds of picoseconds. However it outputs very small signals, of $\sim 100\,\mathrm{fC}$ typically, and the amplification circuitry has to be designed accordingly to account for the weak signal/noise ratio.

1.4 Description and simulation of Resistive Plate Chambers

The Resistive Plate Chamber (RPC) were introduced in 1981 [92]. It is similar to a spark chamber or a PPAC, consisting in two parallel electrode plates which, however, are made of a high resistivity (Bakelite or glass typically). A high tension is applied between the plates. In the same manner than the Pestov counter, the high resistivity contains the drop of the electric field locally in the zone of ionisation and leave the rest of the volume sensible to the passage of other charge particles. The figure 1.12 is a sketch of the first RPC prototype.

When a charged particle goes through the gas gap of a RPC, it will ionises the molecules and create electron-ion pairs. The liberated electrons will drift towards the anode under the influence of the electric field and gain energy while doing so. Once the electron has more energy than the ionisation potential of the gas molecules, it has a high probability to create new electron-ions pair that will also drift and provoke further ionisation. Then the number of electrons augments in an exponential way and a Townsend avalanche develops. The principle is depicted on figure 1.13b. As the electrodes are made of a resistive material the read-out signal is not made of the avalanche electrons, but it is induced by the movement of the charges in the gas gap on detection strips or pads.

Depending on the detector characteristics and parameters, such as the applied electric field, the gas gap width or the gaseous mixture, a RPC can be operated on streamer or avalanche mode.

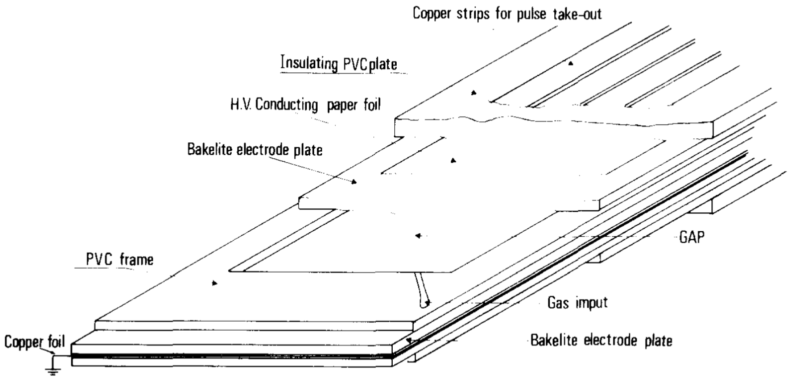

Figure 1.12: Sketch a the first RPC prototype. (From [92])

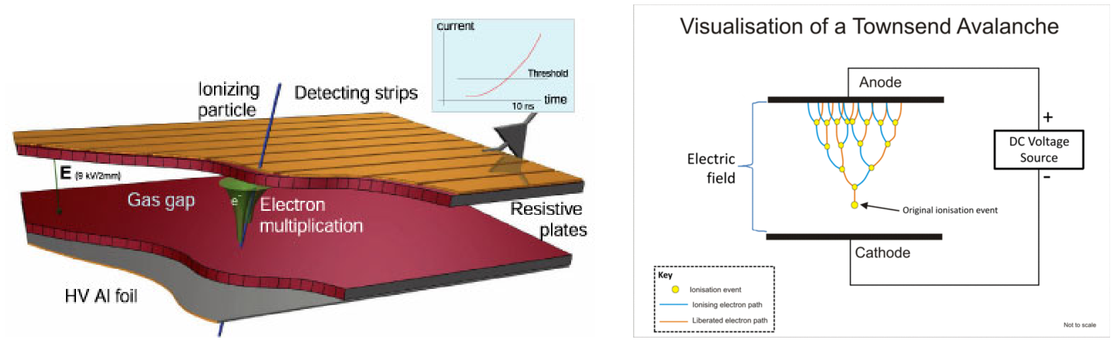

(a)

(b)

Figure 1.13: (a)Principle of operation of RPC. (b) Schematic development of a Townsend avalanche.

Streamer mode

A operation of a RPC in streamer is similar to a spark chamber

1. the ionisation of a particle create electron-ion pairs
2. the electrons drift and multiply into a Townsend avalanche
3. at some point, if the gas multiplication gain is high enough, new avalanches are started from electron-ion pair created by photons through photo-ionisation and contribute to the total avalanche formation.
4. a conductive channel may form between the two electrodes, through which they are locally discharged.

In streamer mode the output signals are quite large (from 0.1 to 1 nC) and thus simple or even none amplification circuitry is needed. But, as in spark and Pestov chambers, the detection rate capability is lowered to $\sim 200\,\mathrm{Hz/cm^2}$.

Avalanche mode

In avalanche mode the transition to streamer is unwanted. The contribution of photons to the avalanche, that triggers the transition, can be suppressed by adding small amount of an UV quencher gas and traces of an electronegative gas [21]. They absorb the created photons in the avalanche and prevent the latter to multiply and develop too much.

Doing so allow the detectors to reach rate capabilities of several kHz/cm^2. However the output signals are drastically lowered, from 0.1 to 5 pC typically. Thus the need for good amplification electronics with low noise.

Because of their good rate capability, RPC in avalanche mode are used at LHC on the ATLAS and CMS detectors. A continuation of this design, the multigap RPC, is also used on the ALICE detector [24].

RPCs in avalanche mode are made of gas gap ranging from 0.1 to several millimeters, with an operating voltage typically from 40 to 70 kV cm^{-1}. The resistive electrodes are typically in the order of some millimeters in width with a volume resistivity from 10^{10} to 10^{12} Ω cm depending on the material.

1.5 Simulation and modelisation of RPC

The RPCs are now widely used on numerous High Energy Physics experiments, as tracking and timing detectors. As of today, numerous simulations for RPCs are described in the literature. Those models rely on mathematical distributions (such as the Polya distribution, described later in this document in chapter3) that fit nicely several macroscopic values, such as the output electric signals or charge spectra. However some of these models' parameters lack physical interpretation and thus need ad-hoc parametrisation. So in the hope to simulate a detector, one needs experimental data in order to fine-tune the model.

Using this approach, one may extrapolate the working behavior of an already-built detector based on its actual experimental data. However one could not simulate a specific detector design and its performances without building it.

In this work, we have studied the modelisation and the simulation of Resistive Plate Chambers operated in avalanche mode, on a macroscopic and microscopic scale, in the goal to develop a full, fast and multi-thread `C++` simulation code.

We will first detail the physics behind the ionisation of a gaseous mixture by the passage of a charged particle. Then we will talk about a model for avalanche development and propagation in gases. We will also detail the basic working operation of Pseudo Random Number Generators which are the very heart of any Monte-Carlo simulations, although too often overlooked. Finally we'll describe the implementation of the model in a simulation program and results, but also limitations, that it yields.

The produced simulation source code is publicly available and hosted on `Github` [36]: `https://github.com/vincentFrancais/RPCSim`

Chapter 2

Primary ionisation in gas

In this section we will discuss about the theories and models for the primary ionisation in a medium, with a focus on gases. We do not go into details for the theories and the derivation of the equation as it is not the purpose of this work.

2.1 Introduction

When a charged particle goes trough a gas, it undergoes a series of stochastic interactions with atoms and molecules, transferring a part of its energy. In this context we are mostly interested by the inelastic diffusion, and most specifically ionisation. This exchanged energy is then dissipated by the creation of an ion-electron pair and the emission of photons; those photons and electrons can then ionise other atoms and so on. The multiplication of ion-electron pairs stops when the energy of the emitted particles becomes smaller than the ionisation potential of the considered atom. This *initial ionisation*, induced by the passage of a charged particle, is of crucial importance for the study of RPC detectors as it determines many characteristics of the avalanche and signals.

The Bethe formula for the mean energy loss by excitation and ionisation

The energy lost by a charged particle traversing a medium has been investigated by Bethe in the 1930s [15]. For a heavy particle of mass $M \gg m_e$, the Bethe formula gives the mean integrated energy loss by the particle through excitation and ionisation processes [85]

$$\left\langle -\frac{\mathrm{d}E}{\mathrm{d}x} \right\rangle = Kz^2 \frac{Z}{A}\frac{1}{\beta^2}\left(\frac{1}{2}\ln\frac{2m_ec^2\beta^2\gamma^2T_{max}}{I^2} - \beta^2 - \delta(\beta\gamma)\right) \tag{2.1}$$

where

K - a constant defined by $K = 4\pi N_A r_e^2 m_e c^2$,
r_e - the classical electron radius $r_e = \frac{1}{4\pi\varepsilon_0}\cdot\frac{e^2}{m_ec^2}$,
e - the electron elementary charge,
m_e - the electron mass,
N_A - the Avogadro's number,
z - the charge of the incident particle,
Z,A - the atomic number and atomic mass of the absorbing medium,
ε_0 - the dielectric constant in vacuum,
β - the velocity of the particle $\beta = v/c$,
c - the speed of light,

γ - the Lorentz factor $\gamma = \left(1-\beta^2\right)^{-1/2}$,
T_{max} - the maximum energy transfer in a single collision,
I - the mean excitation energy of the absorbing medium,
δ - the density effect correction.

One can notice, as intuitively expected, that eq. 2.1 is directly proportional to the density of electrons in the medium, through the factor $N_A \times Z/A$.

In the non-relativistic case, the main dependence in the charged particle speed is in the factor $1/\beta^2$. So in this case the mean energy loss strongly increases as shown in figure 2.2. As a naive interpretation of this effect, we can interpret that electric field of the particle stay for a longer period in the near vicinity of an atom and thus increasing the probability electromagnetic interactions.

The maximum energy transfer in a single collision is defined by [85]

$$T_{max} = \frac{2\, m_e\, p^2}{M^2 + 2\gamma\, m_e\, M + m_e^2}, \tag{2.2}$$

with p the momentum of the particle.

The mean excitation energy I is characteristic of the absorbing medium. Its knowledge is the main non-trivial input of the Bethe formula. It was, in particularly, investigated by Bloch in the year 1933

$$I = (10\,\text{eV}) \times Z. \tag{2.3}$$

That's why eq. 2.1 is often referred as Bethe-Bloch. Others phenomenological formulations for the mean excitation energy I has been proposed in the past. For instance, it can be approximated by the following equation [41]

$$I = 19.2\,\text{eV for } Z = 1, \quad I \sim 16 Z^{0.9}\ \text{eV} \ \text{ for } Z > 1. \tag{2.4}$$

In practice, those values are now obtained from experimental measurements and are referenced in publicly available tables [84]. Figure 2.1 shows the experimental mean excitation energy I as a function of Z, along with the parametrisation of eqs. 2.3 and 2.4. The Bloch approximation may only be considered for large Z but still doesn't account for the large fluctuations of I. The Shwartz expression parametrises the general shape of I/Z but also deviates quite sensibly from experimental values because of fluctuations.

Eq. 2.1 is only valid for heavy particle. For electron colliding with atomic electrons the equation has to be modified. The main reason is the incident and target particles are of equal mass, therefore one can no longer distinguish between the primary and secondary electron after the collision (see [85, 41]). Also the small mass of electrons induce important loss through radiative processes instead which dominate completely the ionisation processes. Figure 2.2 shows the mean energy loss for different incident particles and numerous mediums.

Relativistic rise and density effect

For relativistic particles ($\beta\gamma \gtrsim 4$), the transverse electric field associated to the moving charged particle increases due to the Lorentz factor $E_T \to \gamma E_T$. Thus the interaction cross-section extends as well and the distant collisions contribution to the energy loss (eq. 2.1) increases as $\ln \beta\gamma$ [85].

Because of the higher electric field the absorbing medium becomes polarized, shielding the electric field far from particle path thus cutting off the long range interactions. This is the so called *density effect* which, as the name suggest, is greater for dense absorber mediums as the density of atomic electrons is higher. This effect is taken into account in eq. 2.1 by the density correction term $\delta(\beta\gamma)$.

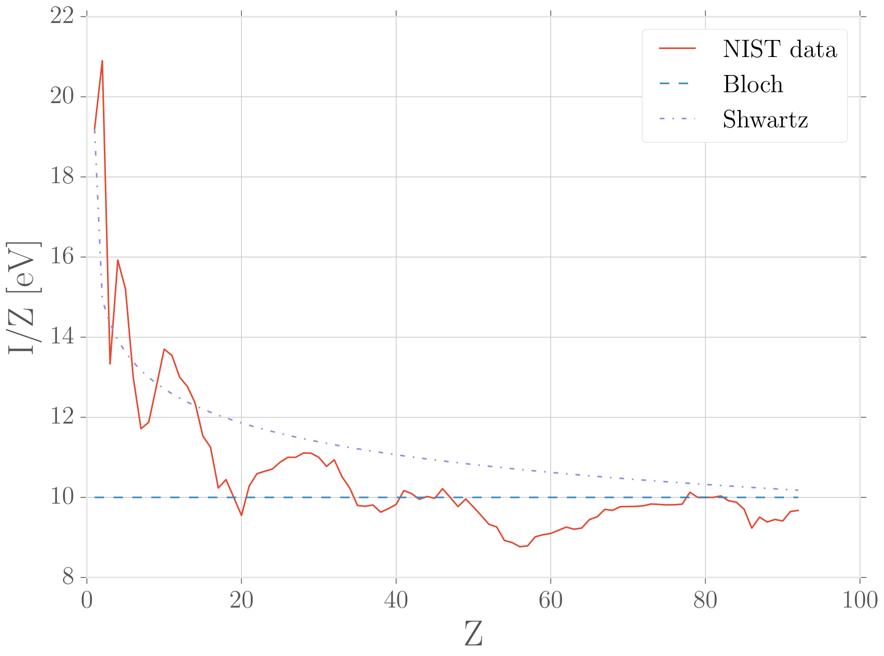

Figure 2.1: Mean excitation energy I for elements referred by their atomic number Z. The curve labeled NIST data are experimental values from [84], the curves labeled as Bloch and Shwartz are for eqs. 2.3 and 2.4 respectively.

At high energy, which is our usual study case in this work, this correction term tends to the well know formula

$$\delta(\beta\gamma) \to \ln(\hbar\omega_p/I) + \ln(\beta\gamma) - 1/2, \quad \hbar\omega_p = \sqrt{\frac{ne^2}{m_e\varepsilon_0}}. \tag{2.5}$$

Where $\hbar\omega_p$ is the plasma energy of electron in the given medium, with n the electron density.

Stochastic fluctuations of energy loss

As stated before the Bethe formula describes the *mean* energy loss in a medium. In a detector, measurements are done via the total energy loss ΔE over a medium of thickness Δx with

$$\Delta E = \sum_{n=1}^{N} \delta E_n \tag{2.6}$$

with N the total number of collision and δE_n the energy loss at the n^{th} collision. Both the total number of collisions N and local energy loss are stochastic variables. The energy loss during a collision δE follows a Landau distribution [64], see figure 2.3. This Landau distribution exhibits that the most probable value is quite different than the mean value, mainly due to large fluctuations at high energy loss.

Total energy loss

Figure 2.4 shows the total energy loss for muon in copper absorber. The part of the plot labeled Bethe corresponds to the energy loss given by the Bethe formula eq. 2.1,

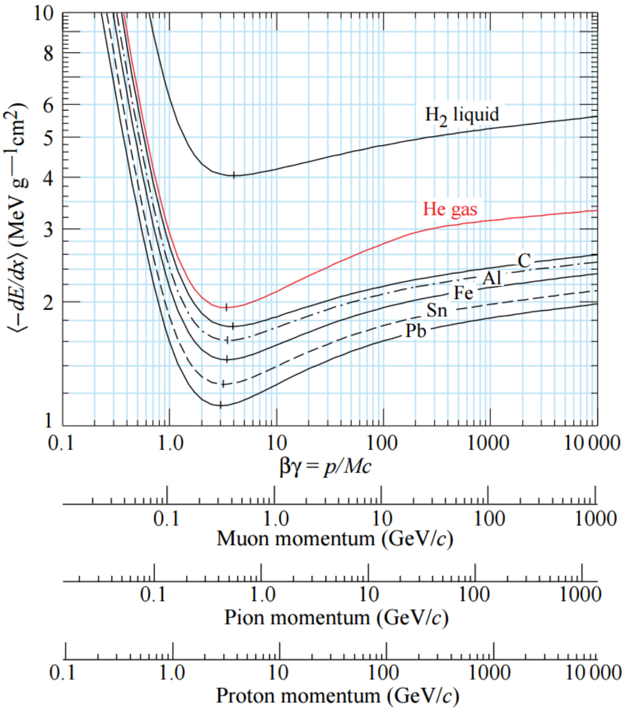

Figure 2.2: Mean energy loss for different incident particle and numerous mediums (from [85]).

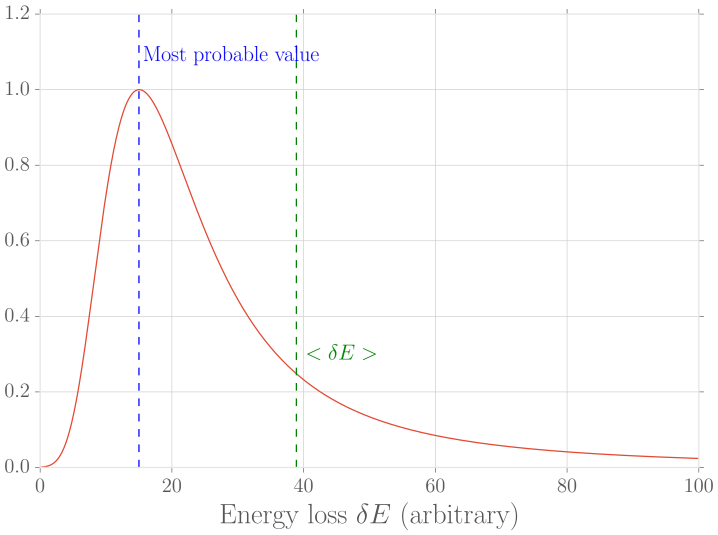

Figure 2.3: Arbitrary Landau distribution for energy loss. The most probable value and the mean value for energy loss are indicated.

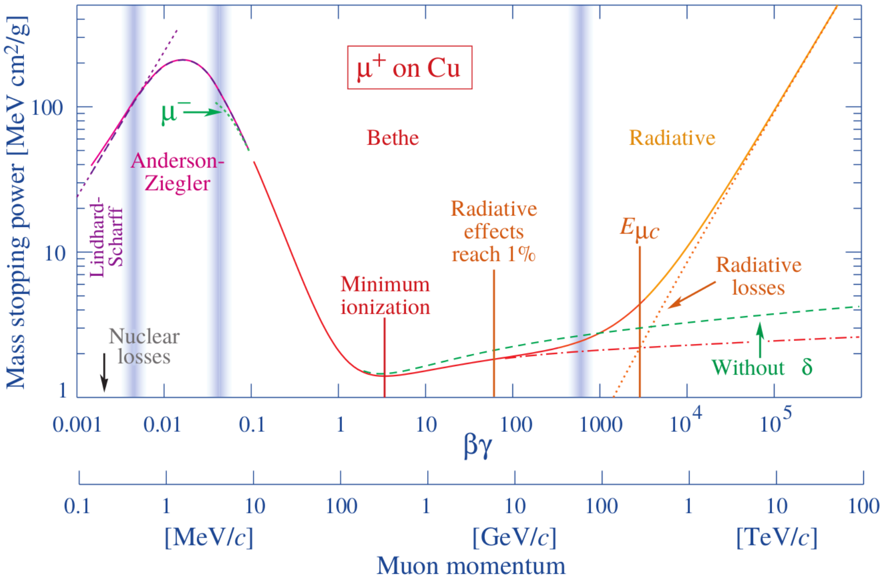

Figure 2.4: The total energy loss for muon traversing copper absorber (from [85]). The vertical bands delimit the different regime for the energy loss.

both curves shows the energy loss with and without the density correction term δ. The right hand part of the plot corresponds to the energy loss by radiative processes (mainly Bremsstrahlung). The critical energy E_c corresponds to the point where the ionisation and excitation loss is equal to the radiative loss

$$-\frac{\mathrm{d}E}{\mathrm{d}x}(E_c)\bigg|_{\text{ionisation}} = -\frac{\mathrm{d}E}{\mathrm{d}x}(E_c)\bigg|_{\text{radiative}} . \tag{2.7}$$

For electrons and positons, it can be approximated through this parametrisation [41]

$$\begin{aligned} E_c &= \frac{610\,\text{MeV}}{Z+1.24} \quad \text{for solids,} \\ E_c &= \frac{710\,\text{MeV}}{Z+0.92} \quad \text{for gases.} \end{aligned} \tag{2.8}$$

The left hand part of figure 2.4 corresponds to loss for low energy, where we have to consider that the atomic electrons are not stationary (shell corrections).

2.2 The Photo-Absorption Ionisation model (PAI)

In order to simulate the signal of a RPC we need precise knowledge of the initial ionisation. As the Bethe formula gives only the mean energy loss we need more precise models that gives the distribution of individual ionisations at a microscopic level along the track of the incident particle.

It is now commonly supposed that the rate of ionisation from a fast charged particle traversing a gas depends on two things [66, 40, 8, 97]:

- the cross-section of ionisation of the gas atoms by real photons. Indeed the interactions of the incident charged particle with the atoms is of electromagnetic nature and thus mediated by quasi-real photons.
- the dielectric constant, which describes the electromagnetic behaviour of the medium.

The model used in most simulation to compute the initial ionisation in a gas by a charged particle is called the Photo-Absorption Ionisation (PAI) model, first developed by Allison and Cobb [8] in 1980. It gives the cross-section of the energy transfers from the particle to the gas.

We can describe this model by a simplified approach with classical electrodynamics. We won't detail all the calculation steps nor the derivation of all the equations as it involves a lot of complex algebra not relevant here.

We consider a dielectric and non-magnetic medium with permittivity ε. When a charged particle goes through this medium with velocity $\vec{\beta}c$, it locally polarises the atoms and thus produces an electric field. This electric field $\vec{\mathbf{D}} = \varepsilon\vec{\mathcal{E}}$ with the associated charge density $\rho = e\delta(\vec{r} - \vec{\beta}ct)$ and current density $\vec{J} = \vec{\beta}c\rho$ describes electromagnetically the movement of the fast charged particle in the medium.

Working in SI units, the Maxwell's equations in this medium may be written as

$$\vec{\boldsymbol{\nabla}} \cdot \vec{\mathbf{H}} = 0 \qquad \vec{\boldsymbol{\nabla}} \times \vec{\mathbf{D}} = -\frac{\partial \vec{\mathbf{B}}}{\partial t} \tag{2.9a}$$

$$\vec{\boldsymbol{\nabla}} \times \vec{\mathbf{H}} = \vec{\mathbf{J}} + \frac{\partial \vec{\mathbf{D}}}{\partial t}, \qquad \vec{\boldsymbol{\nabla}} \cdot \vec{\mathbf{D}} = \rho. \tag{2.9b}$$

This electric field is associated to the charge density and current describing the passage of a charged particle

$$\rho = e\delta(\vec{r} - \vec{\beta}ct); \quad \vec{J} = \vec{\beta}c\rho. \tag{2.10}$$

In the Coulomb gauge the vector and scalar potentials are defined through

$$\vec{\mathcal{E}} = -\vec{\nabla}\phi - \frac{\partial \vec{A}}{\partial t}; \quad \vec{H} = \vec{\nabla} \times \vec{A}; \quad \vec{\nabla} \cdot \vec{A} = 0. \tag{2.11}$$

Using Fourier transforms, we now have an expression for the potentials and thus for the electric field [8]

$$\phi(\vec{k}, \omega) = \frac{1}{4\pi\varepsilon_0} \cdot \frac{2e}{\varepsilon k^2}\, \delta(\omega - \vec{k} \cdot \vec{\beta}c), \tag{2.12a}$$

$$\vec{A}(\vec{k}, \omega) = \frac{1}{4\pi\varepsilon_0} \cdot \frac{2e}{c^2} \frac{\omega\vec{k}/k^2 - \vec{\beta}c}{\varepsilon\omega^2/c^2 - k^2}\, \delta(\omega - \vec{k} \cdot \vec{\beta}c), \tag{2.12b}$$

$$\vec{\mathcal{E}}(\vec{r}, t) = \frac{1}{(2\pi)^2} \iint \left[i\omega\vec{A}(\vec{k}, \omega) - ik\phi(\vec{k}, \omega) \right] \exp\left\{ i\left(\vec{k} \cdot \vec{r} - \omega t \right) \right\} \mathrm{d}^3k\, \mathrm{d}\omega \tag{2.13}$$

The energy loss by the moving particle is the work done by the Lorentz force $\vec{F} = e\vec{\mathcal{E}}$ exerted on the particle itself (with $\vec{F}$ being in the opposite direction of the velocity $\vec{\beta}c$) [65]

$$\left\langle \frac{\mathrm{d}E}{\mathrm{d}x} \right\rangle = e\vec{\mathcal{E}}(\vec{\beta}ct, t) \cdot \frac{\vec{\beta}}{\left|\vec{\beta}\right|}. \tag{2.14}$$

Using the expression for the electric field eq. 2.13, we obtain

$$\left\langle \frac{\mathrm{d}E}{\mathrm{d}x} \right\rangle = \frac{1}{4\pi\varepsilon_0} \frac{e^2 i}{2\pi^2\beta} \iint \left[\frac{\omega}{c^2} \frac{\frac{\omega\vec{k}\cdot\vec{\beta}}{k^2} - \beta^2 c}{\frac{\varepsilon\omega^2}{c^2} - k^2} - \frac{\vec{k} \cdot \vec{\beta}}{k^2\varepsilon} \right] \delta(\omega - \vec{k} \cdot \vec{\beta}c) e^{i\left(\vec{k}\vec{\beta}c - \omega\right)}\, \mathrm{d}^3k\, \mathrm{d}\omega\,. \tag{2.15}$$

The complex dielectric constant is defined by $\varepsilon = \varepsilon_1 + i\varepsilon_2$ where ε_1 and ε_2 describe the polarisation and absorptive properties of the medium. Figure 2.5 shows the evolution of the real and imaginary part of ε as the function of the photon energy. Combining positive

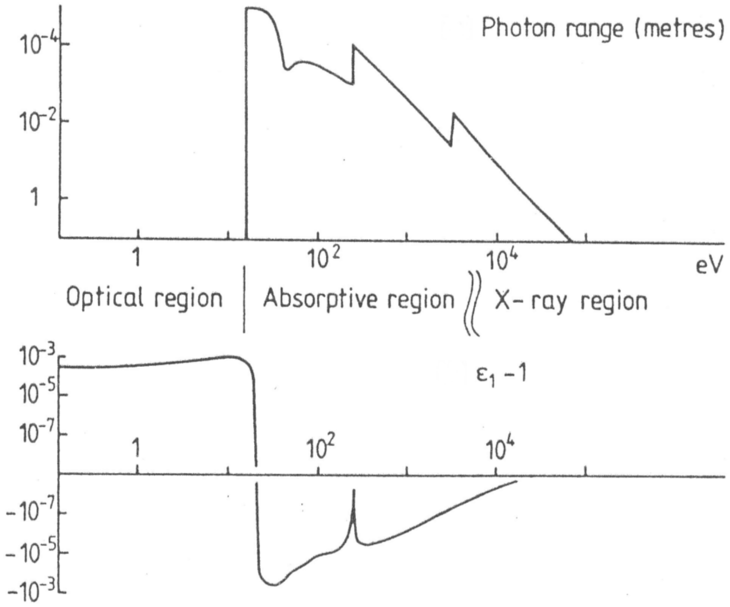

Figure 2.5: The complex dielectric constant $\varepsilon = \varepsilon_1 + i\varepsilon_2$ as a function of the photon energy for Argon (from [7]). The upper graph represents the absorptive part ε_2 expressed as photon range and the bottom one shows $\varepsilon_1 - 1$ with ε_1 being the polarisation part.

and negative frequencies, eq. 2.15 becomes (details of the full derivation are in [8])

$$\left\langle \frac{\mathrm{d}E}{\mathrm{d}x} \right\rangle = -\frac{1}{4\pi\varepsilon_0}\frac{2e^2}{\pi\beta^2}\int_0^\infty \mathrm{d}\omega \int \mathrm{d}k \left[\omega k(\beta^2 - \omega^2/k^2c^2)\mathrm{Im}\left(\frac{1}{\varepsilon\omega - k^2c^2}\right) - \frac{\omega}{kc^2}\mathrm{Im}\left(\frac{1}{\varepsilon}\right)\right]. \tag{2.16}$$

The only unknown parameter in eq. 2.16 is the complex permittivity ε, and more specifically the absorptive part ε_2. This quantity is conveniently expressed in terms of the generalised oscillator strength density $f(k, \omega)$

$$\varepsilon_2(k, \omega) = \frac{2\pi^2 N e^2}{mc} f(k, \omega), \tag{2.17}$$

where N is the atom density. This function $f(k, \omega)\,\mathrm{d}\omega$ represents the fraction of electrons coupling to the field with frequencies between ω and $\omega + \mathrm{d}\omega$ for a given wave number k [8, 52]. It can be expressed as a function of the photo-absorption cross-section $\sigma_\gamma(\omega)$, which is a measurable quantity. So the absorptive part of the complex permittivity can be written as

$$\varepsilon_2(k, \omega) = \frac{Nc}{\omega}\left[\sigma_\gamma(\omega)\mathrm{H}\left(\omega - \frac{\hbar k^2}{2m}\right) + \delta\left(\omega - \frac{\hbar k^2}{2m}\right)\int_0^\omega \sigma_\gamma(\omega')\,\mathrm{d}\omega'\right], \tag{2.18}$$

with H(x) the Heaviside function. The first and second terms of eq. 2.18 represent respectively the resonance and quasi-free part of the oscillator strength. The polarisation and absorptive part of ε are related by the Kramers-Kroning relation [8, 55]

$$\varepsilon_1 = 1 + \frac{2}{\pi}\mathcal{P}\int_0^\infty \frac{x\,\varepsilon_2(x)}{x^2 - \omega^2}\,\mathrm{d}x\,. \tag{2.19}$$

Injecting eq 2.18 in eq. 2.16 we obtain an expression for the energy loss [97, 8, 9]

$$\begin{aligned}\left\langle \frac{\mathrm{d}E}{\mathrm{d}x} \right\rangle = \frac{1}{4\pi\varepsilon_0}\frac{e^2}{\beta^2 c^2 \pi}\int_0^\infty & \left[N c\, \sigma_\gamma(\omega) \ln \left[\left(1-\beta^2\varepsilon_1\right)^2 + \beta^4 \varepsilon_2^2 \right]^{-1/2} \right. \\ & + \omega \left(\beta^2 - \frac{\varepsilon_1}{|\varepsilon|^2} \right) \arg(1-\beta^2\varepsilon^*) + N c\, \sigma_\gamma(\omega) \ln \frac{2 m_e c^2 \beta^2}{\hbar\omega} \\ & \left. + \frac{1}{\omega}\int_0^\omega \sigma_\gamma(\omega)\,\mathrm{d}\omega \right] \mathrm{d}\omega\,. \end{aligned} \tag{2.20}$$

We now interpret the energy loss semi-classically in terms of discrete collisions with energy transfer $E = \hbar\omega$ [8, 7].

$$\left\langle \frac{\mathrm{d}E}{\mathrm{d}x} \right\rangle = -\int_0^\infty N E \,\frac{\mathrm{d}\sigma}{\mathrm{d}E}\,\hbar\,\mathrm{d}\omega \tag{2.21}$$

with N the number of atoms per unit of volume and $\frac{\mathrm{d}\sigma}{\mathrm{d}E}$ the differential cross-section of the energy transfer from the particle to the medium. Equalling with eq. 2.20, we get an expression for the differential cross-section

$$\begin{aligned}\frac{\mathrm{d}\sigma}{\mathrm{d}E} = \frac{\alpha}{\beta^2\pi} & \left(\frac{\sigma_\gamma(E)}{E} \ln \left(\frac{1}{\sqrt{\left(1-\beta^2\varepsilon_1\right)^2 + \beta^4\varepsilon_2^2}} \right) + \frac{1}{N\hbar c}\left(\beta^2 - \frac{\varepsilon_1}{|\varepsilon|^2}\right)\arg(1-\beta^2\varepsilon^*) \right. \\ & \left. + \frac{\sigma_\gamma(E)}{E}\ln\frac{2 m_e c^2 \beta^2}{E} + \frac{1}{E^2}\int_0^E \sigma_\gamma(E_1)\,\mathrm{d}E_1 \right). \end{aligned} \tag{2.22}$$

With $\alpha = e^2/4\pi\varepsilon_0\hbar c$ is the fine structure constant. Eq. 2.22 is composed of four distinct terms:

- If we re-express $\beta' = v/u = \beta\sqrt{\varepsilon}$ and $\gamma' = (1-\beta'^2)^{1/2} = (1-\beta^2\varepsilon)^{1/2}$ with the velocity of light in the medium $u(\omega) = c/\sqrt{\varepsilon}$, we can recognize in the first term (with $\varepsilon_2 = 0$) the factor $\ln\left(\gamma'^2\right)$ responsible for the relativistic rise and saturation of the cross-section [8, 7].
- The second term in eq. 2.22 refers to the Cherenkov radiation [66, 8]:

$$N\left(\frac{\mathrm{d}\sigma}{\mathrm{d}E}\right)_{\check{\mathrm{C}}} = \frac{\alpha}{\hbar c}\left(1 - \frac{\varepsilon_1}{\beta^2|\varepsilon|^2}\right) = \frac{\alpha}{\hbar c}\sin^2\theta_{\check{\mathrm{C}}}. \tag{2.23}$$

- The third term comes from the resonance at energy transfer E.
- The fourth term is the Rutherford scattering concerning the quasi-free atomic electrons at energy transfer E. As σ_γ falls approximatively as $E^{-2.5}$ and because of the Thomas-Reiche-Kuhn sum rule [8, 97]

$$\int_0^\infty \sigma_\gamma(E)\,\mathrm{d}E = \frac{2\pi\alpha Z}{m_e} \tag{2.24}$$

  this term converges to pure Rutherford scattering $1/E^2$. In case of hard collisions the other terms vanishes and the cross-section is only driven by the Rutherford term [97]. This is the main process of production of δ-electrons. They are energetic and heavily scattered electrons, who may induce ionisation on their own. They are responsible for the tails in the probability of the number of electrons freed from the ionisation of a fast charged particle.

One could notice that the Cherenkov term does not depend on σ_γ. This is expected since Cherenkov radiations are produced by the whole medium rather than individual atoms.

In order to use eq. 2.22, we only need to know the photo-absorption cross-section of the considered medium. Such experimental data are now available for a large panel of media, and mostly centralised in database of the `HEED` simulation program [97].

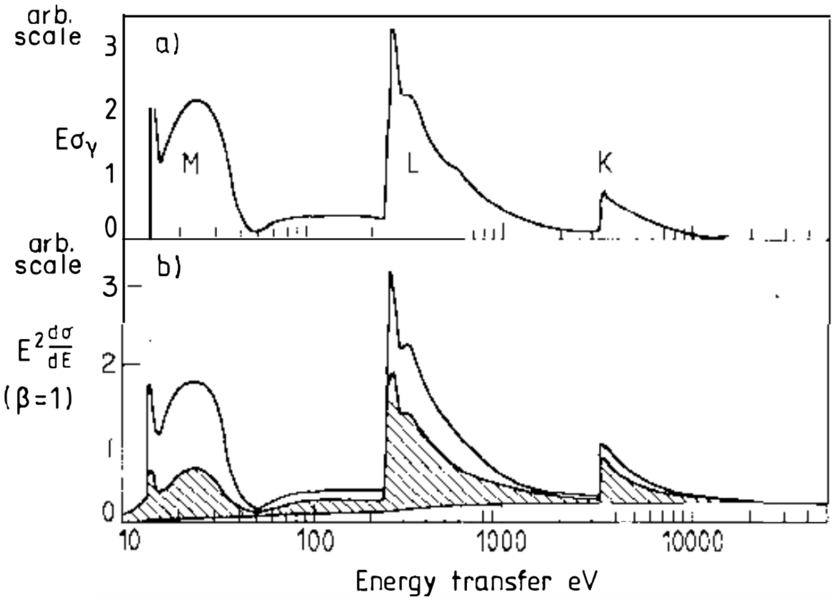

Figure 2.6: An example calculation with the PAI model for Argon as a function of the energy transfer. The upper graph is the experimental photo-absorption cross-section σ_γ, the bottom one is the PAI cross-section in the case $\beta = 1$. The upper unshaded curve is the contribution of the first two terms of eq. 2.22, the shaded term is from the third term and the lower unshaded part represent the Rutherford scattering. (From [8], part of figure 6.)

Figure 2.6 shows an example calculation of the PAI model in Argon gas as a function of the energy. The contribution of the K, L and M shells are clearly visible on the photo-absorption cross-section plot. The bottom part of the figure represents $\mathrm{d}\sigma/\mathrm{d}E$ from eq. 2.22 in the limit case $\beta = 1$. For this plot, from bottom to top, the areas under the curve represents the Rutherford Scattering, the third term in eq. 2.22 (resonance term) and the first two terms. We can clearly see that the Rutherford scattering produces a background under the other parts that grows with energy transfer E.

At the practical application of this model for the description of the signals from gaseous detectors one usually assumes that the amount of ionisation created after each energy transfer is approximately proportional to the transferred energy with some fluctuations. So in the end the ionisation distribution, ie the number of electron-ion pairs produced n, by an energy deposit Δ is given by

$$\Delta = n_i W \tag{2.25}$$

with W the mean work per pair production. This value depends only on the medium (density, composition ...) and the nature of the incident particle [54]. For example, in Argon $W = 26.4$ eV for 5.30 MeV α-particle, meaning we'll have a cluster containing $n_i \geqslant 1$ electron-ion pair for an energy transfer $\Delta \geqslant 26.4$ eV.

It is also interesting to note that W is greater than the ionisation potential I. This means that for argon an average of $W - I = 10.6$ eV is dissipated in various processes at the ionisation threshold.

2.3 Secondary particles and the Photo-Absorption Ionisation with Relaxation model (PAIR)

The PAI model has been widely used for many calculations about primary ionisation in gaseous detectors. It also has been implemented in Monte-Carlo simulation framework (such as `GEANT3`, `GEANT4`, `Garfield` ...). But this model is not sufficient if one is interested in the simulation of the detailed emission of secondary particles, as it only gives the energy transfer.

Secondary particles

The energy of the emitted secondary particles will depend on the atomic shell that have absorbed the transferred energy (or at least a part of it). If one assumes that the interaction is undergone by a single atomic electron rather than the whole atom itself, the ejected photo-electron carries an energy equals to the transferred energy minus the binding energy of the corresponding atomic shell.

This leaves the atom in an excited state, with one or more vacancies in its electronic shells. Those vacancies can be filled either by the emission of fluorescence photon or by relaxation Auger electrons. Those photons and electrons are considered as secondary particles and can lead to additional excitations or ionisations in the gas.

The Photo-Absorption Ionisation with Relaxation model

The cross-section for the transferred energy E described by the PAI model in eq. 2.22 gives only the probability for an incident particle to interact with the whole atom rather than a single atomic electron. So in order to modelise the emission of secondary particles eq. 2.22 has to be modified.

Smirnov [97] has introduced such a modification in the PAI model. If we keep the assumption that the transferred energy is absorbed by single atomic shells, eq. 2.22 has to be reinterpreted to take this into account. This model is called the Photo-Absorption Ionisation with Relaxation model (PAIR), in reference to the original PAI.

As eq. 2.22 depends on the photo-absorption cross-section of the whole atom, this term is modified to take into account absorption by atomic shells. It is reinterpreted by a sum of partial cross-sections, each corresponding to a particular shell [97]

$$\sigma_\gamma(E) \to f(n_a)\,\sigma_\gamma(E, n_a, n_s) \tag{2.26}$$

where n_a and n_s denote respectively the corresponding atom and shell. $f(n_a)$ is the fraction of the atom of a given species n_a in the gas with the straightforward condition

$$\sum_{n_a} f(n_a) = 1\ . \tag{2.27}$$

According to [97] the cross-section of the energy transfer from the particle to a particular shell of an atom, above ionisation threshold, is given by

$$\begin{aligned}\frac{\mathrm{d}\sigma(E,n_a,n_s)}{\mathrm{d}E} = \frac{\alpha}{\beta^2\pi}\Bigg(&\frac{f(n_a)\,\sigma_{\gamma i}(E,n_a,n_s)}{E}\ln\left(\frac{2\,m_e\,c^2\,\beta^2}{E\sqrt{\left(1-\beta^2\varepsilon_1\right)^2+\beta^4\varepsilon_2^2}}\right)\\ &+H(E-I_{\min})\frac{f(n_a)\,\sigma_{\gamma i}(E,n_a,n_s)}{\bar{\sigma}_\gamma(E)}\frac{1}{N\hbar c}\left(\beta^2-\frac{\varepsilon_1}{|\varepsilon|^2}\right)\arg(1-\beta^2\varepsilon^*)\\ &+H(E-I(n_a))R(E)\times\int_0^E f(n_a)\sigma_\gamma(E_1,n_a,n_s)\,\mathrm{d}E_1\Bigg)\end{aligned} \tag{2.28}$$

where $H(x)$ is the Heaviside function. There are several key differences with the original PAI equation. The first and third terms from eq. 2.22 have been merged into one and only the ionisation part of the photo-absorption cross-section, noted $\sigma_{\gamma i}$ is taken into account. Concerning the second term in eq. 2.22 related to Cerenkov radiation, it does not depend on σ_γ as it is a result of the whole media rather than specific atoms. As eq. 2.28 treats only ionisation, this term is neglected below the minimum ionisation threshold of the medium $I_{\min}$. Above ionisation threshold this term can no longer be interpreted as Cerenkov radiation and becomes numerically small (yet doesn't completely vanish); so it is distributed uniformly among the shells, where $\bar{\sigma}_\gamma$ is the mean photo-absorption cross section

$$\bar{\sigma}_\gamma = \sum_{n_a,n_s} f(n_a)\,\sigma_\gamma(E,n_a,n_s)\,. \tag{2.29}$$

Concerning the Rutherford term, the $1/E^2$ has been reinterpreted in a more precise form as it is only an approximation [97, 99, 17]

$$\begin{aligned}R(E) &= \frac{1}{E^2}\left(1-\frac{\beta^2 E}{E_{\max}}\right)\,,\\ E_{\max} &= \frac{2\,T_{\max}}{(1-\beta^2)}\end{aligned} \tag{2.30}$$

with $T_{\max}$ eq. 2.2. This term also depends on the total photo-absorption cross-section σ_γ (not the ionisation part) in order to retrieve the correct asymptotic behavior [97].

This model has been implemented in the `HEED` simulation program and is part of the simulation framework `GARFIELD` [38].

With the PAIR model one can modelise the absorption of the interaction energy by atomic shells, thus providing the means to compute the relaxation cascade of an atom left in an excited state because of the vacancies in its atomic shells. Most of the time the relaxation happens through emission of Auger electrons, as the probability of fluorescence is usually small [97]. If we consider a photo-ionisation in the K shell, the relaxation process follows such pattern [41]:

- If we consider the photo-ionisation occurred in the K shell (with binding energy E_{B_K}), the hole in this shell is then filled by an electron of the L shell (with binding energy E_{B_L}). The excitation energy $E_{B_K} - E_{B_L}$ is transfered to an electron of the L shell and if $E_{B_K} - E_{B_L} > E_{B_L}$ this electron is knocked out of the electron with an energy $E_{B_K} - 2E_{B_L}$.

- The two vacancies left in the L shell are then filled by the same process from the M shell, with the emission of two Auger electrons carrying an energy $E_{B_L} - 2E_{B_M}$.

In the `HEED` simulation program the vacancy in any given shell is filled by an electron from the next shell with an Auger electron emitted from that next shell. Then the two vacancies left in the next shell are filled by the outermost shell with another two Auger electron emitted [97].

Figure 2.7 shows the photo-absorption cross-section, as parametrised in the `HEED` database, for Argon, Neon, Helium and Xenon. For the Argon (fig. 2.7a) one clearly sees the rise of the cross-section on K, L and M shells (as expected we get the same behaviour than figure 2.6). Helium has only its first shell populated so one cannot distinguish any specific rise on its cross-section on figure 2.7c. Same idea for Neon as it doesn't have a M shell, on figure 2.7b there is only the rise due to the L shell. For Xenon, figure 2.7d, it becomes harder to distinguish the contributions from the individual shells. Figure 2.8 presents the photo-absorption cross-section for two gaseous mixtures commonly found in RPC. In this case it is also hard to tell the contribution from individual shells. One can remark that the cross-sections are very similar for the two compounds, the subtle variances between the two curves arise from the difference in proportion of $C_2H_2F_4$ as it is the ionising gas of the mixtures, ie the gas which has the lowest ionisation potential.

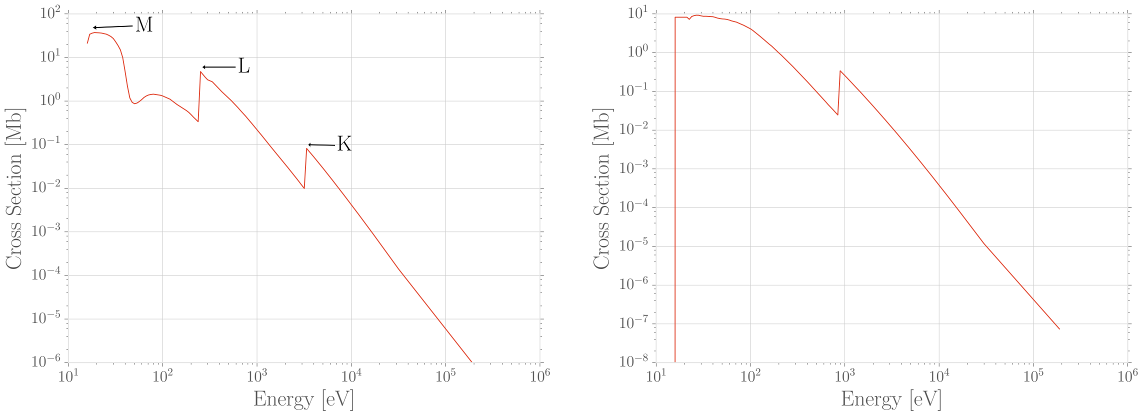

(a) Argon

(b) Neon

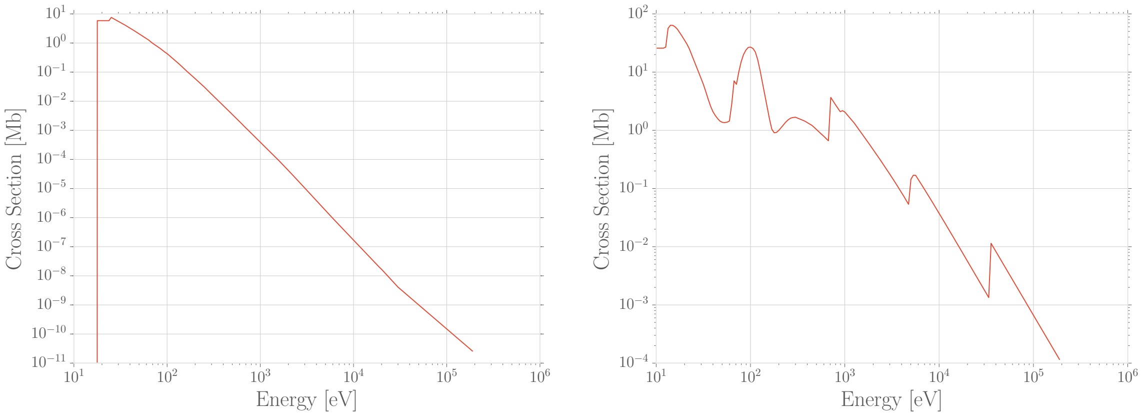

(c) Helium

(d) Xenon

Figure 2.7: Photo-absorption cross-section for some noble gases. Plotted with the HEED database.

The Jesse-Sadauskis effect

When small amounts of some other gases are added to an original mixture, there may be an increase in the amount of ionisation produced by the passage of a charged particle of

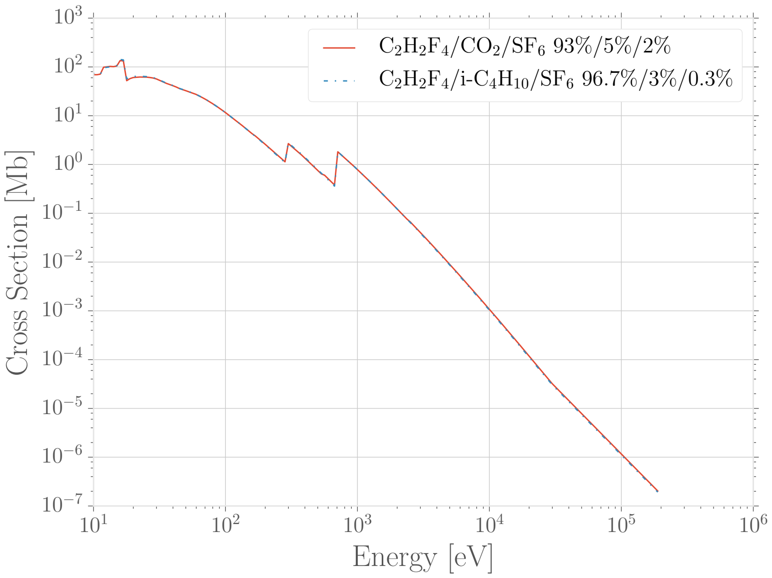

Figure 2.8: Photo-absorption cross-section for two gaseous mixtures commonly used in RPC. Plotted with the HEED database.

given energy. There is a correlation between the increase of ionisation and the ionisation potential and quantity of the foreign species. This phenomena is called the Jesse-Sadauskis effect [54, 57].

Simply put, the ionisation potential of a given gas is reduced when traces of a specie with a lower ionisation potential is present, as shown by figure 2.9. Then the excitation of one atom can give rise to ionisation of another atom with a smaller ionisation potential. This is only an over-simplification of the phenomena as one can see on figure 2.10, where a negative Jesse-Sadauskis effect is observed when Neon is added to Helium with $W_{\mathrm{He}} = 45.2$ eV and $W_{\mathrm{Ne}} = 39.3$ eV.

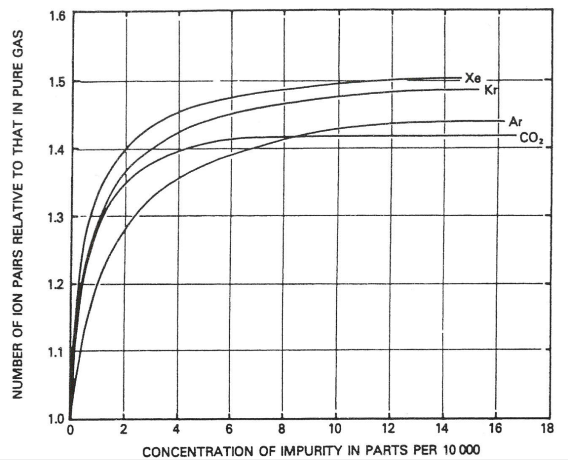

Figure 2.9: Relative ionisation as a function of impurities concentration (from [54]).

As one can remark in eq. 2.28 we do not take into account the contribution to the cross-section below the ionisation threshold, but excitation will still have an impact indirectly as it has an influence on the complex dielectric constant calculation. This is an approximation since the Jesse-Sadauskis effect can produce excitation-induced ionisation.

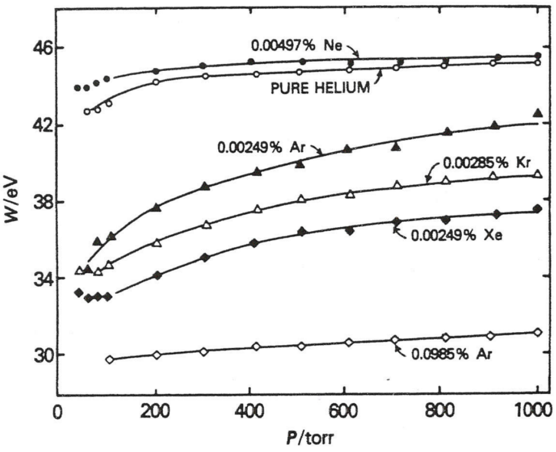

Figure 2.10: Evolution of the mean work per pair production for Helium with different impurities in various proportion as a function of gas pressure (1 torr = 133 Pa) (from [54]).

2.4 Primary ionisation distribution

Figure 2.11 shows the distribution of energy loss and the number of electrons produced by the passage of a 5 GeV/c muon in 0.12 cm of Argon, Helium and an RPC mixture $C_2H_2F_4$/i-C_4H_{10}/SF_6 96.7%/3%/0.3%. As one could expect from the Bethe formula (eq. 2.1) both histograms follow a Landau distribution in the three cases.

Due to their electronic structure the range of energy loss in Argon is very restrained (2 and 0.15 KeV respectively), as well as the distribution of the number of electrons produced. As helium atoms have their only shell fully populated, the probability for an energy transfer from the incident particle is quite small (see figure 2.11b), and when it occurs the energy lost is small. Therefore the distribution of electron produced in Helium is particularly narrow and most of the time no electrons are freed.

The RPC mixture ($C_2H_2F_4$/i-C_4H_{10}/SF_6 96.7%/3%/0.3%) presents a much wider range of energy loss and therefore bigger probability for electron production, with a most probable value around 17.

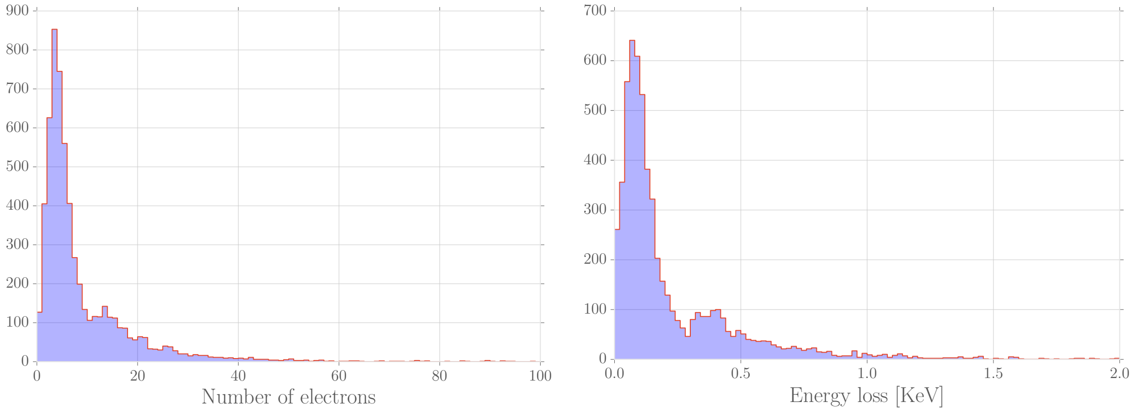

(a) Argon

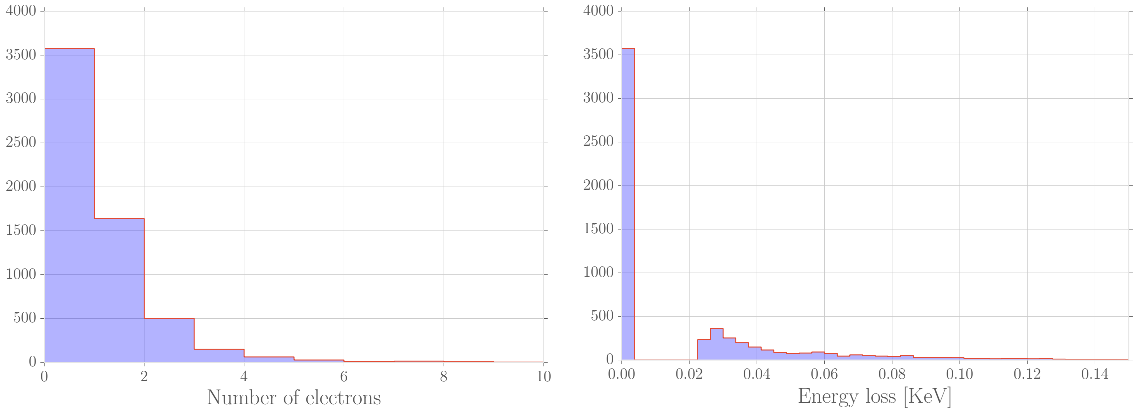

(b) Helium

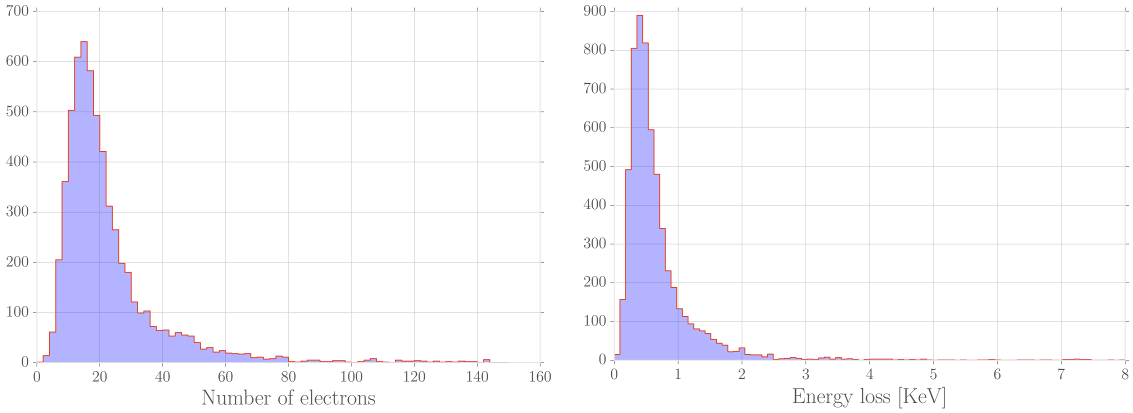

(c) $C_2H_2F_4$/i-C_4H_{10}/SF_6 96.7%/3%/0.3%

Figure 2.11: Distribution of the energy loss and the number of electrons produced by the passage of a 5 GeV/c muon in argon, helium and a mixture composed of $C_2H_2F_4$/i-C_4H_{10}/SF_6 96.7%/3%/0.3%. Computed with HEED.

Chapter 3

Electronic avalanches in gases

3.1 Choice of gaseous mixture

The gaseous mixture is one of the most vital part of an RPC as it influences many key characteristics; so it has to be chosen accordingly to usage. The mixture will have a strong impact on the primary ionisation, the amount of energy lost by a charged particle when it crosses the detector (see chapter 2). It will also impact the avalanche development and propagation that will be discussed further in this chapter.

Usually a gaseous mixture is composed of 3 gases, each one having its purpose:

1. an ionising gas, typically $\sim 95\%$ for RPCs. This is usually a gas with a low ionisation potential to produce electrons;
2. a UV quencher gas, typically $\sim 4\%$ for RPCs. It is used to absorb photons, in order to avoid the development of secondary avalanches started by photon and so avoiding false-positives;
3. an electron quencher gas, typically $\sim 1\%$ for RPCs. It is added in very small quantity to contain the avalanche and prevent it to spread and develop too much in order to suppress streamers and sparks.

A RPC gaseous mixture will vary on its composition depending on the target rate capability or the background noise tolerance. Nowadays one of the most common mixture used in High Energy Physics detectors is composed of Tetrafluoroethane (also denominated as forane R134a) $C_2H_2F_4$ as ionising gas, iso-butane i-C_4H_{10} as photon quencher and Sulphur hexafluoride SF_6 as electron quencher. It is the mixture used by the single-gap muon trigger system at CMS, ATLAS and ALICE at LHC, in the proportion 95.2%/4.5%/0.3%, 94.7%/5%/0.3% and 89.7%/10%/0.3% respectively [29, 28].

The use of F-based gas will become limited or even banned in the near future by demand of new European regulations for environment protection. The impact of such gases on the greenhouse effect is quantified by the Global Warmth Potential (GWP), normalised to the effect of CO_2 (GWP$= 1$). The European Community has prohibited the production and use of gas mixtures with GWP > 150. The $C_2H_2F_4$ and SF_6 gases expose a GWP of 1430 and 29800 respectively and have to be replaced. Tetrafluoropropene (HFO) is currently investigated to replace those gases as it presents a GWP of 4. However it currently cannot be used as the sole replacement in already active RPC as it cannot reach the same efficiency and quenching capacity than forane and SF_6 [14, 13, 63]. Furthermore the lack of study of HFO in the frame of High Energy Physics detectors and its non-existence in simulation program database such as `Magboltz` or `HEED` make the modelisation of RPC using this particular gas, as of today, impossible.

In this thesis we have been working mainly with the mixture used by the sDHCAL prototype of the CALICE collaboration [20] composed of forane, CO_2 (which is a common alternative to isobutane) and SF_6 in the proportion 93%/5%/2%. Otherwise indicated, this will be the default gaseous mixture used for our results.

3.2 Cluster distribution

As a first step in simulating a gaseous detector, one has to know the amount of ionisation deposited in the gas by the incident particle. The various processes occurring during an ionisation event have been discussed in chapter 2. We use the `HEED` simulation software [98] to modelise the primary ionisation produce by the passage of a charged particle through the detector.

By moving through the gas, a charged particle will provoke ionisation along its track. At each ionisation event we will have the production of electron clusters containing one or more electrons, depending on the amount of energy lost by the particle during the interaction (see eq. 2.28). So the amount of primary ionisation deposited in the detector can be characterized by the cluster density, ie the number of clusters produced by unit of length, and the probability distribution of the number of electrons per cluster.

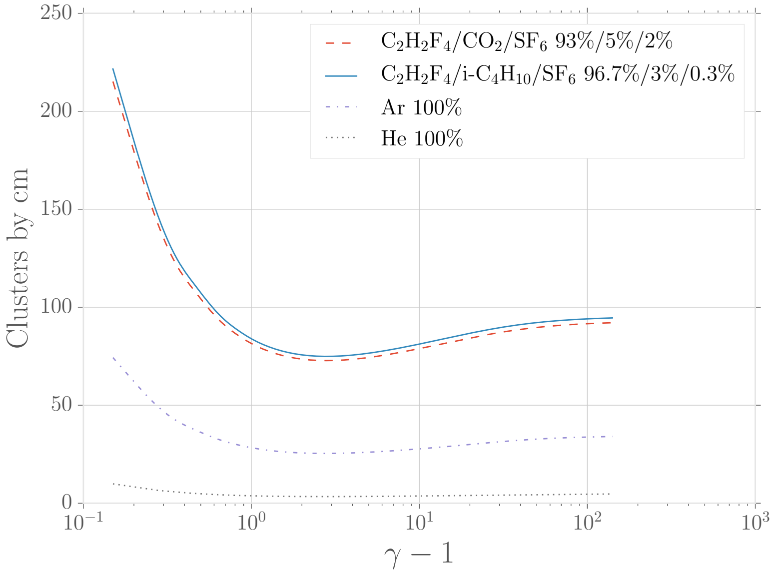

Figure 3.1: The cluster density for different gases, produced by the passage of muons.

Figure 3.1 presents the cluster density for different gases and gaseous mixtures produced by incident muons. As it is expected the curves exhibit the same behaviour as the energy loss given by the Bethe formula (see figure 2.2). In average a minimum ionising muon will produce 75 clusters per centimetre in commonly used RPC mixture. The figure 3.2 shows the probability distribution of the number of electrons freed by the passage of a muon with $p = 5$ GeV/c in 0.12 cm of several gases. As one can remark, most of the time there is only one electron produced (around 95% probability in helium and argon, and around 80% for both RPC mixtures). Except in helium, all distributions present small *bumps* which are directly related to the resonances due to the electronic structure of atoms in the photo-absorption cross-sections (see figures 2.7 and 2.8). As the photo-absorption cross-section of helium is smooth, so is its distribution.

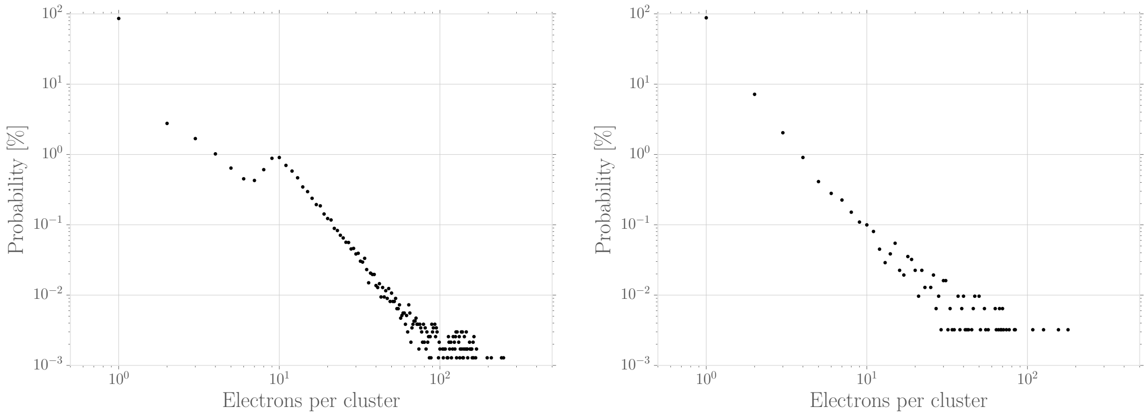

(a) Argon **(b)** Helium

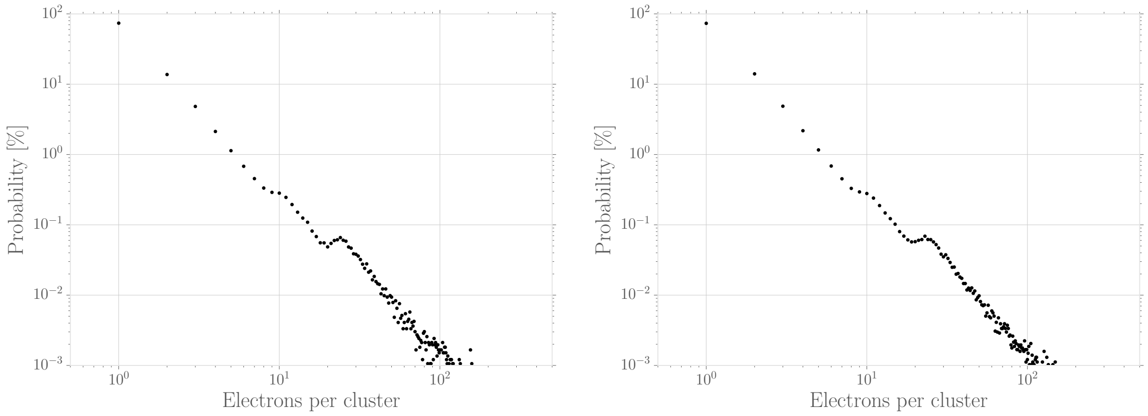

(c) $C_2H_2F_4$/i-C_4H_{10}/SF_6 96.7%/3%/0.3% **(d)** $C_2H_2F_4$/CO_2/SF_6 93%/5%/2%

Figure 3.2: Distribution of the number of electrons produced by the passage of a 5 GeV/c muon in 0.12 cm of argon, helium and two RPC mixtures. Values are computed with `HEED`.

To summarise, the passage of a 5 GeV/c muon in 0.12 cm of a commonly used RPC gaseous mixture will produce on average about 8.5 clusters containing between 1 and 2 electrons, so an average total between 10 and 25 electrons freed in the gas.

3.3 Electronic avalanche development and propagation

In this section we will discuss the model used for the avalanche development and its propagation in a RPC.

3.3.1 Electron multiplication and attachment

Each electron freed by the passage of a charged particle will drift under the influence of the electric field and multiply by interacting with gas molecules, leading to an electronic avalanche that will grow until it has reached the RPC's anode. For each electron there is a probability to multiply and a probability to get attached to a gas molecule. If we make the assumption that the ionisation probability is independent of the history of previous collisions, the avalanche can be characterised by the Townsend coefficient α and attachment coefficient η. These two parameters represent in some way the mean free path for ionisation and attachment. Figure 3.3 shows the evolution of both coefficients with the

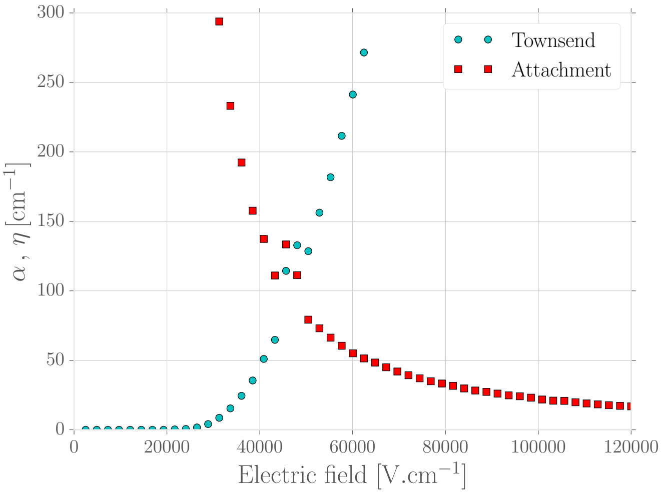

(a) $C_2H_2F_4/CO_2/SF_6$ 93%/5%/2%

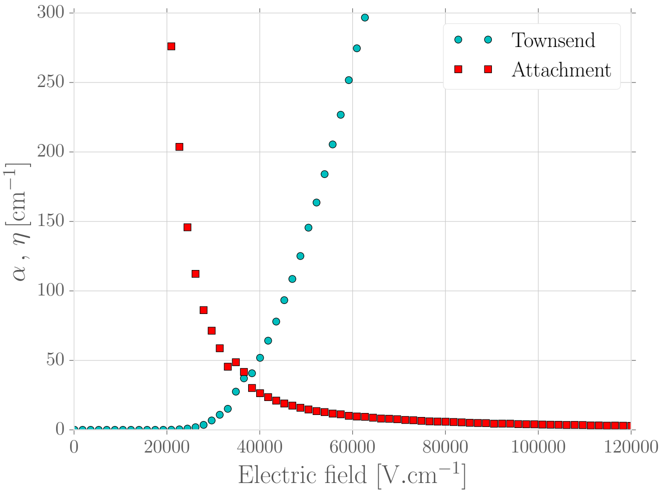

(b) $C_2H_2F_4$/i-C_4H_{10}/SF_6 96.7%/3%/0.3%

Figure 3.3: Townsend and attachment coefficients for two RPC mixtures, for $T = 296.15$ K and $P = 1013$ mBar, computed with `Magboltz` [16].

electric field. If we consider one electron, the probability that it multiplies is simply αdz, and the probability that it gets attached is ηdz. This can be generalised to any number of electrons, as shown in eq. 3.1.

$$\begin{array}{rlrl} n=1 \rightarrow n=2 & \alpha dz & n=1 \rightarrow n=0 & \eta dz \\ n=2 \rightarrow n=3 & 2\alpha dz & n=2 \rightarrow n=1 & 2\eta dz \\ n=3 \rightarrow n=4 & 3\alpha dz & n=3 \rightarrow n=2 & 3\eta dz \\ & \vdots & & \\ n \rightarrow n+1 & n\alpha dz & n \rightarrow n-1 & n\eta dz \end{array} \tag{3.1}$$

So if we consider an avalanche containing n electrons at position z, then the probability that it contains $n+1$ electrons at $z+dz$ is $n\alpha\, dz$. With the same arguments, the probability that one electron gets attached is $n\eta\,\mathrm{d}z$. Then the average number of electrons $\bar{n}$ and positive ions $\bar{p}$ are given by the relations [76, 90]

$$\frac{\mathrm{d}\bar{n}}{\mathrm{d}z} = (\alpha - \eta)\,\bar{n}, \tag{3.2}$$

$$\frac{\mathrm{d}\bar{p}}{\mathrm{d}z} = \alpha\bar{n}. \tag{3.3}$$

With the initial conditions $\bar{n}(0) = 1$ and $\bar{p}(0) = 0$ those equations yield

$$\bar{n}\,(z) = e^{(\alpha-\eta)z}, \tag{3.4}$$

$$\bar{p}\,(z) = \frac{\alpha}{\alpha - \eta}\left(e^{(\alpha-\eta)z} - 1\right). \tag{3.5}$$

Then the average number of negative ions is $\bar{p} - \bar{n}$ due to the total charge conservation in the process.

Now that we have an expression for the average number of electrons produced by an incident particle, we need the statistical distribution for the expected number of electrons. Different models for the stochastic nature of avalanche multiplication have been proposed and studied in the past 60 years.

The Furry model

A simple model has been used in the 50's where no attachment was considered. It is actually derived from a model proposed in 1937 by Furry to study the fluctuation of the size of electromagnetic cascades from cosmic-rays in lead ($\gamma \to ee$, $e \to \gamma e$ processes), which shares the same mathematical structure of a Townsend avalanche ($e \to ee$) [37]. In this model we consider that the probability for an electron traversing the distance $\mathrm{d}t$ to multiply into two electrons is simply $\mathrm{d}t = \alpha\,\mathrm{d}z$.

With this assumption we can write the differential equations for the probabilities to have $1, 2, \cdots, n$ electrons at position t

$$\begin{aligned}
\frac{\mathrm{d}}{\mathrm{d}t}P(1,t) &= -P(1,t),\\
\frac{\mathrm{d}}{\mathrm{d}t}P(2,t) &= -2P(2,t) + P(1,t),\\
&\vdots\\
\frac{\mathrm{d}}{\mathrm{d}t}P(n,t) &= -nP(n,t) + (n-1)P(n-1,t).
\end{aligned} \tag{3.6}$$

The first equation means that between t and $t + \mathrm{d}t$ the probability of having still one electron has diminished by $\mathrm{d}t$ times the initial probability $P(1,t)$. With the same idea for the second, we have a diminution of the probability with a factor 2 because there is 2 electrons that can initiate an avalanche on distance $\mathrm{d}t$ but also we can get 2 electrons from 1 hence the positive contribution of $P(1,t)$. The n-th order can be inferred from the pattern described by the previous equations.

Using the boundary conditions $P(1,0) = 1$ and $P(n,0) = 0$ for $n > 1$ and by successive integration we have

$$P(1,t) = e^{-t}; \quad P(2,t) = e^{-t}(1 - e^{-t}); \quad \cdots; \tag{3.7}$$

and with mathematical induction we get

$$P(n,t) = e^{-t}(1 - e^{-t})^{n-1}. \tag{3.8}$$

Replacing t by αz eq. 3.8 becomes

$$P(n,z) = \bar{n}^{-1}(1-\bar{n}^{-1})^{n-1}, \tag{3.9}$$

with $\bar{n} = e^{\alpha z}$ the average number of electrons when no attachment is considered. In the case $\bar{n} \gg 1$ eq. 3.9 can be approximated to

$$P(n,z) = \bar{n}^{-1} e^{-\frac{n}{\bar{n}}} \tag{3.10}$$

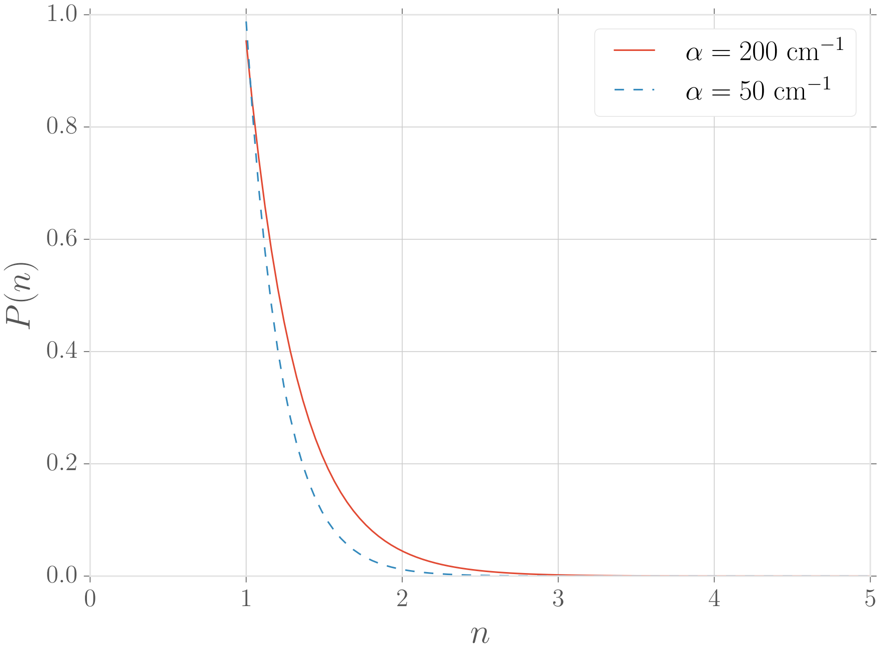

Figure 3.4: Probability for an electron to multiply to n electrons according to the Furry model (eq. 3.9), for $\delta z = 2.4\,\mu\text{m}$

The Furry formulation indicates that the probability to have an avalanche of size n decreases exponentially and that the fluctuations of n around the average $\bar{n}$ are important. The most probable value is $n = 1$ at a given distance dz. This is shown on figure 3.4. This is not an intuitive result but becomes clear from the schematic description of figure 3.5. For this simplified case we set d$z = 1$. Then for any electron the probability to multiply is α and the probability of no multiplication is $1 - \alpha$. Thus, after 4 steps and starting with one electron, we have

$$\begin{aligned} P(n=4) &= \alpha^3, \\ P(n=3) &= 3\alpha^2(1-\alpha), \\ P(n=2) &= 3\alpha(1-\alpha)^2, \\ P(n=1) &= (1-\alpha)^3. \end{aligned} \tag{3.11}$$

If we take an infinitesimal distance drifted between two steps δz, then the probability for ionisation is small so that we can neglect the successive powers of α. Eq. 3.11 simplifies to

$$\begin{aligned} P(n=4) &\sim 0, \\ P(n=3) &\sim 0, \\ P(n=2) &= 3\alpha, \\ P(n=1) &= 1-3\alpha. \end{aligned} \tag{3.12}$$

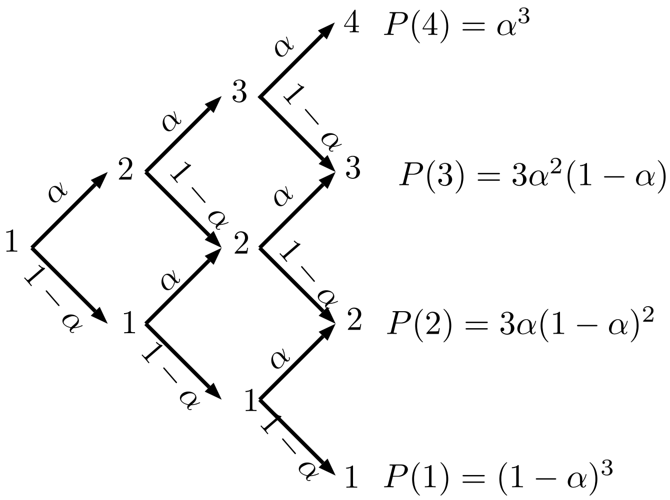

Figure 3.5: Schematic representation of an electron multiplication according to the Furry model. We simplified the process by taking $\mathrm{d}z = 1$ so $\mathrm{d}t = \alpha$.

And the most probable value is for $n = 1$. This makes sense because if the most probable value was for $n > 1$ then the avalanche growth would be tremendous and the number of electrons quickly would explode.

It is also important to notice that we consider that each electron has the same probability to ionise while traversing the distance $\mathrm{d}z$, and that this probability is independent of the path travelled from the previous ionizing collision. This last assumption leads to the condition that distance $s = U_i/E$, the minimum distance for an electron in an electric field E to gain enough energy for ionising the molecule with an ionising potential U_i, has to be small before the mean free path for ionisation $x_0 = 1/\alpha$ [39].

The Polya distribution

During the avalanche, the number of charge may become important enough to disturb the locally multiplication mechanisms. This is not taken into account in the Furry model. Another model for avalanche multiplication uses a Polya distribution (negative binomial distribution). In this model the probability of ionisation depends on the size of the avalanche itself, thus taking into account the perturbation of the multiplication processes. The Townsend coefficient is simply redefined as [32]

$$\alpha(n, z) = \alpha(z)\left(1 + \frac{\theta}{n}\right), \qquad n > 0 \tag{3.13}$$

where θ is an empirical parameter. Then the probability to have an avalanche of size n at position z is

$$P(n, z) = \frac{(1+\theta)}{\bar{n}}\frac{1}{\theta!}\left(\frac{(1+\theta)\,n}{\bar{n}}\right)^{\theta} e^{-\frac{(1+\theta)n}{\bar{n}}} \tag{3.14}$$

The limit case $\theta \to 0$ leads to the Furry distribution eq. 3.10.

It was pointed out that the dependence of the size of the avalanche in the probability of ionisation lacks physical interpretation [77, 90]. Eq. 3.14 doesn't take into account attachment processes, just as the Furry model eq. 3.9. Also the presence of empirical parameter that needs to be fine-tuned to existing data is incompatible with our objective of a full RPC simulation, relying on only physical mechanisms and not on ad-hoc parameters.

The Riegler-Lippmann-Veenhof model

In this work we use another model described by Riegler, Lippmann and Veenhof [77, 90] which is a continuation of the model of avalanche in electro-negative gases developed by Legler [76]. This is an expansion of the Furry model where we consider the attachment process.

In this model the probability $P(n,z)$ for an avalanche started by one electron to contain n electrons after the propagation on the distance z is defined through

$$\begin{aligned} P(n,z) = {} & P(n-1,z)\,(n-1)\,\alpha \mathrm{d}z\,(1-(n-1)\,\eta \mathrm{d}z) \\ & + P(n,z)\,(1-n\alpha \mathrm{d}z)\,(1-n\eta \mathrm{d}z) \\ & + P(n,z) n\alpha\, \mathrm{d}z\, n\eta\, \mathrm{d}z \\ & + P(n+1,z)\,(1-(n+1)\,\alpha \mathrm{d}z)\,(n+1)\,\eta \mathrm{d}z. \end{aligned} \tag{3.15}$$

This equation gives the possibilities to have n electrons at $z+\mathrm{d}z$. The first line represents the probability there is $n-1$ electrons, one multiplies and none gets attached. The second line gives the probability there is n electrons at z, none multiplies and none gets attached. It is the same case for the third line where one electron multiplies and another one gets attached. Finally the fourth line is the probability to have $n+1$ electrons at z and one gets attached and none multiplies. From there the differential probability can be derived, and limiting at the first order of dz we have

$$\frac{\mathrm{d}P(n,z)}{\mathrm{d}z} = -P(n,z)n\,(\alpha+\eta) + P(n-1,z)\,(n-1)\,\alpha + P(n+1,z)\,(n+1)\,\eta. \tag{3.16}$$

One can recognise in eq. 3.16 the differential equations of the Furry model (eq. 3.6) if we put $\eta = 0$ and define $\mathrm{d}t = \alpha\,\mathrm{d}z$.

From eq. 3.16 we can derive the general formulation for the probability for an avalanche of size n at position z [90, 76]

$$P(n,z) = \begin{cases} k\frac{\bar{n}(z)-1}{\bar{n}(z)-k}, & n=0 \\ \bar{n}(z)\left(\frac{1-k}{\bar{n}(z)-k}\right)^2 \left(\frac{\bar{n}(z)-1}{\bar{n}(z)-k}\right)^{n-1}, & n>0 \end{cases} \tag{3.17}$$

where $\bar{n}(z)$ is still from eq. 3.4, $k = \frac{\eta}{\alpha}$ and its variance is

$$\sigma^2(z) = \left(\frac{1+k}{1-k}\right)\bar{n}(z)\,(\bar{n}(z)-1)\,. \tag{3.18}$$

In the case $\alpha = \eta$ or $\alpha = 0$ distribution from eq. 3.17 becomes undefined [77, 90]. These two cases are important when we consider the space-charge effects. For $\alpha = \eta$ the probability distribution becomes

$$P(n,z) = \begin{cases} \frac{\alpha z}{1+\alpha z}, & n=0 \\ \frac{1}{(1+\alpha z)^2}\left(\frac{\alpha z}{1+\alpha z}\right)^{n-1}, & n>0 \end{cases} \tag{3.19}$$

and its variance is

$$\sigma^2(z) = 2\alpha z. \tag{3.20}$$

For $\alpha = 0$ the probability distribution becomes

$$P(n,z) = \begin{cases} 1-e^{-\eta z}, & n=0 \\ e^{-\eta z}, & n=1 \end{cases} \tag{3.21}$$

and its variance is

$$\sigma^2(z) = e^{-2\eta z}\,(e^{\eta z}-1)\,. \tag{3.22}$$

In this case the probability for $n > 1$ is null as $\alpha = 0$, ie the probability for ionisation is null.

From eqs. 3.17, 3.19 and 3.21 we can generate random numbers to simulate the multiplication and attachment of electrons. To generate a random number from eq. 3.17 we use

$$n = \begin{cases} 0, & s < k\frac{\bar{n}(z)-1}{\bar{n}(z)-k} \\ 1 + \ln\left(\frac{(\bar{n}(z)-k)(1-s)}{\bar{n}(z)(1-k)}\right)\frac{1}{\ln\left(1-\frac{1-k}{\bar{n}(z)-k}\right)}, & s > k\frac{\bar{n}(z)-1}{\bar{n}(z)-k} \end{cases} \qquad \alpha, \eta > 0 \tag{3.23}$$

where s is a random number in the interval $[0, 1)$. In the same way, to generate a random number from eq. 3.19 we use

$$n = \begin{cases} 0, & s < \frac{\alpha x}{1+\alpha x} \\ 1 + \ln\left[(1-s)\left(1+\alpha x\right)\right]\frac{1}{\ln\left(\frac{\alpha x}{1+\alpha x}\right)}, & s > \frac{\alpha x}{1+\alpha x} \end{cases} \qquad \alpha = \eta. \tag{3.24}$$

And to generate a random number from eq. 3.21 we use

$$n = \begin{cases} 0, & s < e^{(-\eta x)} \\ 1, & s > e^{(-\eta x)} \end{cases} \qquad \alpha = 0. \tag{3.25}$$

3.3.2 Electron diffusion and drift

The energy distribution of a free electron cloud in a gas follows a Maxwell-Boltzmann distribution with a mean defined by the thermal energy of the cloud

$$\langle E \rangle = \frac{3}{2}kT \tag{3.26}$$

with k the Boltzmann constant and T the temperature of the gas in Kelvin. The diffusion that undergoes a free electron in a gas is due to random collisions with the gas molecules. If the gas is not influenced by an electric field, then the diffusion is isotropic and follows a Gaussian distribution. An initial point-like electron cloud at $\vec{r_0}$ will follows, at time t, the density distribution [77]

$$\varphi(\vec{r}, t) = \frac{1}{\left(\sqrt{2\pi}\sigma(t)\right)^3}\exp\left(-\frac{(\vec{r}-\vec{r_0})^2}{2\sigma^2(t)}\right). \tag{3.27}$$

The sigma of this distribution is defined by

$$\sigma^2 = 2\overline{D}t \tag{3.28}$$

with $\overline{D}$ being the mass diffusivity in m^2/s (SI units).

When a constant electric field is applied to the gas, the electron cloud undergoes a constant drift motion in addition to the thermal diffusion. When there is no magnetic field, as it is the usually case in RPCs, the motion direction follows the electric field lines. From a microscopic point of view an electron will move under the influence of the electric field and collide with gas molecules. Between two collisions this electron drifts on the distance δz and gains a kinetic energy $T = e_0 \, |\vec{E}| \, \delta z$, with e_0 being the electron charge and $|\vec{E}|$ the intensity of the electric field. After the collision, the electron is slowed down and some of its energy is lost. In the same way, the electron will gain energy until the next collision, then will be slowed down again and so on. On a macroscopic scale, one will observe an electron moving with a constant velocity v_D, which is the velocity of the electron averaged over a large number of collisions, which depends on E/p. This quantity represents the electric field reduced by the gas pressure, it is a usual parameter to describe RPC characteristics. Figure 3.6 shows the evolution of the drift velocity in two RPC

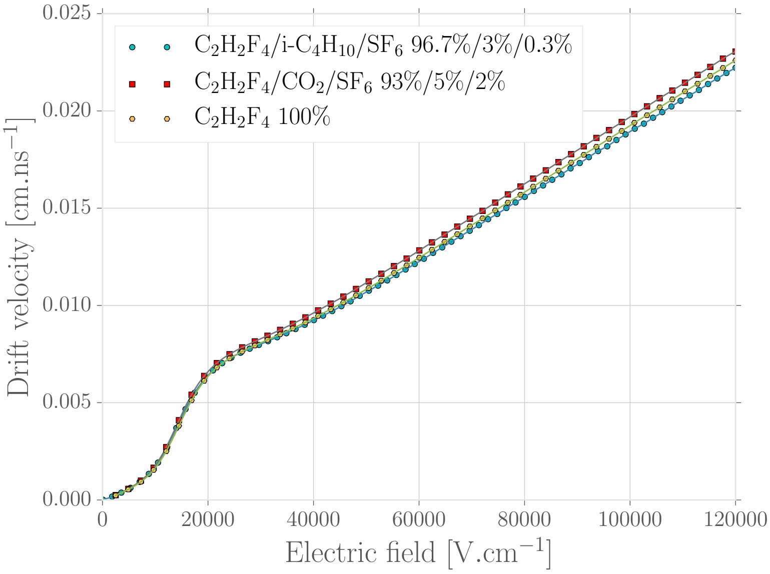

Figure 3.6: Electron drift velocity in two RPC gaseous mixtures and pure $C_2H_2F_4$. The temperature of the gas is $T = 296.15$ K and the pressure $P = 760$ Torr.

mixtures with the electric field. Those values are computed with `Magboltz` 9.01 [16]. This is a typical regime for drift velocity in RPCs, but this is not an universal behaviour for gaseous detectors. For instance in drift chamber, on work in region v_D is almost constant with respect to E.

As the presence of an electric field implies the addition of a constant drift motion to the thermal diffusion, the diffusion becomes anisotropic. We can separate it in two distinct terms, a longitudinal term and a transverse term. We can assume a rotational symmetry around the electric field axis for the electron cloud, and using cylindrical coordinates we obtain from eq. 3.27 [77]

$$\varphi(r, z, t) = \frac{1}{\sqrt{2\pi}\sigma_L\sigma_T^2} \exp\left(-\frac{(z - z_0)^2}{2\sigma_L^2} - \frac{(r - r_0)^2}{2\sigma_T^2}\right). \tag{3.29}$$

One can remark an additional factor 2π in the normalisation part of eq. 3.29. It comes from the integration over ϕ because of the rotational symmetry. $\sigma_{L,T}$ denotes the longitudinal and transverse parts of the variance and is defined (from eq. 3.28)

$$\sigma_{L,T}^2 = \overline{D}_{L,T}\, t. \tag{3.30}$$

Assuming a constant drift velocity we can introduce a new diffusion coefficient $D_{L,T}$ [77]. So with $v_D = l/t$ eq. 3.30 becomes $\sigma_{L,T}^2 = 2\overline{D}_{L,T} l / v_D = D_{L,T}^2\, l$ with $D_{L,T} = \sqrt{2\overline{D}_{L,T}/v_D}$ in $\sqrt{\text{m}}$. Using this and separating eq 3.29 in two specific parts, we have

$$\varphi_L(z, t) = \frac{1}{\sqrt{2\pi l}\, D_L} \exp\left(-\frac{(z - z_0)^2}{2D_L^2 l}\right), \tag{3.31a}$$

$$\varphi_T(r, t) = \frac{1}{D_T^2\, l} \exp\left(-\frac{(r - r_0)^2}{2D_T^2 l}\right). \tag{3.31b}$$

Both equations define the density distribution of an electron cloud in the longitudinal and transverse plane (parallel and perpendicular to the electric field lines, respectively) due to the diffusion of electrons with the gas molecules. Figure 3.7 is a plot of the diffusion coefficients as a function of the electric field, computed with `Magboltz` 9.01.

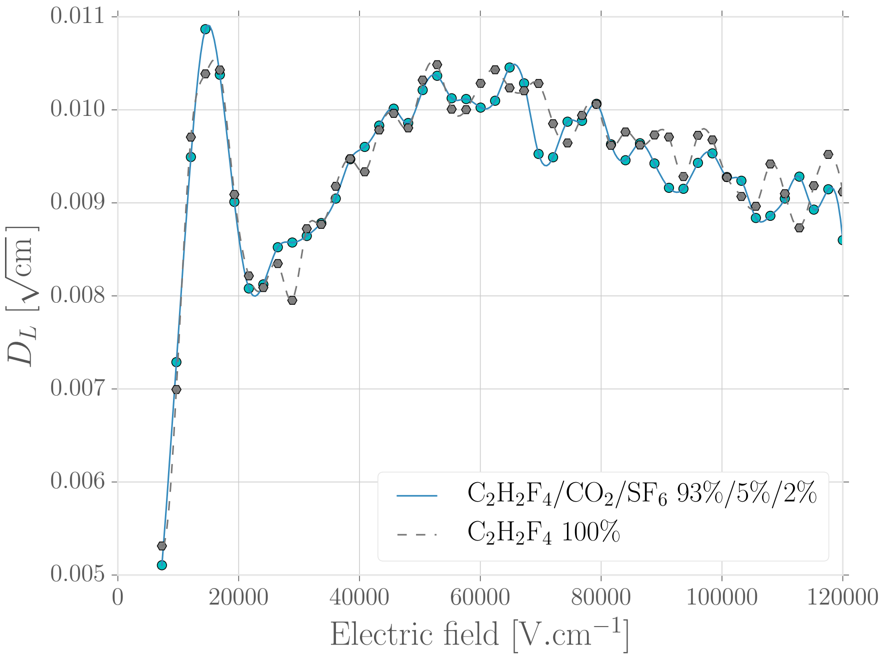

(a) Longitudinal diffusion coefficient

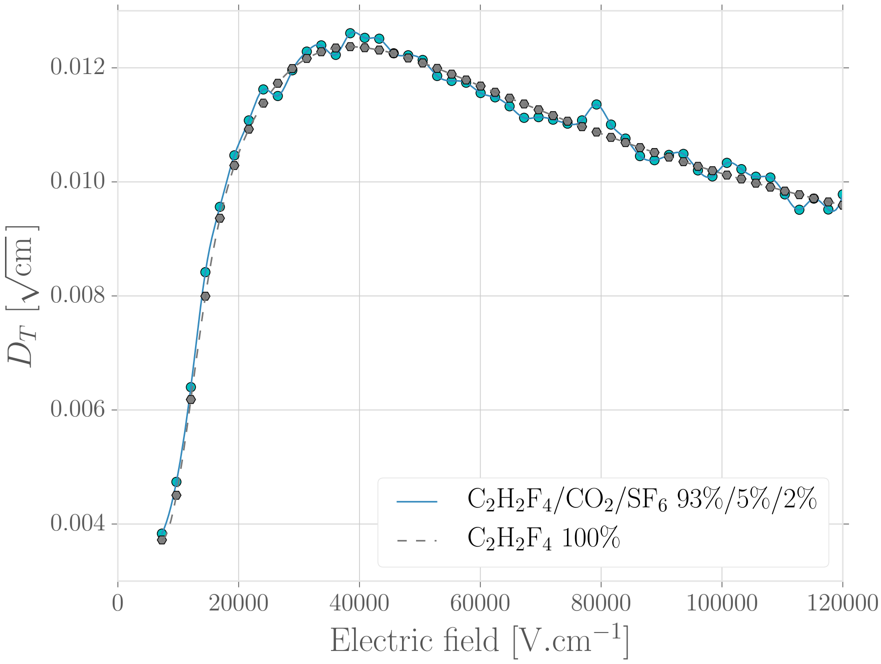

(b) Transverse diffusion coefficient

Figure 3.7: Longitudinal and transverse diffusion coefficients for $C_2H_2F_4$ 93%/5%/2% and pure isobutane $C_2H_2F_4$. The pressure is $P = 760$ Torr and the temperature $T = 296.15$ K

3.4 Influence of an avalanche on the electric field

Each charged particle induces its own electric field. When the electron density inside the detector becomes high enough, it influences the electric field applied between the plates, as it is illustrated by figure 3.8. This is the so called space charge effect. As a consequence, the Townsend and attachment coefficients, but also the drift velocity and the diffusion coefficients, are not uniform in the gas gap and this affects the development of the avalanche.

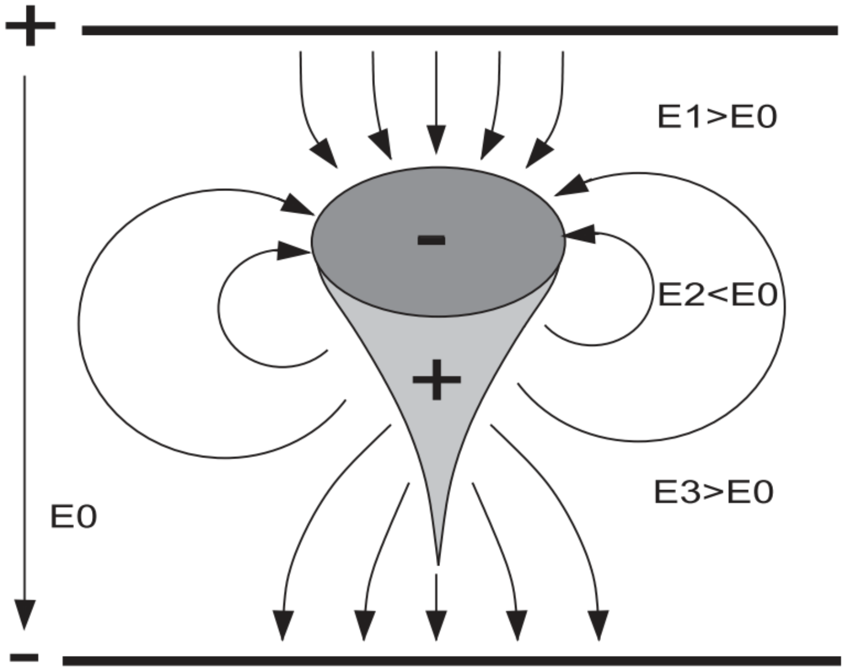

Figure 3.8: Schematic view of an electronic avalanche during its propagation. The field at the tip and bottom of the avalanche are stronger whereas the field at its core is reduced. (From [78])

In order to get an estimation of such an effect on the total electric field, we can make the rough approximation that all the charges lay in a sphere of radius r_d. Using the Gauss theorem, the electric field of this sphere is

$$E = \frac{e_0\, n_e}{4\pi\, \varepsilon_0\, r_d^2} \qquad r = r_d, \tag{3.32a}$$

$$E = \frac{e_0\, n_e}{4\pi\, \varepsilon_0\, r^2} \qquad r > r_d. \tag{3.32b}$$

Taking $n_e = 10^6$ for the number of electrons and $r_d = 0.1$ mm, we have $E = 1.5$ kV/cm on the sphere's surface. This represents about 3% of a typical RPC electric field, and in a typical RPC mixture this yields a $\sim 14\%$ change in the Townsend and attachment coefficients [77].

In order to accurately take into account the space charge effect, we need to compute the contribution to the total electric field from each charge in the gas.

3.4.1 Electric potential of a free point charge

In this section we will discuss an analytic solution for the electric potential produced by a point charge in a three layer geometry, like an RPC. We won't detail the derivation itself as it is not relevant in this study. The full derivation can be found in [46].

We consider the RPC as an infinite plane capacitor, made of three homogeneous parallel dielectric layers. The figure 3.9 presents the geometry of the capacitor. The point

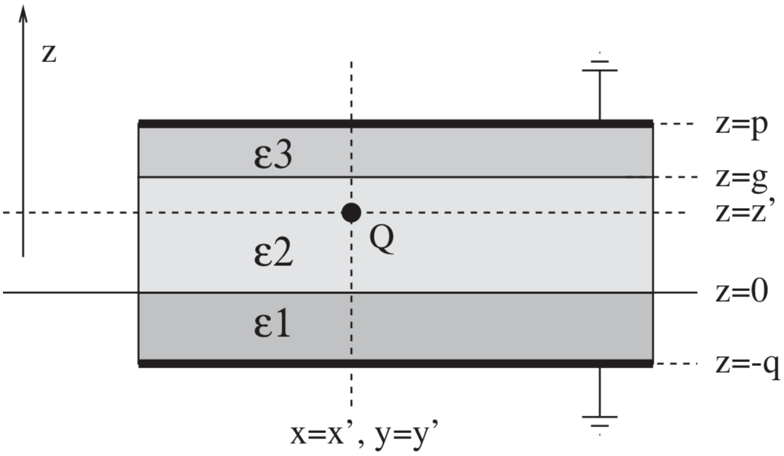

Figure 3.9: Geometry of the three layers capacitor. The point charge Q is present at position (x', y', z'). (From [47])

of observation is located at (x, y, z) and the point charge is located at position (x', y', z'). The first and third layers in figure 3.9 correspond to the resistive plates of a RPC. The second layer represents the gas gap located at $g \leq z \leq 0$, where g is the gap width. The dielectric permittivity of each layer is defined by $\varepsilon_i = \varepsilon_0 \, \varepsilon_{r_i}$, where ε_{r_i} is the relative dielectric constant of layer i and ε_0 is the vacuum dielectric constant. Using cylindrical coordinates, the distance R between the point of observation located at $\vec{r}$ and the point charge located at $\vec{r}\,'$ is defined by

$$\begin{aligned} R^2 &= |\vec{r} - \vec{r}\,'|^2 = (x - x')^2 + (y - y')^2 + (z - z')^2 \\ &= r^2 - 2rr' \cos(\phi - \phi') + r'^2 + (z - z')^2 \\ &= P^2 + (z - z')^2. \end{aligned} \tag{3.33}$$

The potential of a point charge located in the second layer, i.e. the gas gap of a RPC, with $g \leq z \leq 0$ follows [47, 46]

$$\begin{aligned} \Phi\left(r, \phi, z, r', \phi', z'\right) = \frac{Q}{4\pi\varepsilon_0} \Bigg[& \frac{1}{\sqrt{P^2 + (z - z')^2}} \\ & - \frac{\varepsilon_1 - \varepsilon_2}{(\varepsilon_1 + \varepsilon_2)\sqrt{P^2 + (z + z')^2}} \\ & - \frac{\varepsilon_3 - \varepsilon_2}{(\varepsilon_3 + \varepsilon_2)\sqrt{P^2 + (2g - z - z')^2}} \\ & + \frac{1}{(\varepsilon_1 + \varepsilon_2)(\varepsilon_2 + \varepsilon_3)} \int_0^\infty \mathrm{d}\kappa \, J_0(\kappa P) \, \frac{R(\kappa, z, z')}{D(\kappa)} \Bigg]. \end{aligned} \tag{3.34}$$

J_0 is the Bessel function of order 0. The functions $R\left(\kappa, z, z'\right)$ and $D\left(\kappa\right)$ are given by

$$\begin{aligned}
R\left(\kappa, z, z'\right) = {} & \left(\varepsilon_1+\varepsilon_2\right)^2\left(\varepsilon_2+\varepsilon_3\right)^2\left[e^{\kappa(-2p-2q+z-z')}+e^{\kappa(-2p-2q-z+z')}\right] \\
& -\left(\varepsilon_1+\varepsilon_2\right)^2\left(\varepsilon_2-\varepsilon_3\right)^2 e^{\kappa(-4g-2q+z+z')} \\
& -4\varepsilon_1\varepsilon_2\left(\varepsilon_2+\varepsilon_3\right)^2 e^{\kappa(-2q-z-z')} \\
& -\left(\varepsilon_1-\varepsilon_2\right)^2\left(\varepsilon_2+\varepsilon_3\right)^2 e^{\kappa(-2p-z-z')} \\
& -\left(\varepsilon_1^2-\varepsilon_2^2\right)\left(\varepsilon_2-\varepsilon_3\right)^2 e^{\kappa(-4g+z+z')} \\
& +\left(\varepsilon_1^2-\varepsilon_2^2\right)\left(\varepsilon_2+\varepsilon_3\right)^2\left[e^{\kappa(-2p-2q-z-z')}+e^{\kappa(-2p+z-z')}+e^{\kappa(-2p-z+z')}\right] \\
& -4\left(\varepsilon_1^2-\varepsilon_2^2\right)\varepsilon_2\varepsilon_3 e^{\kappa(-2p-2q+z+z')} \\
& -4\left(\varepsilon_1+\varepsilon_2\right)^2\varepsilon_2\varepsilon_3 e^{\kappa(-2p+z+z')} \\
& +\left(\varepsilon_1-\varepsilon_2\right)^2\left(\varepsilon_2^2-\varepsilon_3^2\right) e^{\kappa(-2g-z-z')} \\
& +4\varepsilon_1\varepsilon_2\left(\varepsilon_2^2-\varepsilon_3^2\right) e^{\kappa(-2g-2p-2q-z-z')} \\
& +\left(\varepsilon_1+\varepsilon_2\right)^2\left(\varepsilon_2^2-\varepsilon_3^2\right)\left[-e^{\kappa(-2g-2q+z-z')}-e^{\kappa(-2g-2p-z+z')}+e^{\kappa(-2g-2p-2q+z+z')}\right] \\
& +\left(\varepsilon_1^2-\varepsilon_2^2\right)\left(\varepsilon_2^2-\varepsilon_3^2\right)\left[e^{\kappa(-2g-2q-z-z')}-e^{\kappa(-2g+z-z')}-e^{\kappa(-2g-z+z')}+e^{\kappa(-2g-2p+z+z')}\right],
\end{aligned} \tag{3.35}$$

and

$$\begin{aligned}
D\left(\kappa\right) = {} & \left(\varepsilon_1+\varepsilon_2\right)\left(\varepsilon_2+\varepsilon_3\right)\left(1-e^{-2\kappa(p+q)}\right) \\
& -\left(\varepsilon_1-\varepsilon_2\right)\left(\varepsilon_2+\varepsilon_3\right)\left(e^{-2\kappa p}-e^{-2\kappa q}\right) \\
& -\left(\varepsilon_1+\varepsilon_2\right)\left(\varepsilon_2-\varepsilon_3\right)\left(e^{-2\kappa(p-g)}-e^{-2\kappa(q+g)}\right) \\
& +\left(\varepsilon_1-\varepsilon_2\right)\left(\varepsilon_2-\varepsilon_3\right)\left(e^{-2\kappa g}-e^{-2\kappa(p+q-g)}\right).
\end{aligned} \tag{3.36}$$

Eq. 3.34 is only valid for a point charge in the second layer described in figure 3.9 (ie the gas gap). It doesn't hold for a point charge in the first or third layer (ie the resistive plates), the potential in these cases is described in [46]. Figure 3.11 shows an example of the potential of a charge located in two different positions in the plane $r = \phi = 0$ and figure 3.10 is a 3d plot for a charge.

Eq. 3.34 is composed of four terms, one is the source charge and two are the mirror charges. The derivation of the solution, in [46], implies the Green function associated to the boundary conditions. The mirror charges are the geometrical solutions and are located outside the volume of interest [55]. The interaction of the electric field from the mirror charges and the source charge is analogous to the effect of the boundary conditions on the source electric field. In our case this is the gas gap and so the mirror charges are placed in the anode and cathode. The first term is the potential of a simple point charge (source charge) situated at (r', ϕ', z'), the second and third terms describe the potential of the mirror charges respectively at $(r', \phi', -z')$ and $(r', \phi', 2g - z')$. The fourth term is numerically small. Its aim is to find back the correct asymptotic behaviour of the potential [46]. Figure 3.12 is a plot of the four terms.

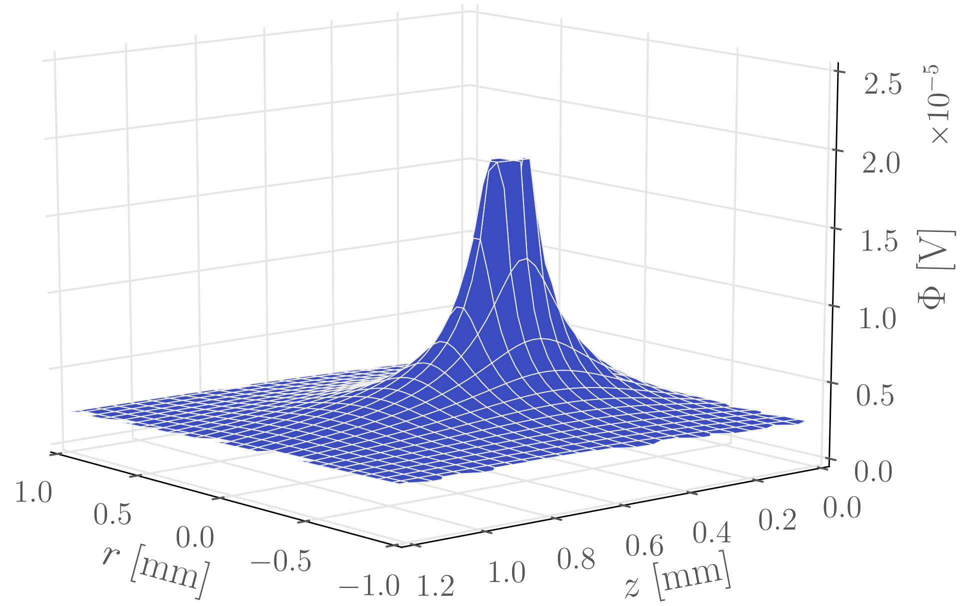

Figure 3.10: Potential of free charge at ($r' = 0$, $\phi' = 0$, $z' = 4$ mm), in the plane $\phi = 0$. With $g = 0.12$ cm, $p = 0.19$ cm, $q = 0.11$ cm, $\varepsilon_3 = \varepsilon_1 = 7$ and $\varepsilon_2 = \varepsilon_0$.

3.4.2 Electric field of a free point charge

With the potential from eq. 3.34 we can now derive the expression for the electric field

$$E_r(r,\phi,z,r',\phi',z') = -\frac{\partial \Phi}{\partial r}\left(r,\phi,z,r',\phi',z'\right), \tag{3.37a}$$

$$E_\phi(r,\phi,z,r',\phi',z') = -\frac{1}{r}\frac{\partial \Phi}{\partial \phi}\left(r,\phi,z,r',\phi',z'\right), \tag{3.37b}$$

$$E_z(r,\phi,z,r',\phi',z') = -\frac{\partial \Phi}{\partial z}\left(r,\phi,z,r',\phi',z'\right). \tag{3.37c}$$

Figure 3.14 is a 3d plot of z-component of the electric field and figure 3.13 shows the field from a free charge at different positions. From figure 3.12 one can remark that the integral term is about one order of magnitude smaller than the other terms in the potential formula (eq 3.34). When we get closer to a resistive layer, the near mirror charge term becomes important and the far one has a smaller impact. It is more visible on figure 3.15. It is apparent in the case of a free charge and both mirror charges that neglecting the correction term causes the field to deviate up to 85%, especially close to the cathode. So in order to save-up computation time one can neglect, according to figure 3.15, the correction term and the mirror charge term at $z = -z'$ [77]. In this case the field can be

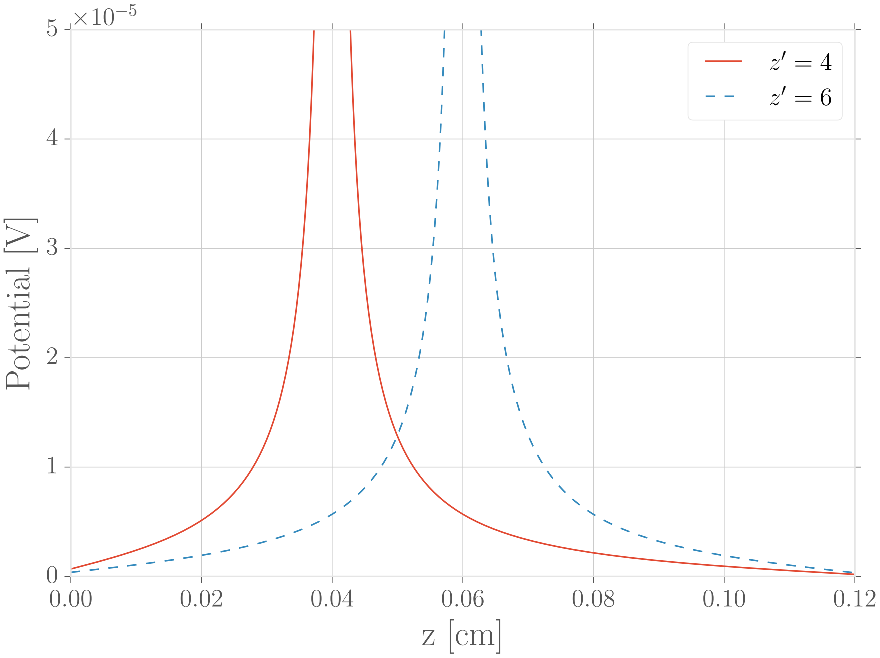

Figure 3.11: Potential of free charge at ($r' = 0$, $\phi' = 0$, $z' = 4$ mm) and ($r' = 0$, $\phi' = 0$, $z' = 6$ mm), from eq 3.34, in the plane $r = \phi = 0$. With $g = 0.12$ cm, $p = 0.19$ cm, $q = 0.11$ cm, $\varepsilon_3 = \varepsilon_1 = 7$ and $\varepsilon_2 = \varepsilon_0$.

analytically derived and we obtain

$$E_r(r,\phi,z,r',\phi',z') \approx \frac{Q}{4\pi\varepsilon_2}\left[\frac{r - r'\cos(\phi-\phi')}{(P^2+(z-z')^2)^{\frac{3}{2}}} + \left(\frac{\varepsilon_2-\varepsilon_3}{\varepsilon_2+\varepsilon_3}\right)\frac{r - r'\cos(\phi-\phi')}{(P^2+(2g-z-z')^2)^{\frac{3}{2}}}\right], \tag{3.38a}$$

$$E_\phi(r,\phi,z,r',\phi',z') \approx \frac{Q}{4\pi\varepsilon_2}\left[\frac{r'\sin(\phi-\phi')}{(P^2+(z-z')^2)^{\frac{3}{2}}} + \left(\frac{\varepsilon_2-\varepsilon_3}{\varepsilon_2+\varepsilon_3}\right)\frac{r'\sin(\phi-\phi')}{(P^2+(2g-z-z')^2)^{\frac{3}{2}}}\right], \tag{3.38b}$$

$$E_z(r,\phi,z,r',\phi',z') \approx \frac{Q}{4\pi\varepsilon_2}\left[\frac{z-z'}{(P^2+(z-z')^2)^{\frac{3}{2}}} - \left(\frac{\varepsilon_2-\varepsilon_3}{\varepsilon_2+\varepsilon_3}\right)\frac{2g-z-z'}{(P^2+(2g-z-z')^2)^{\frac{3}{2}}}\right]. \tag{3.38c}$$

3.5 Signal induction

The electrons produced in an avalanche won't be directly collected by the electrodes as they will be absorbed by the resistive anode upstream. It is only the movement of charges inside the detector that will induce a current on the read-out electrodes. In order to compute the induced charges one usually uses the Ramo's theorem [88]. This theorem gives the induced current on an electrode by a moving charge between conductors

$$i(t) = \frac{Q}{V_w}\vec{E_w}(\vec{x}(t))\,\dot{\vec{x}}(t), \tag{3.39}$$

with $\vec{E_w}(\vec{x}(t))$ being the electric field in the detector at position $\vec{x}(t)$ when the given electrode is put to the voltage V_w and the others grounded, also called the electrostatic weighting field.

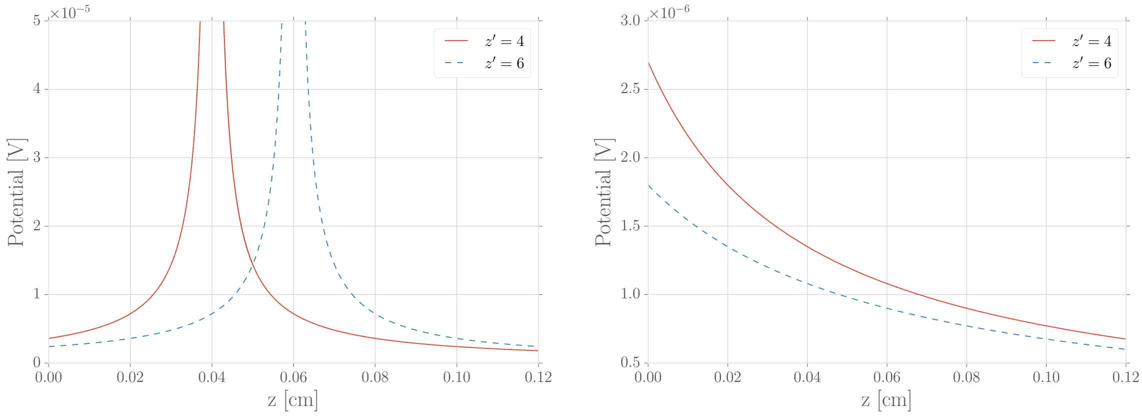

(a) Free charge term **(b)** Mirror charge term at $-z'$

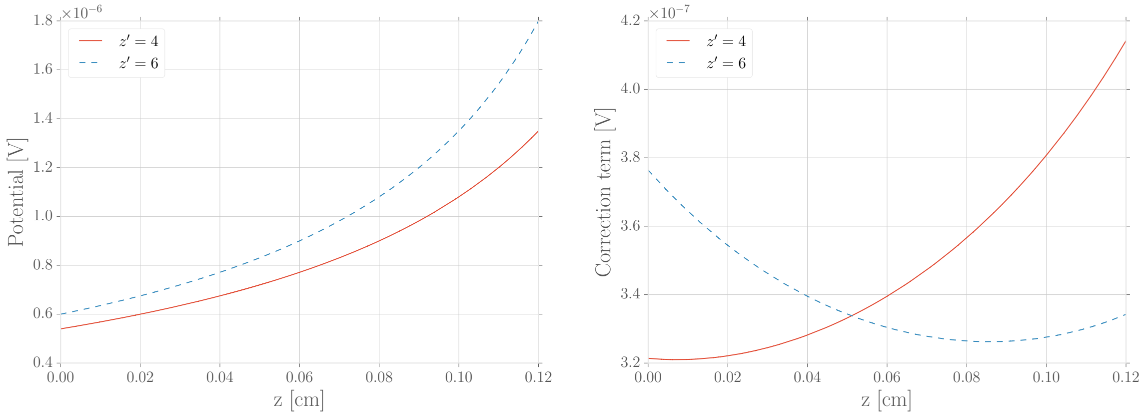

(c) Mirror charge term at $2g - z'$ **(d)** Integral term

Figure 3.12: Plot of the four terms of eq. 3.34, for a free charge located at two positions: $z' = 0.4$ and $z' = 0.6$ mm, in the plane $r = \phi = 0$. With $g = 0.12$ cm, $p = 0.19$ cm, $q = 0.11$ cm, $\varepsilon_3 = \varepsilon_1 = 7$ and $\varepsilon_2 = \varepsilon_0$. (a) The potential of a free charge. (b) The potential produced by the mirror charge at $-z'$. (c) The potential of the mirror charge at $2g - z'$. (d) The correction term.

Eq. 3.39 is valid only when we assume perfectly conducting electrodes surrounded by insulating materials, in which case electric fields are instantaneous. Considering a detector including resistive materials, such as RPCs, time-dependent fields will arise and the Ramo theorem won't be applicable any more. We use a modified version of Ramo's equation, generalised to the presence of materials with finite resistivity and conductivity [89]

$$i(t) = \frac{Q}{V_w} \int_0^t \vec{E}_w(\vec{x}(t'), t - t')\, \dot{\vec{x}}(t')\, \mathrm{d}t' \,. \tag{3.40}$$

3.5.1 Weighting field

Now one needs the corresponding expression for the detector electrostatic weighting field $\vec{E_w}(\vec{x}(t), t)$. It mainly depends on the geometry and the dielectric properties of the detector.

We consider the simple case of a single-gap geometry described by figure 3.16. A voltage V_w is applied between the electrodes, which then contain a surface charge density

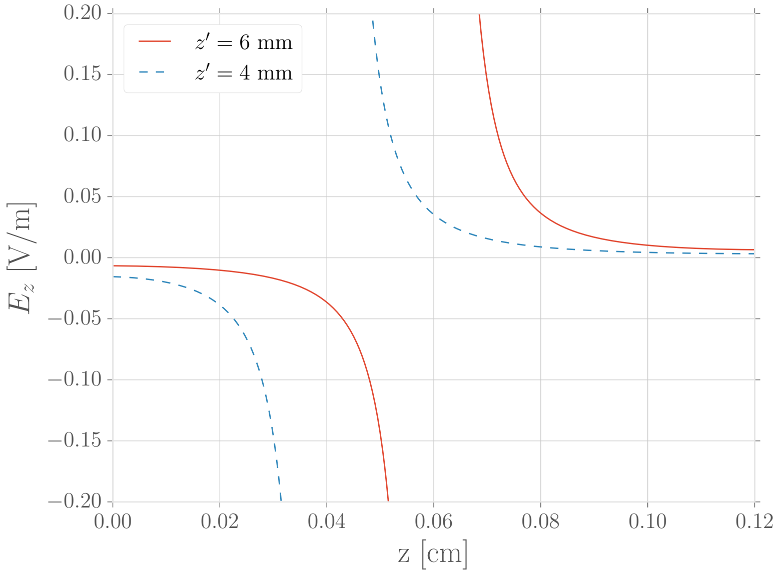

Figure 3.13: Electric field of free charge at ($r' = 0$, $\phi' = 0$, $z' = 4$ mm) and ($r' = 0$, $\phi' = 0$, $z' = 6$ mm), in the plane $r = \phi = 0$. With $g = 0.12$ cm, $p = 0.19$ cm, $q = 0.11$ cm, $\varepsilon_3 = \varepsilon_1 = 7$ and $\varepsilon_2 = \varepsilon_0$.

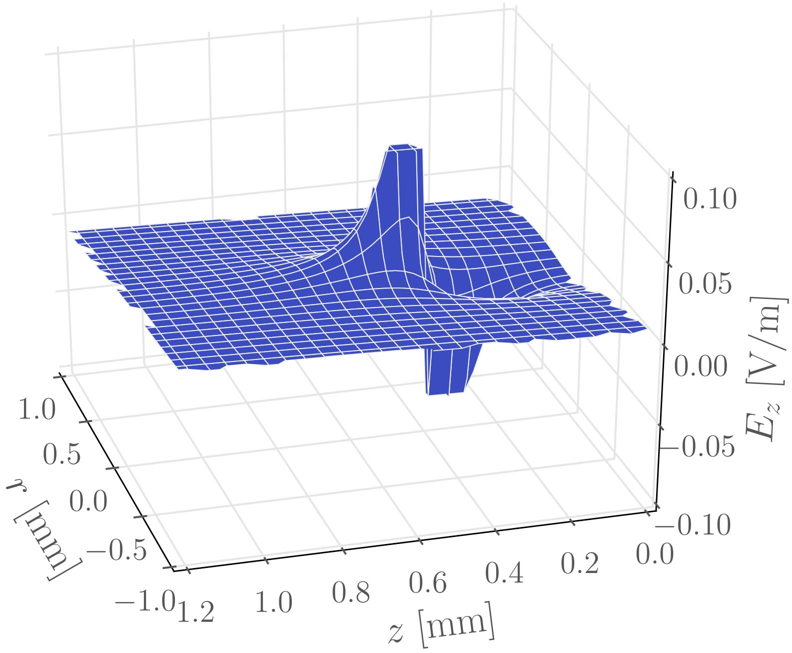

Figure 3.14: Electric field of free charge at ($r' = 0$, $\phi' = 0$, $z' = 4$ mm), in the plane $\phi = 0$. With $g = 0.12$ cm, $p = 0.19$ cm, $q = 0.11$ cm, $\varepsilon_3 = \varepsilon_1 = 7$ and $\varepsilon_2 = \varepsilon_0$.

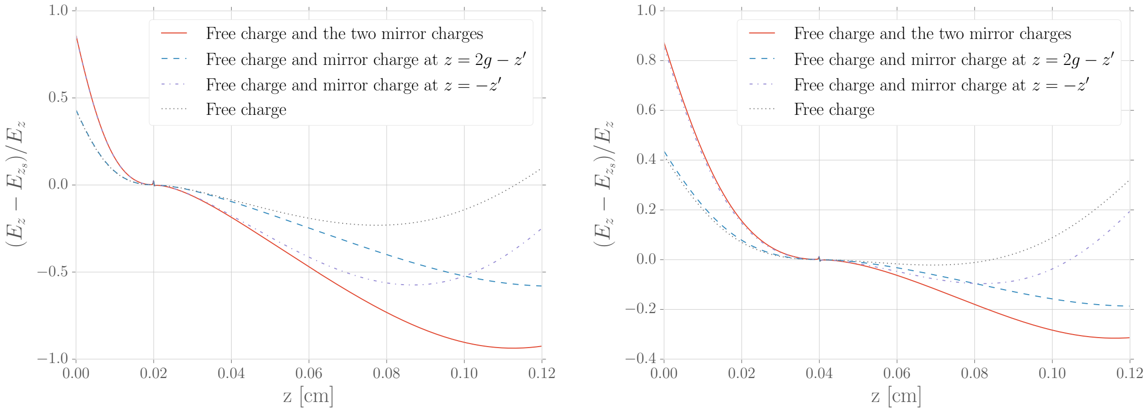

(a) $z' = 0.02$ cm **(b)** $z' = 0.04$ cm

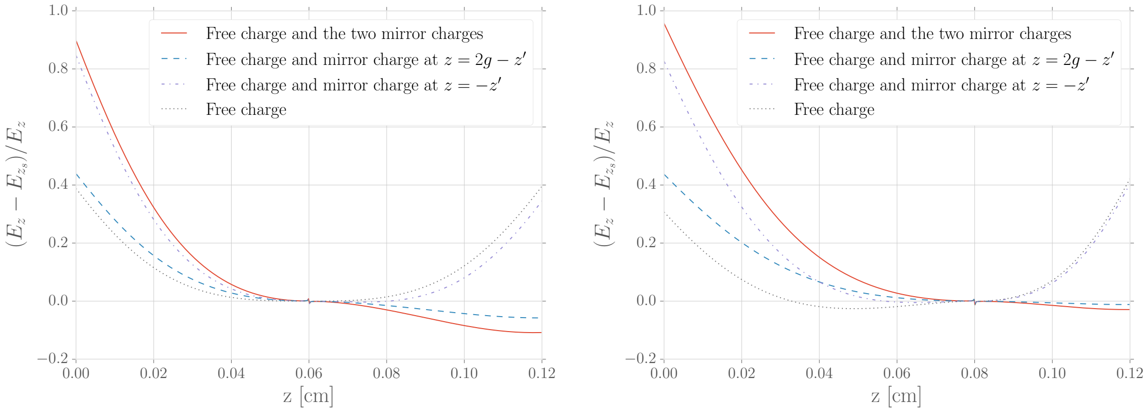

(c) $z' = 0.06$ cm **(d)** $z' = 0.08$ cm

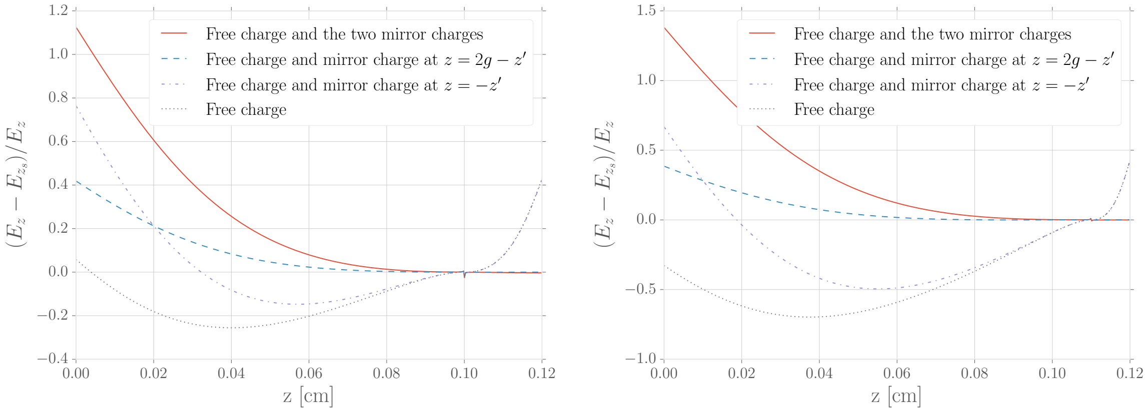

(e) $z' = 0.1$ cm **(f)** $z' = 0.11$ cm

Figure 3.15: Difference between the full expression of the electric field and a simplified form where certain terms have been omitted (the $_s$ in E_{z_s} stands for simplified), for different charge positions.

ρ. Using the Gauss theorem on three layers, labelled 1, 2 and 3 on the figure, we get the expression for electric fields

$$E_1 = \frac{\rho}{\varepsilon_1}, \quad E_2 = \frac{\rho}{\varepsilon_2}, \quad E_3 = \frac{\rho}{\varepsilon_3}. \tag{3.41}$$

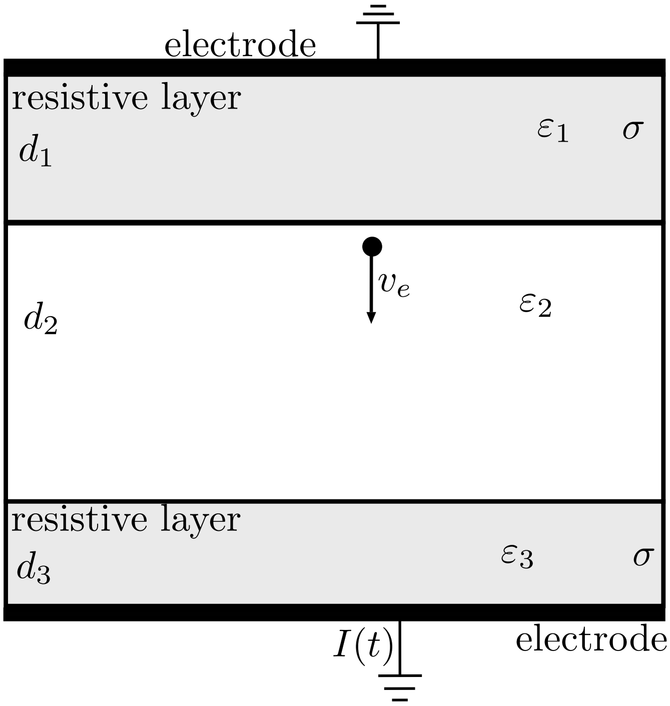

Figure 3.16: Simple single-gap geometry used to compute the weighting field. The resistive layers are d_1 and d_3 long with permittivity ε_1 and ε_3 and conductivity σ. The gas gap width is d_2 with permittivity ε_2. An electron is present in the detector, moving at velocity v_e.

The electrodes are put to voltage V_w, so we can write

$$V_w = \int_{d_1} E_1 \,\mathrm{d}r + \int_{d_2} E_2 \,\mathrm{d}r + \int_{d_3} E_3 \,\mathrm{d}r = \rho \left(\frac{d_1}{\varepsilon_1} + \frac{d_2}{\varepsilon_2} + \frac{d_3}{\varepsilon_3} \right) \tag{3.42}$$

We are interested by the weighting field, ie the field in the gas gap when the electrodes are put to voltage V_w, so $E_w = E_2$. Usually the relative dielectric constant of gases used in RPC mixtures is close to 1, so $\varepsilon_2 \approx \varepsilon_0$. From eq. 3.41 and 3.42, we have the expression for the electrostatic weighting field in the most generic case of a single-gap RPC. The time-dependant weighting field is then given by (see annexe and [89])

$$\frac{E_w}{V_w} = \frac{\varepsilon_1 \varepsilon_3}{d_1 \varepsilon_0 \varepsilon_3 + d_2 \varepsilon_1 \varepsilon_3 + d_3 \varepsilon_0 \varepsilon_1} \,\delta(t), \tag{3.43}$$

with δ is the Dirac distribution. In the case of resistive electrodes made of the same material we have $\varepsilon_1 = \varepsilon_3 = \varepsilon_0 \varepsilon_r$ with ε_r the relative dielectric constant of the electrode. Then the expression for the weighting field simplifies to

$$\frac{E_w}{V_w} = \frac{\varepsilon_r}{d_1 + d_3 + d_2 \varepsilon_r} \,\delta(t). \tag{3.44}$$

Injecting in eq. 3.40 we find the expression for the induced current

$$i(t) = Q \,\dot{\vec{x}}(t) \,\frac{\varepsilon_r}{d_1 + d_3 + d_2 \varepsilon_r}. \tag{3.45}$$

3.6 Effect of plates roughness on the electric field

The surface quality of the resistive plates has a non-negligible influence on the detector characteristics, especially the surface roughness. A plate made of Bakelite with a mat finish presents a surface roughness superior of about 6 orders of magnitude than a plate with glossy finish, which induces a swift and steady decrease in the detection efficiency [18]. Applying a thin silicone coating on mat-finished plate gives results similar to a glossy-finished plate.

Numerical simulations have been conducted by Jash et al. [56] to further investigate the effect of surface roughness. It has been found that the electric field gets heavily perturbed in the near vicinity of plates presenting a large surface roughness. It can deviate from -20% up to 60% from its regular value. Though the modelisation of the roughness has been done in a simple way, this highlights that a strong field effect may appear in the close vicinity of resistive plates, cutting-off the electron multiplication process.

3.7 Streamer formation

When the gain becomes high enough, the avalanche may evolve into a streamer or contribute to its formation with some delay [96, 61]. The streamer formation is a photonic process, as UV-photons start to contribute to the multiplication and propagation of an avalanche. A streamer can further develop into a spark discharge under some extreme conditions, such as a very high flow of charges, but those are very unlikely to happen in a RPC due to the high resistivity of the plates.

The streamer formation is a complex process but it usually involves remnants UV-photons from a precursor avalanche. Those photons may interact with the anode and cathode and generate knock-out electrons which will produce multiple avalanches that will merge into a streamer [77], see figure 3.18. Also a very high number of primaries (inducing a high rate of cluster production) could provoke a streamer formation without the need of an avalanche precursor.

The apparition of streamer is an undesired effect in RPCs in avalanche mode, as it drastically reduces the RPC rate capability. Moreover the RPC's read-out electronics and amplification circuitry are designed for avalanche currents which are much lower than of streamers.

Streamer formation is not simulated, as it would involve the modelisation of photo-ionisation processes during avalanche. In a very simple and crude way, we can consider that an avalanche evolves into a streamer if its gain exceeds $e^{20} \sim 4.85 \times 10^8$ [4, 22]. Though this a simplification, which depends on numerous parameters such as the gas mixture, it can give a rough approximation on the streamer probability during an event.

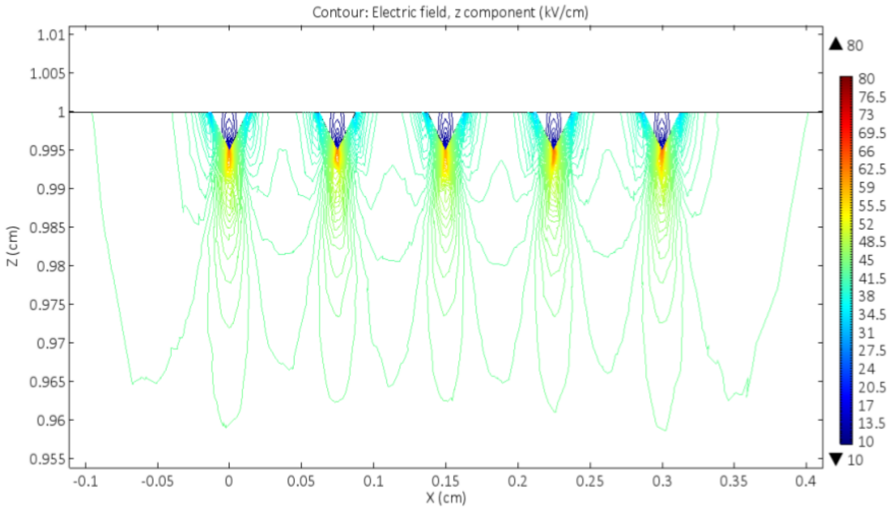

(a) Contour map of the electric field in the vicinity of a plate presenting asperities

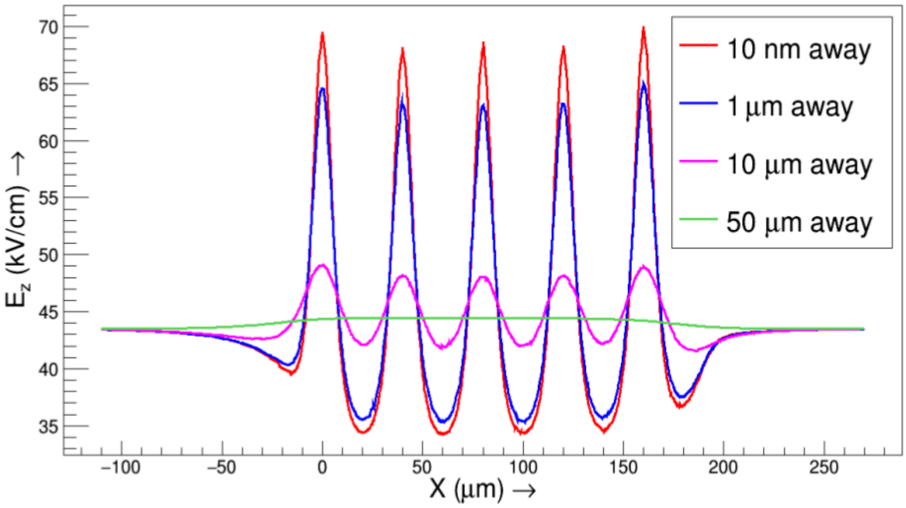

(b) Profile of the z-component of electric field along the cathode presenting asperities

Figure 3.17: Simulation of the electric field in tha gas gap of a RPC, when perturbed by the asperities present in the cathode (from [56]).

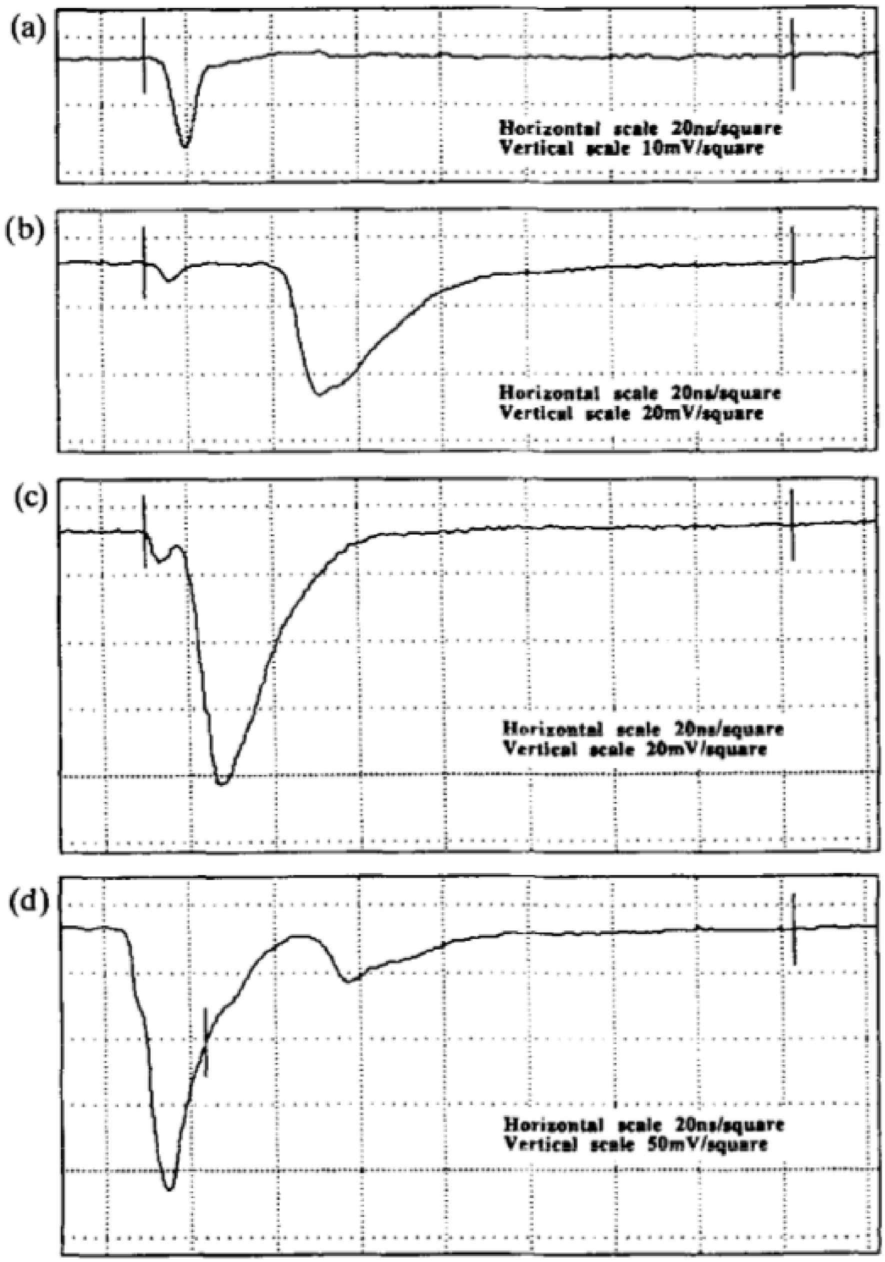

Figure 3.18: Signal from an 2 mm-wide RPC at different operating voltage, operated with $C_2H_2F_4$. (a) 9.4 kV, typical avalanche signal. (b) 9.6 kV a streamer appears after a time delay of 38 ns. (c) 10.2 kV The delay becomes shorter. (d) 11.4 kV the avalanche and streamer merged and becomes indistinguishable, also a second streamer signal is present. (From [22])

Chapter 4

Pseudo-Random number generation

The heart of any Monte-Carlo simulation lies within its random number generator. As it uses the stochastic nature of a physic phenomena; such a simulation needs a great number of random numbers, namely a sequence of independent and identically distributed variables (i.i.d.). But another key aspect of any scientific simulation is the reproducibility. In its broader sense, *scientific reproducibility* means that anyone may reproduce "*the result from a given method, possibly with different techniques and approaches*" [48]. In the case of scientific simulation one often refers to reproducibility as *repeatability*, i.e. the capacity to replicate the result given the same input data and algorithms. The repeatability is a very important aspect of any scientific simulation since it is key of validation by peer review. It is also very important when it comes to debugging.

In a naive attempt one would want to use a truly random generator for Monte-Carlo simulation, such as the `/dev/random` of UNIX systems or an external device. But by doing so, one will break away the reproducibility criteria of its simulation. Also these devices can not cope with the high output rate of random numbers needed by current simulations.

That's why the generation of random numbers is done through the use of deterministic algorithms to produce a sequence of random numbers. Such generators are called *Pseudo-Random Number Generators* (PRNGs). The task of such RNG is to produce a sequence of independent and identically distributed (i.i.d.) random variables uniformly distributed over a specific set $\mathcal{U}$, usually the unit interval $(0, 1)$ denoted $\mathcal{U}(0, 1)$. As they are generated through a deterministic algorithm, such sequences are not truly random but appear random enough to a certain point, i.e. provide good statistical properties of randomness.

There exists another category of random number generators called Quasi-Random Generator (QRNG). As PRNGs, they use a deterministic algorithm to produce random sequence whose purpose is not to look random (at least not as much as with a PRNG) but to be more evenly distributed on its interval of generation (most of the time it's $\mathcal{U}(0, 1)$). This kind of generator are mainly used for Monte-Carlo integration [83, 62] and won't be discussed in this thesis.

4.1 Definition of Pseudo-Random Number Generator

Formally a generator is a mathematical structure, defined from 5 mathematical objects $\mathcal{G} = (\mathcal{S}, s_0, \mathcal{U}, f, g)$ [62, 71],

- $\mathcal{S}$ is a finite set of *states* (as instance $\mathbb{R}, \mathbb{Z}$ are infinite mathematical sets),
- $s_0 \in \mathcal{S}$ is the initial state, also often referred as *seed*,
- $\mathcal{U}$ the set of output symbols (usually it is $\mathcal{U}(0,1)$ for Monte-Carlo applications),
- f a transition function (the function to modify the internal state of the generator),
- g the output function.

The initial state can be either deterministic or randomly generated according to a given probability distribution over $\mathcal{S}$. The state of the generator evolves as $s_n = f(s_{n-1}),\ n > 0$, and it outputs $u_n = g(s_n)$ at step n. Figure 4.1 exposes schematically the operation of a PRNG.

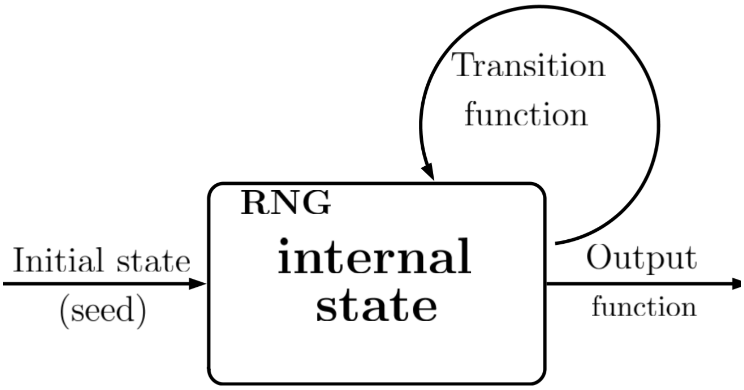

Figure 4.1: Schematic organisation of a PRNG.

Since $\mathcal{S}$ is a finite set, there exists two integers $l \geq 0$ and $0 < j < |\mathcal{S}|$ such as $s_{l+j} = s_j$ and so $u_{i+j} = u_j\ \forall\ i \geq l$. The smallest j for which this is true is called the *period* ρ of the generator. In the case of a generator whose states are represented with b bits $\rho \leq |\mathcal{S}| \leq 2^b$ [75]. In the hope of a well designed RNG typically $l = 0$ and ρ nears 2^b.

4.2 Main families of RNGs for MC simulation

Most RNGs used for simulation are expressed by linear recurrences modulo m over its set, either for $m = 2$, which means the algebra operations are in the finite field $\mathbb{F}_2$[1], or for larger value of m. In the most general form, m is a primer integer and $\mathcal{S} = \mathbb{F}_{m^k}$. In the case $k = 1$, $\mathcal{S}$ is the finite field with m elements $\in \mathbb{Z}_m = \{0, 1, 2, \cdots, m-1\}$ [62]. k is called the order of recurrence.

We take the general transition and output functions defined by $f : \mathbb{F}_{m^k} \to \mathbb{F}_m$ and $g : \mathbb{F}_m \to \mathcal{U}$. Then we define $x_n = f(s_n)$ and the output is given by $u_n = g(x_n)$. The sequence $\{x_n\}$ is called the *linear recurrence sequence.*

Typically, a generator is designed by the definition of k, m, $\mathcal{U}$ and the general output and transition functions [62]. In what follows we will briefly describe some family of generator, that include the most widely used PRNGs in Monte-Carlo simulations.

---

[1] The finite field $\mathbb{F}_m$ is the field, i.e. an algebraical structure encompassing a set $\mathbb{S}$ of numbers and algebraic operations acting on $\mathbb{S}$, of congruential operations modulo m. Two numbers a, b are congruential modulo m if $a = b \mod m$ (Gauss notation)

4.2.1 Linear Congruential Generator

A Linear Congruential Generator (LCG) is defined by the following. We set $k = 1$ and

$$x_n = a\, x_{n-1} \mod m, \tag{4.1a}$$
$$u_n = \frac{x_n}{m}. \tag{4.1b}$$

$a \in \mathbb{Z}_m^* = \{1, 2, \cdots, m-1\}$ is the set of elements of $\mathbb{F}_m$ minus the null element. Its period is $\rho = m - 1$.

This kind of generator has been widely used over the past 30 years. The `rand()` function of the UNIX's glibc is an LCG with $m = 2^{31}$, yielding a period of $2^{31} - 1 \sim 2,14 \times 10^9$. It is now considered obsolete and should not be used in Monte Carlo simulation because of its small period and inner structure (see section 4.4.1) [68, 50]. On modern CPU, the range of this RNG can be exhausted in a matter of minutes (even seconds on fastest CPUs).

4.2.2 Multiple Recursive Generator

The Multiple Recursive Generator (MRG) family is defined in its matrix form as

$$\mathbf{X}_n = \mathbf{A}\, \mathbf{X}_{n-1} \mod m. \tag{4.2}$$

The $k \times k$ matrix $\mathbf{A}$, of elements $a_i \in \mathbb{Z}_m$, defines simple operations on blocks of bits such as AND, OR, exclusive-OR ... With $\mathbf{X}_n = (x_{n,0}, \cdots, x_{n,k-1})^{\mathrm{T}}$.

The matrix $\mathbf{A}$ is defined so that we can rewrite eq. 4.2 in a more classic form [75, 69]

$$x_n = (a_1\, x_{n-1} + \cdots + a_k x_{n-k}) \mod m, \tag{4.3a}$$
$$u_n = \frac{x_n}{m}. \tag{4.3b}$$

The state of the generator is defined by the vector $s_n = (x_n, \cdots, x_{n+k-1}) \in \mathbb{Z}_m^k$. This generator has a period of $\rho = m^k - 1$. When we take $k = 1$ we find back the LCG generator.

The `MRG32k3a` [72, 67] is an example of MRG generator. It is in fact a combination of two small MRGs of order of recurrence $k = 3$, with $m_1 = 2^{32} - 209$ and $m_2 = 2^{32} - 22853$. Because m is not prime, the generator doesn't reach the maximal period, which would be $\rho = (m_1^k - 1)(m_2^k - 1)$, but is $\rho = (m_1^k - 1)(m_2^k - 1)/2 \approx 2^{191}$. This combination technique allows the design of fast RNGs with small states (low impact on memory consumption) and a period reasonably enough for most simulation cases.

4.2.3 Linear Feedback Shift Register Generator

A Linear Feedback Shift Register Generator (LFSR) is a special case of eq. 4.2 with $m = 2$ and an output function of the form

$$u_n = \sum_{j=1}^{L} x_{ns+j-1}\, 2^{-j}. \tag{4.4}$$

The state of the generator $s_n = (\mathbf{X}_n, \cdots, \mathbf{X}_{n+k-1})$ is a $(L \times k)$-dimensional vector. The integer $s > 0$ is called the shift length and $L \leq k$ is an integer. In practice L is the size of a machine-word ($L = 32$ or $L = 64$ typically) so that each X_n occupies the memory of a machine-word to improve efficiency.

One particular sub-family of this kind of generator is the Twisted Linear Feedback Shift Register [80], which reaches the maximum period possible of $\rho = 2^{kL} - 1$. Its most famous and used implementation is the so-called Mersenne-Twister [82] `MT19937` which has a period of $2^{19937} - 1$.

4.3 Jump-ahead and sequence splitting

From the matrix form formulation of an MRG (eq. 4.2), one can compute the state $\mathbf{X}_{n+\nu}$ from $\mathbf{X}_n$ for any integer $\nu > 0$ with

$$\mathbf{X}_{n+\nu} = (\mathbf{A}^{\nu} \mod m)\, \mathbf{X}_n \mod m, \tag{4.5}$$

where the matrix $(\mathbf{A}^{\nu} \mod m)$ can be precomputed. This method is called *jump-ahead* and is very handy in the process of splitting a random sequence in many streams and substreams [74, 75].

To split a cycle in several streams and substreams, we choose two positive integers v and w and we define $z = v + w$. The cycle is first divided into adjacent *streams* of length $Z = 2^z$. Then each stream is cut into $V = 2^v$ *substreams* of length $W = 2^w$. In order to advance (jump-ahead) to the state at the beginning of next streams or substreams, the matrix $(\mathbf{A}^{\nu} \mod m)$ needs to be computed only once for $\nu = Z$ and $\nu = W$.

The `RngStreams` package [74] implements the generator `MRG32k3a` with sequence splitting and jump-ahead. It is capable of producing 2^{64} streams that are divided into $V = 2^{51}$ substreams of length $W = 2^{76}$ for a stream length of $Z = 2^{127}$. It is a generator perfectly adapted for simulation in parallel environment. Figure 4.2 exposes a schematic view of the sequence splitting implemented in `RngStreams`.

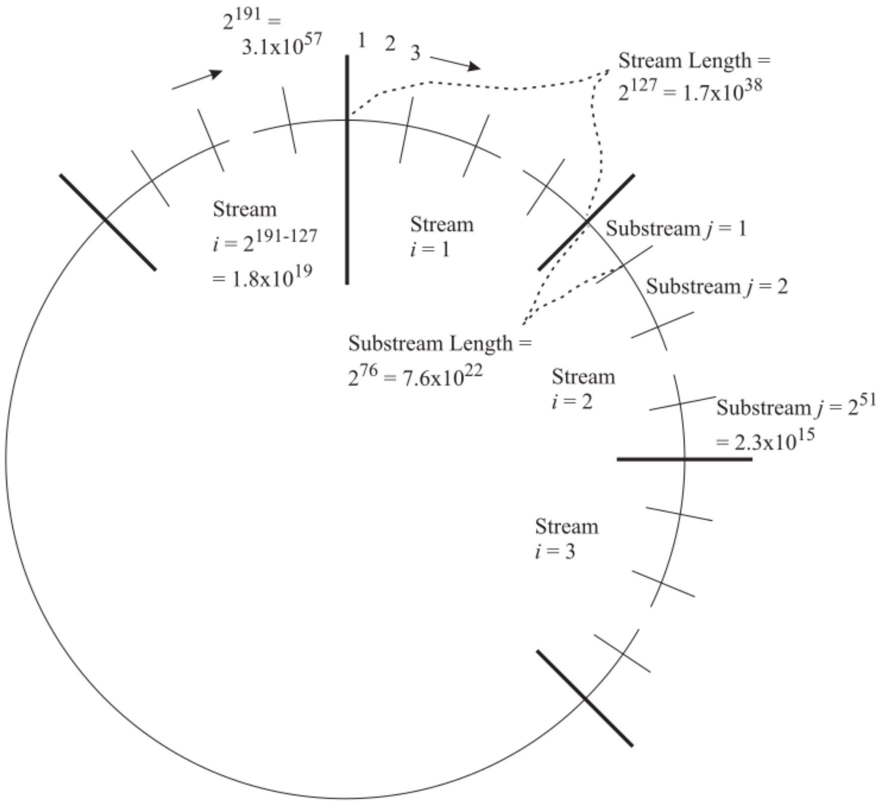

Figure 4.2: Schematic view of the internal organisation of `RngStreams`. (from [74])

4.4 Quality criteria of PRNGs

There is a wide number of generators available out there. Some of them are bad, some are good, other unadapted for specific cases ... In general, a generator should satisfy a certain number of criteria to be considered in a Monte-Carlo simulation [62, 44]

Period length A generator has to provide a period sufficiently large so that it is not exhausted by any simulation system. A simulation should only consume a small fraction of the generator period. Nowadays one can directly ban the classical LCG as it provides only some several billions of numbers.

Uniformity and unpredictability A generator should output a sequence that behaves like a realisation of i.i.d over the set $\mathcal{U}$. Hence a sequence should be uniformly distributed over $\mathcal{U}$ and unpredictable (one could not guess u_{n+1} from $(u_0, \cdots, u_n)$). But since the sequence is deterministic and periodic, we know in advance it is not truly random and there will always be a statistical test to fail the generator (in more or less time).

But in Monte-Carlo simulation, the requirements for a generator are not as high and important as in cryptography for instance. In general we ask that generators pass a battery of statistical tests, adapted to the application, so that we can consider that the sequence it yields looks enough like an i.i.d.

Efficiency A generator should yield random numbers at a high output rate; typically a simulation needs several billions, of random numbers. A generator should be able to output such a large quantity of random numbers in an acceptable small time, with an impact on the simulation performance as small as possible.

Repeatability and portability A generator should always output the same sequence given a specific initial state. It is an important criteria for scientific simulations, for error checking and resolution. Also a generator implementation should not depend on specific machine architecture. In other words, a generator should give the same numbers no matter the hardware on which it is executed.

4.4.1 Lattice structure and figures of merit

Any generator has its inner structure, more or less *hidden*. As we have described only generators with linear algorithms, those present a linear inner structure. The structures begin to appear for very large sample, in the order of magnitude of the generator's period. Figure 4.3 show the successive outputs of a LCG generator, where each tuple (u_{2n}, u_{2n+1}) represents a point. For $n = 100$, points look randomly distributed. For $n = 500$ regularities begin to arise and become clearly visible for $n = 1000$. For $n = 5000$ we can see a linear lattice structure, where each point lie in parallel hyper-planes. Figure 4.4 exhibits the same behaviour but in a 3-dimensional cube, each point represents the tuple $(u_{3n}, u_{3n+1}, u_{3n+2})$. We used a LCG with the parameters $a = 1103515245$ and $m = 2^{21}$. Since m is not prime, the period of this generator cannot reach its maximum value of $\rho = m - 1$ [62]. We poorly set the parameters on purpose to highlight the inner structure in small CPU-time.

More generally, for a given dimension $d > 0$ we define the vector $\mathbf{v}_{0,d} = (u_0, ..., u_{d-1})$. If the initial state s_0 has been set randomly over $\mathcal{S}$, then the vector $\mathbf{v}_{0,d}$ should be approximately uniformly distributed over the unit hyper-cube $(0, 1)^d$. We define the set Ψ_d composed of the d-dimensional vectors: $\Psi_d = \{\mathbf{v}_{0,d} = (u_0, ..., u_{d-1})\}$. The purpose of a PRNG is to output values u_i that mimic an i.i.d behaviour (namely to be uniformly distributed and independent). Since a generator has only a finite set of states, the vector

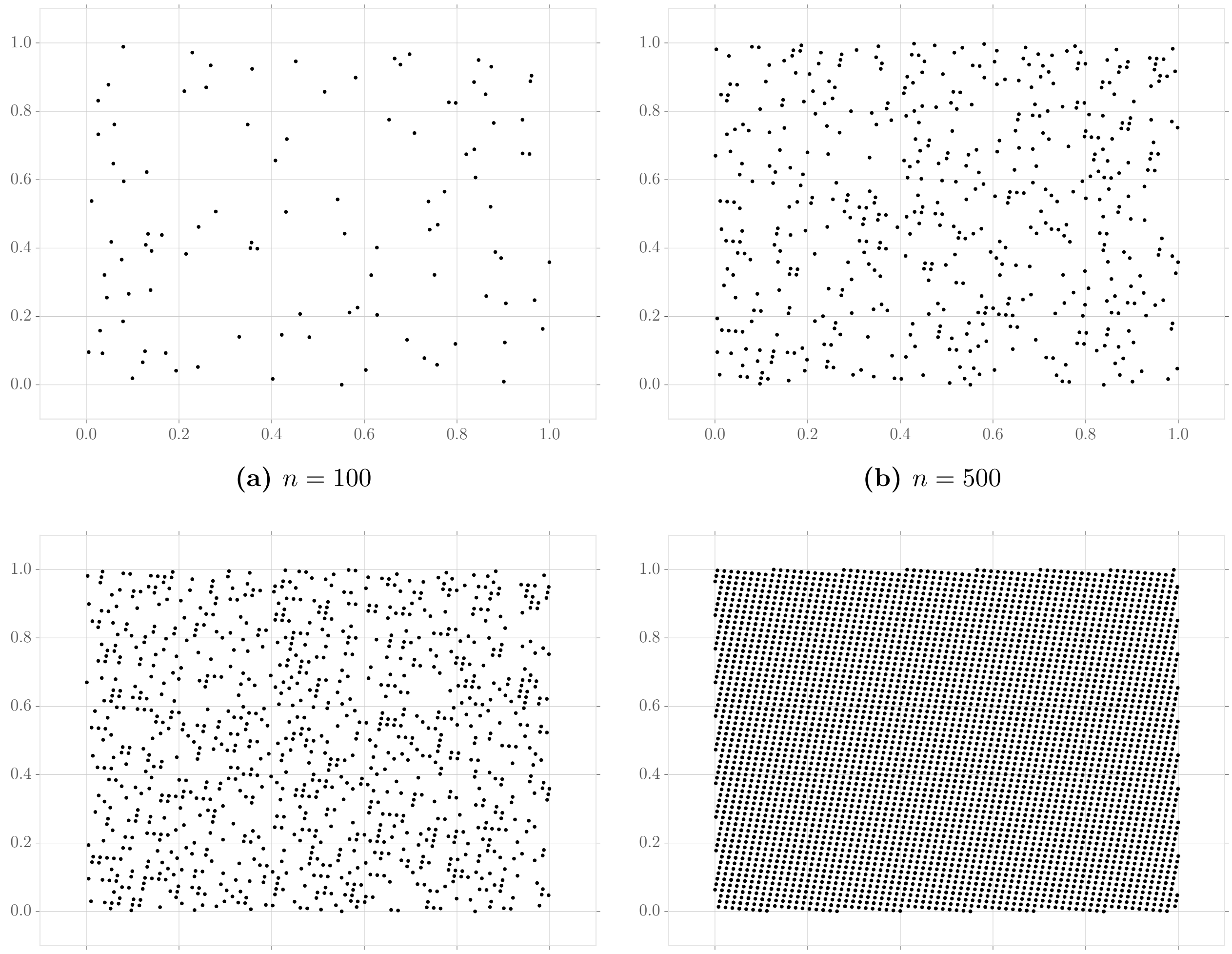

(a) $n = 100$ **(b)** $n = 500$

(c) $n = 1000$ **(d)** $n = 5000$

Figure 4.3: Successive outputs of a LCG generator, where each point represents the tuple (u_{2n}, u_{2n+1}), for different number of points.

$\mathbf{v}_{0,d}$ can only be uniformly distributed over the set Ψ_d. So we want Ψ_d to cover as much as and the most evenly possible the unit hyper-cube $(0,1)^d$. A larger Ψ_d should cover it more evenly, but this also means a larger $\mathcal{S}$ and so a greater memory consumption and overhead to compute the output sequence. This is a major drawback for parallel environment with many streams and/or substreams. It is also important to note that a bigger set of states does not necessarily make a generator a good one [68].

We have seen earlier that linear RNGs exhibit a lattice structure where the output vectors lie in parallel hyper-planes (see figures 4.3 and 4.4). We call the distance between the hyper-planes d_d, and a smaller d_d means that Ψ_d is more uniformly distributed over the hyper-cube. Measuring this distance is called the *spectral test* [70]. It is a figure of merit to assess the quality of a generator by studying its mathematical structure.

There exists other figures of merit used to evaluate theoretically the quality of a generator, such as the *discrepancy*, but we won't detail them in this thesis.

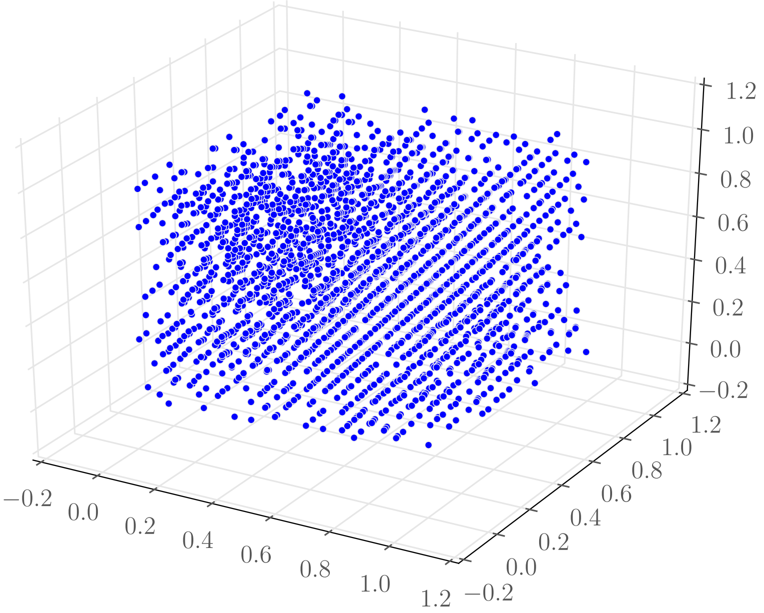

Figure 4.4: Successive outputs of a LCG generator on 3-dimensions, where each point is the tuple $(u_{3n}, u_{3n+1}, u_{3n+2})$, for 2500 points.

4.4.2 Statistical testing

After a generator has been designed and its structure analysed, one can evaluate how it performs through statistical tests. We consider the RNG as a black-box and we test it against the null-hypothesis $\mathcal{H}_0$ that "*the output of the generator is a realisation of a sequence of i.i.d random variable over the set* $\mathcal{U}(0,1)$". Basically one knows this is a wrong assumption, as the sequence from a generator is deterministic and periodic, but we want to know to which extent this is false.

The fact that a generator passes those tests doesn't mean anything but only that those tests failed to measure a noticeable deviation from an i.i.d sequence in a reasonable amount of time. Even if no statistical tests can prove that a generator is foolproof, they can improve our *confidence* in it.

There exists a wide variety of available tests. The `TestU01` software [73] offers the most extensive collection of statistical tests currently available for RNGs. It presents three famous batteries of tests called *smallCrush*, *Crush* and *BigCrush*. A generator that passes those are referred as *Crush-resistant*. This is an efficient way to determine if a RNG is suited for a particular Monte-Carlo simulation. However a generator deemed as not Crush-resistant is not necessarily inappropriate. For instance, the Mersenne-Twister `MT19973` fails some Crush tests but is still perfectly safe for most simulation cases. It is implemented as the default RNG in the `ROOT` framework [19], commonly used in High Energy Physics.

4.5 PRNG in parallel environment

Nowadays parallel systems are widely available and used, with multi-core and many-core CPU architecture and GP-GPUs (General-Purpose Graphics Processing Units). They present an increasing number of *processing elements* (PEs) that can operate in parallel.

With this new programming paradigm for Monte-Carlo simulations, arise new problematics for the implementation and use of RNGs [58]:

- a generator should produce sequences for any number of PEs ,
- each parallel sequence should be independent and without correlation,
- there should be no cross-talk between RNG assigned to PEs.

There are many techniques to produce parallel stochastic streams from a given PRNG, either from an unique sequence to be divided into substreams or by feeding carefully chosen parameters to a generator to produce multiple independent sequences.

Central server - This approach consists in using a central server on which an unique generator is running and provides on-demand pseudo-random numbers to the PEs. This is maybe the easiest way to provide random numbers to parallel workers but it has major drawbacks. The results of a simulation won't be reproducible using this technique because of scheduling policies (the random numbers won't be distributed to the same PEs from a run to another). Furthermore a bottleneck may appear if too many PEs need to be fed. In the end, this approach is not recommended for parallel Monte-Carlo simulations [50].

Sequence splitting - This method consists in partitioning the sequence of a generator into several non-overlapping and contiguous blocks of equal size. From a stochastic sequence $\{u_i\}$ we'll get the j-th subsequence of length m $\{u_{k+(j-1)m}\}$ with $k = 0, \cdots, m-1$. The parameters of the sequence has to be carefully chosen in order to create long-enough substreams for the considered simulation, but also to avoid correlations between substreams [34, 50].

Jump-ahead algorithms are an important part for any generator implementing sequence splitting, in order to advance the state at the beginning of the next substream. Section 4.3 describes the basics of jump-ahead and figure 4.2 shows schematically the sequence splitting parametrised in `RngStreams`.

Random spacing - This method builds n streams from an unique generator by initialising it with n random initial states. The random states are usually generated through another generator. There is a risk of streams overlapping coming from bad initialisation because of two random states being too close to each other. The overlapping probability for n streams of length L with a generator of period P is $n(n-1)L/P$ [50].

If we consider $n = 100$ PEs running in parallel a simulation consuming $L = 10^{12}$ random numbers, $n(n-1)L \approx 10^{16}$. So for the overlapping probability to become negligible, we need a generator with a period far greater than $P = 10^{16} \sim 2^{53}$. For this reason it is not recommended to use any LCGs generator, whose period is usually of the order of 2^{60}, with random spacing for parallel Monte-Carlo simulation.

Leapfrog - This method builds up a random stream from an initial sequence by distributing random numbers in turn to each PEs, in the same manner as cards are dealt to players. Each PE has an unique identifier i, and they'll build their own stream Y_i from the generator's sequence X where $\{Y_i = X_i, X_{i+N}, \cdots, X_{i+kN}\}$ with N being the numbers of PEs. For a generator's period P, the length of each allocated stream will be P/N.

This method has to be used with care. As in sequence-splitting, correlations may arise between streams and the leap interval (ie the numbers of PEs) has an influence on the randomness quality [44, 50].

One should give extra care to parametrisation of the number of PEs. If the number of workers is changed, from one run to another the random numbers won't be allocated to the same PE, thus breaking away the repeatability.

Parametrisation - With this method, one doesn't create several streams from an original sequence. Instead one builds as many instances of a given PRNG but with different parametrisation. Each instance shares the same generator (ie the same mathematical structure and generation mechanism) but an unique parameter set is embedded into its internal structure. Thus one will get as many independent PRNGs as needed.

The Dynamic Creator (`DC`) of the Mersenne-Twister family [81] uses this method to build parametrised generators, from a given unique identifier. The created generators are said to be highly independent although no mathematical proof can establish this [50].

This method, and particularly the `DC` algorithm, is an efficient way to produce parallel stochastic streams without breaking away the repeatability.

Chapter 5

Monte-Carlo simulation of electronic avalanches in RPC

Nowadays Monte-Carlo simulation has become an essential tool to understand and study the behaviour of a detector. When designing a specific detector in High Energy Physics, a detailed and precise modelisation of the physics processes is an important tool to optimise the detector parameters, such as gas mixture, electric field intensity, plates material and so on in the case of RPCs.

In this chapter we will detail the Monte-Carlo simulation of electronic avalanches in RPCs, from the description and modelisation of the main physical processes detailed in chapter 3. The propagation of the electrons is simulated in one dimension along the z-axis (as defined in figure 3.9), which is divided into several steps. The contribution of the space charge to the z-component of the electric field is dynamically computed at each step. The values of the gas parameters (Townsend and attachments coefficients, ...) are re-evaluated at each position and time-step. We refer to this model as 1.5D because the propagation of the avalanche is in one dimension and we assume that at each position the electrons are contained in a radial distribution depending on the transverse diffusion coefficient.

It is a `C++` simulation, exploiting some features of the `C++11` standard, with multi-thread support. It needs some input parameters computed by `MAGBOLTZ` and `HEED` software [98, 16], both being interfaced in the `Garfield++` framework [38]. Apart from this, the simulation doesn't need any other 3rd party library. It was designed in the hope to be fast and easily portable, so that anyone wishing to use and modify it could do so without too much difficulties. It is available at a public repository [36].

5.1 Implementation of the model

To simulate the development of an avalanche in an RPC we first need the amount of ionisation deposited in the gas by the passage of a charged particle, i.e. the position and number of electrons liberated. We use the `HEED` simulation program that yields the number and position of ionisation cluster produced by the passage of a charged particle in a gaseous mixture (see figures 3.1 and 3.2 of section 3.2).

From the amount of primary ionisation we can now proceed to the avalanche propagation computation, which is characterised by the probability distributions from eqs. 3.17 3.19 and 3.21 depending on the value of α and η. It is simulated by drawing a random number from eqs. 3.23 3.24 and 3.25. To give an example of the procedure, let's consider that the gas gap is divided into N steps of δz and assuming n_0 electrons at position $z = 0$. Each of the n_0 electrons have a probability to multiply, which is modelised by drawing a random number from eq. 3.23 3.24 or 3.25 for each one of them. In the end we will have n_1 electrons at the position $z = \delta z$. Then those n_1 electrons will multiply in the exact same manner, and we'll have n_2 electrons at the position $z = 2\delta z$. This procedure is iterated until all the electrons have reach the anode.

However this procedure is very slow when the number of electrons to multiply becomes important, because of heavy CPU-time functions (principally in eq. 3.23). In this case we can make use of the Central Limit Theorem, which dictates that the summation of a large number n of independent and identically distributed random variables from a probability distribution of mean μ and variance σ converges to a normal distribution defined with

$$\mu_{CLT} = n\,\mu, \quad \sigma_{CLT} = \sqrt{n}\,\sigma, \quad n \gg 1. \tag{5.1}$$

In our case n is the number of electrons at position z, $\mu = \bar{n}(z)$ and σ is from eqs. 3.18, 3.20 or 3.22. Figure 5.1 exhibits the difference in the number of electrons given by the full procedure and with the central limit theorem. From about $n = 10^4$ the difference becomes negligible. In the simulation, we switch to the central limit theorem when the number of electrons exceeds $n = 1.5 \times 10^4$. With this method the multiplication procedure is quite fast.

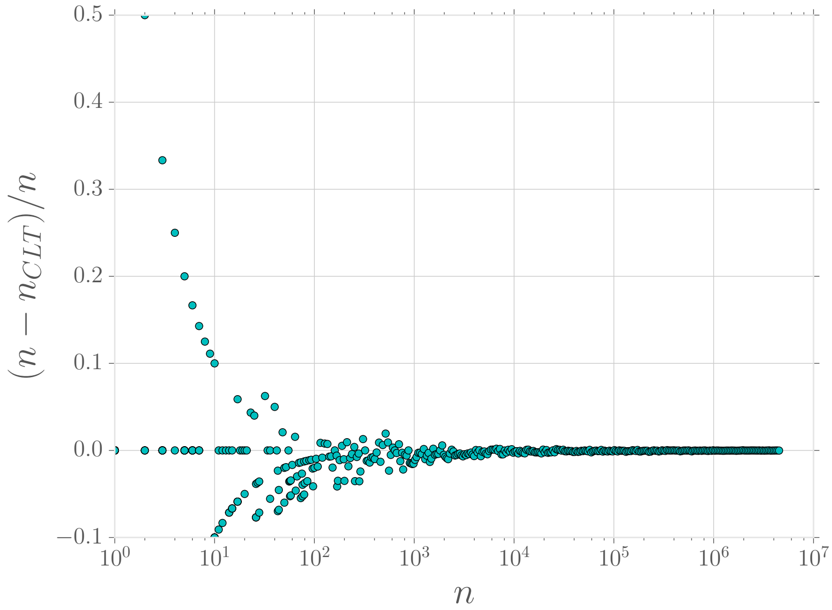

Figure 5.1: Difference in the number of electrons produced by the full procedure, described in section 5.1, and the central limit theorem.

Figure 5.2 shows the evolution of three different avalanches started by a single electron at $z = 0$, the average number of electrons $\bar{n}$ (eq. 3.4) is also plotted. Large fluctuations appear during the first step of an avalanche, that greatly influence its evolution. Very quickly the avalanches behave like a growing exponential, just like the expression for the average number of electrons.

The simulation is organised as follow.

1. The gas gap, of width g, is divided into a fixed number of steps $\delta z = g/N$. This corresponds to time steps of $\delta t = \delta z / v_0$, with $v_0 = v_D(E_0)$ which is the drift velocity at the initial electric field E_0.
2. Primary ionisation by a charged particle with momentum p is computed with `HEED`.

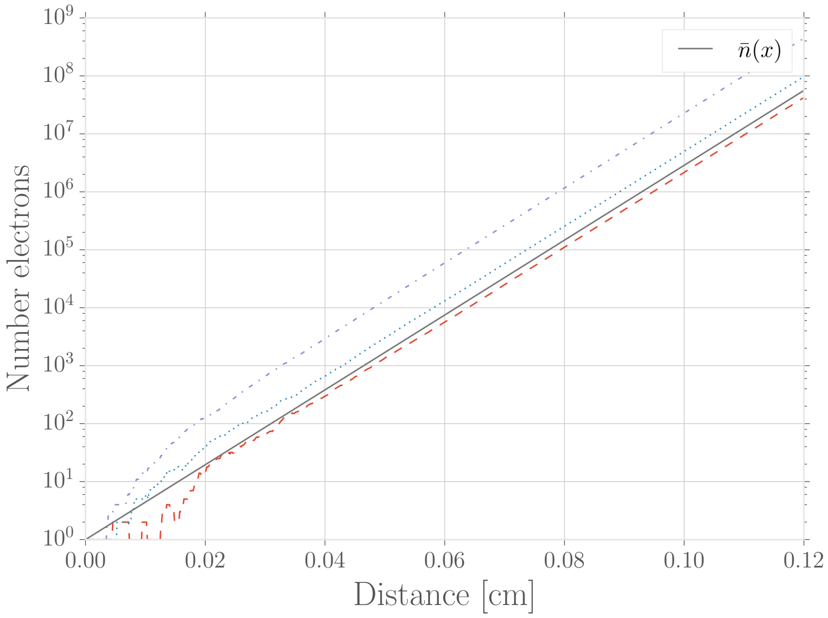

Figure 5.2: Simulation of three different avalanches, started by a single electron at $x = 0$, over a gas gap of 0.12 cm with $\alpha = 190\,\text{cm}^{-1}$ and $\eta = 64\,\text{cm}^{-1}$. The analytic formulation of the average number of electron $\bar{n}(x)$ is also plotted.

3. From the values returned by `HEED`, primary clusters are distributed into their respective bins and populated by their number of electrons
4. The space charge field $E_{SC}(z)$ is evaluated, using the transverse diffusion coefficient to approximate the radial distribution, and the electric field is dynamically computed with $E(z) = E_0 + E_{SC}(z)$, E_0 being the applied electric field (see section 5.3).
5. The transport parameters, the Townsend and attachment coefficients $\alpha(E(z))$ and $\eta(E(z))$, the drift velocity $v_D(E(z))$ and the diffusion coefficients $D_{L,T}(E(z))$ are computed at each detector step.
6. The electrons multiply according to eqs 3.23 3.24 3.25, depending on the value of $\alpha(z)$ and $\eta(z)$, and propagated to the next bin.
7. The longitudinal diffusion is computed (see section 5.2)
8. The current and charges induced on the anode by the movement of the electrons are computed using eqs 3.44 and 3.45 (see section 5.5).
9. Steps 4 to 8 are repeated until all the electrons have reached the anode or have been attached.

In the next sections we will detail some of the processes involved during the computation of an avalanche.

5.2 Diffusion

In section 3.3.2 we talked about the anisotropic diffusion undergone by an electron cloud in a gas under the influence of an electric field. It is due to collisions with gas molecules and can be described by two distinct expressions, one for the longitudinal diffusion and the other for the transverse one.

5.2.1 Longitudinal diffusion

If an electron cluster drifts from the position z to $z + \delta z$, each electron has a probability to drift to another position different from $z + \delta z$. The diffusion is assumed to be gaussian and the probability distribution is given by eq. 3.31a

$$\varphi_L(z, \delta z) = \frac{1}{\sqrt{2\pi\,\delta z}\,D_L} \exp\left(-\frac{z^2}{2D_L^2\,\delta z}\right). \tag{5.2}$$

To compute the new z-coordinate of an electron drifting from z to $z + \delta z$, meaning that it has drifted a total distance $l = \delta z$, we draw a random number from a gaussian defined with $(z_0 = 0)$

$$\mu = z + \delta z\,, \quad \sigma_L = D_L\sqrt{\delta z}\,. \tag{5.3}$$

Since each electron has a probability to be diffused forward and backward, the growth of the avalanche is influenced. An electron that has been diffused backward will drift on a greater distance and will multiply further. On the contrary, an electron diffused forward will drift on a smaller distance and won't multiply as much. Figure 5.3 shows the same

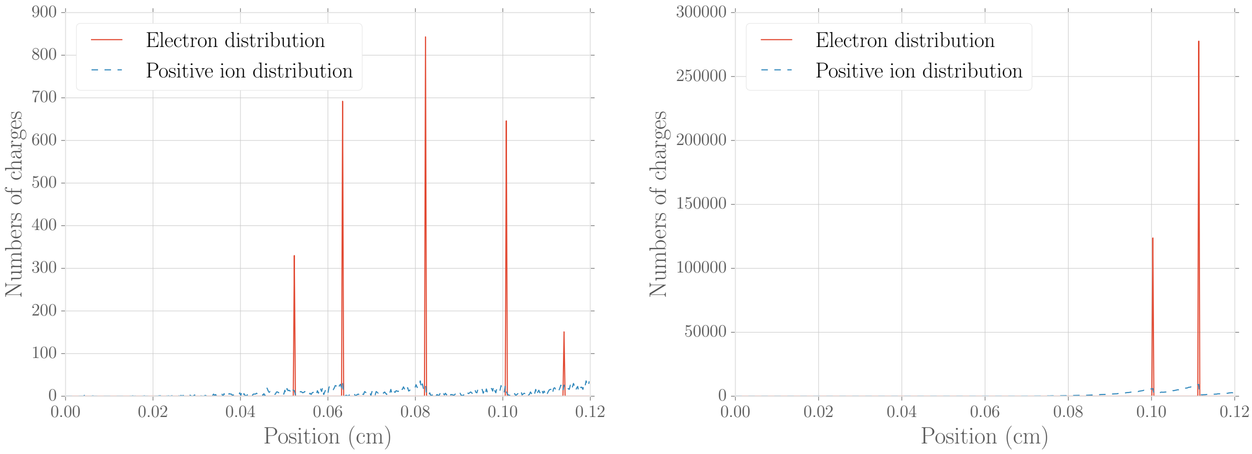

(a) $n_e = 2662$ **(b)** $n_e = 4.01 \times 10^5$

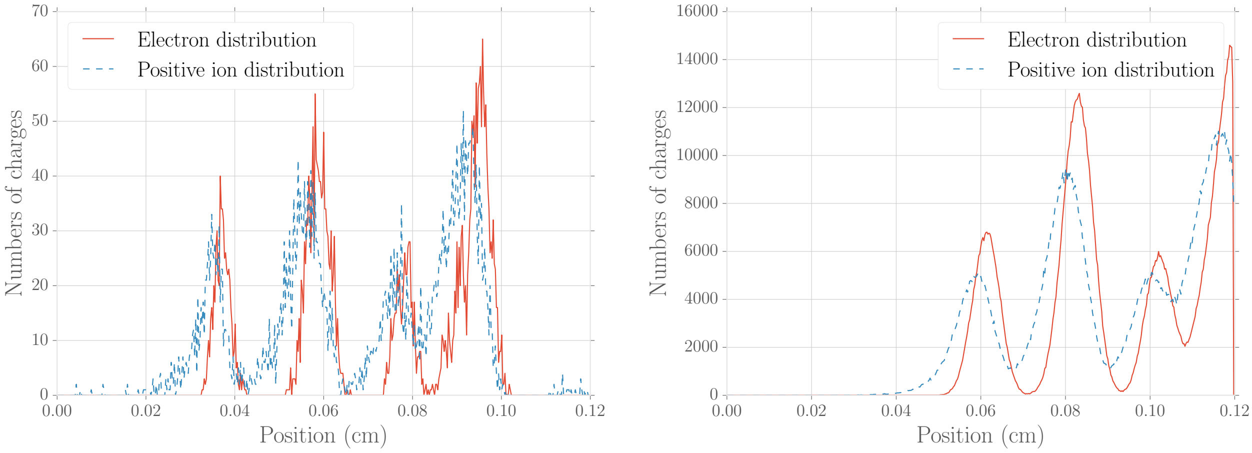

(c) $n_e = 3828$ **(d)** $n_e = 1.25 \times 10^6$

Figure 5.3: Charge distribution of an avalanche at $t = 3.95\,\text{ns}$ and $t = 7.90\,\text{ns}$. On (c) and (d) the longitudinal diffusion is computed. On (a) and (b) it is switched off.

avalanche at two different times with and without longitudinal diffusion. We can see the impact of such diffusion on the development of the avalanche. It is clearly visible between figures 5.3a and 5.3c, they exhibit the influence of the backward diffusion that makes the avalanche to grow for a much longer time. On figure 5.3a the farthest cluster is almost at the anode whereas on figure 5.3c the farthest cluster extends to about 0.10 cm.

In a more general manner, following the arguments proposed in [77], we consider two avalanches that travel the distances $z + \delta z$ and $z - \delta z$. From eq. 3.4, on average, these avalanches will produce $n(z, \delta z) = e^{\alpha(z+\delta z)} + e^{\alpha(z-\delta z)}$ electrons. Then we consider two avalanches that travel the distance z, on average they will produce $n(z) = e^{\alpha z} + e^{\alpha z} = 2e^{\alpha z}$. We compare both expressions

$$\frac{n(z, \delta z)}{n(z)} = \frac{e^{\alpha(z+\delta z)} + e^{\alpha(z-\delta z)}}{2e^{\alpha z}} = \cosh(\alpha\, \delta z). \tag{5.4}$$

Figure 5.4 shows a plot for the cosh function with $\alpha = 1$. For any α, $\delta z > 0$, which is always the case during a Townsend avalanche when we consider longitudinal diffusion, we have $\frac{n(z,\delta z)}{n(z)} > 1$. So in the end the longitudinal diffusion increases the production of electron during an avalanche.

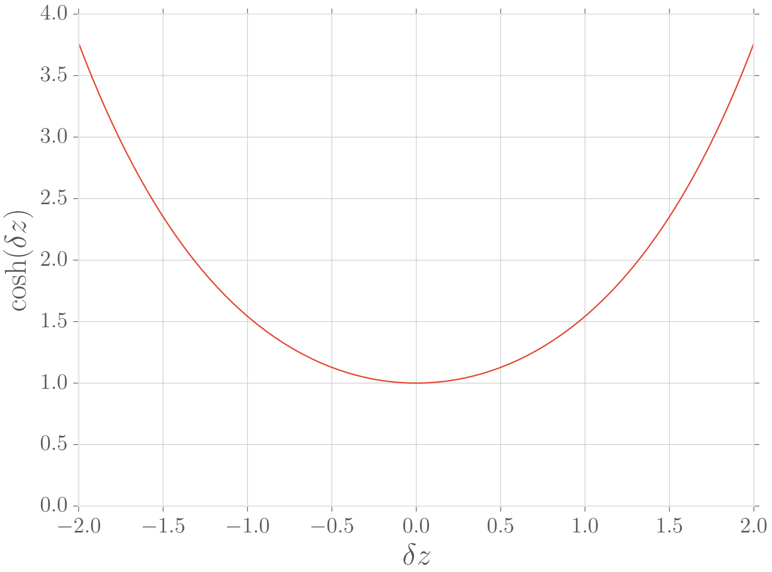

Figure 5.4: Plot of eq. 5.4 for $\alpha = 1$.

5.2.2 Transverse diffusion

The electron cluster is also subject to the transverse diffusion, perpendicular to the direction of the electric field. Since the propagation of the charges is only in 1 dimension we cannot directly compute the radial displacement of the electron cluster. However it can be approximated by computing the radial charge distribution.

The diffusion has been described in section 3.3.2. We assume the electron cluster has a rotational symmetry and the transverse charge distribution is only influenced by the transverse diffusion. The radial charge distribution will be given by eq. 3.31b

$$\varphi_T(r, l) = \frac{1}{D_T^2\, l} \exp\left(-\frac{r^2}{2D_T^2 l}\right). \tag{5.5}$$

In this case l is the total distance drifted by the electron during the avalanche. The more an electron has drifted the more it has been diffused radially and so the variance of eq. 3.31b $\sigma^2 = D_T^2 l$ increases. We set $r_0 = 0$ since we consider the avalanche to develop centred around the z-axis.

5.3 Space charge influence on the electric field

At a certain point during an avalanche, the space charge density in the detector becomes high enough to actually influences the applied electric field. To take into account this phenomena, we have to compute the contribution of all the charges present in the detector from eqs 3.37 and 3.34. The avalanche are propagated only along the z-axis, so only the z-component of the electric field is needed.

The point of observation is defined by (r, ϕ, z) and the position of the charge by (r', ϕ', z'). Since the simulation is only carried on the z-axis and we consider the electron distribution has a rotational symmetry we can simplify the computation of the potential to $(r = 0, \phi = 0, z)$ and (r', ϕ', z). Then the electric field of a charge radially distributed according to eq. 5.5 $\overline{E}_z(r = 0, \phi = 0, z, l, z') = \overline{E}_z(z, l, z')$ is given by [77]

$$\overline{E}_z(z, l, z') = \int_0^\infty \varphi_T(r', l(z'))\, E_z\left(r = 0, \phi = 0, z, r', \phi', z'\right) r' dr' . \tag{5.6}$$

The z-component of the electric field is given by eq 3.37c

$$E_z(r = 0, \phi = 0, z, r', \phi', z') = -\frac{\partial \Phi}{\partial z}\left(r = 0, \phi = 0, z, r', \phi', z'\right) . \tag{5.7}$$

The space charge field $E_{\mathrm{SC}_z}(z)$ resulting from all the charges present in the detector is computed by integrating eq. 5.6 over the gas gap length

$$E_{\mathrm{SC}_z}(z) = \int_0^g q(z')\, \overline{E}_z(z, l, z')\, \mathrm{d}z' , \tag{5.8}$$

with $q(z')$ the number of charges present at position z'.

However, dynamically computing the space charge field at all steps is very time consuming (many numerical integrations have to be carried out which is quite slow). As it was suggested in [77], in order to speed-up the simulation we pre-compute an interpolation table of $\overline{E}_z(z, l, z')$ for a specific number of values n for (z, l, z'). This table is loaded into memory before the avalanche simulation and actual values are given by interpolation. This interpolation table depends on some detector parameters which are the transverse diffusion coefficient, the gap length, the number of simulation steps, the resistive layers' permittivity and width. It needs to be re-computed only when one of those parameters is modified. Figure 5.5 shows the influence of the interpolation table size n on the precision. For $n = 30$ the differences are quite noticeable, whereas for $n = 100$ the differences are only visible for small values of l and almost negligible for $n = 140$.

This method allows to take into account, in an approximate way, the transverse dispersion of the electrons and their influence over the electric field without the need of a 2-dimensional propagation algorithm. However because we use a pre-computed interpolation table for the values of $\overline{E}_z(z, l, z')$, we use the value of the transverse diffusion coefficient at the initial electric field $D_T = D_T(E_0)$. This is equivalent to assume that D_T is constant during the simulation while in fact it will vary with the electric field (figure 3.7b). The figure 5.6 presents the difference between the electric field of a gaussian charge distribution with different variances σ, for a difference of 20% and 40%. In the first case there is a 30% difference in the electric field, it increases to 47% in the second case.

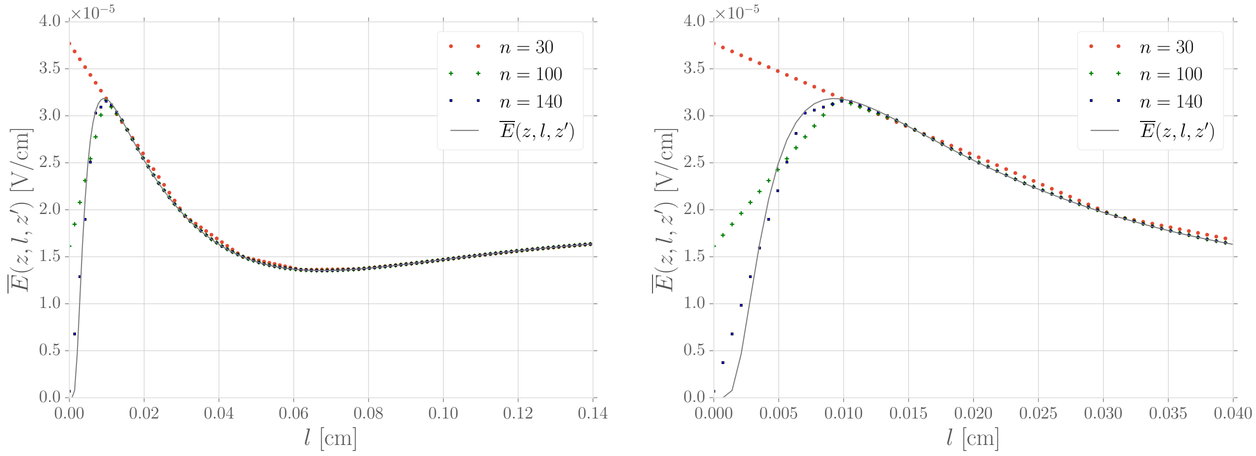

(a) **(b)**

Figure 5.5: Values of $\overline{E}(z,l,z')$ from eq. 5.6 and from interpolation for different table size n. We set $z = z' = 0.08$ cm. (b) is a zoom on the region $l \in [0, 0.04]$cm.

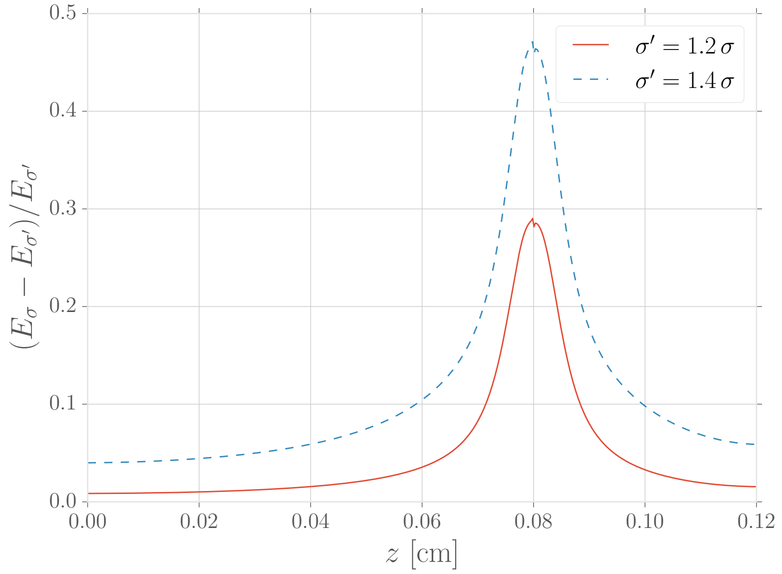

Figure 5.6: Difference between the electric field of three different gaussian charge distributions. The first distribution has a variance 20% higher than the reference and the second 30% higher. The distribution are centred on $z' = 0.08$ cm in a 0.12 cm gas gap.

It is also interesting to note that when a strong space charge effect is present, which is usually the case in the final stages of an avalanche, the repulsion due to the Coulomb force becomes important and may influence the diffusion, both longitudinal and transverse. It can reach a point where the influence of the Coulomb force may be stronger than the successive elastic collisions and, in this scenario, we may no longer consider the charge distribution by a gaussian.

So, in the end, our computation of the radial charge density might be overestimated.

5.3.1 Influence of the space charges on the avalanche development

As the space charges have an influence on the applied electric field, they also modify the value of the transport parameters. When the charge density in the gas gap becomes sufficiently important, the external electric field is modified enough to lower the global multiplication gain, when $\eta(E)$ and $\alpha(E)$ respectively increases and decreases.

Figure 5.7 shows two different avalanches in a 0.12 mm gap, divided in 200 steps, started by a single electron placed in the 20-th bin. In 5.7a the space charge field is not computed and the avalanche growth further than in 5.7b, where the space charge is taken into account. The electric field distortion by the space charge leads to a saturation in the electron multiplication. This appears around time step 300 on figure 5.7b, whereas in 5.7a the avalanche continues to grow until around time step 380 where the first electrons have reached the anode. We deliberately chose a low electric field so that the gain won't be too important in order to compute the avalanche without space charge effect in reasonable time, but high enough to see the impact of the space charges on the avalanche development.

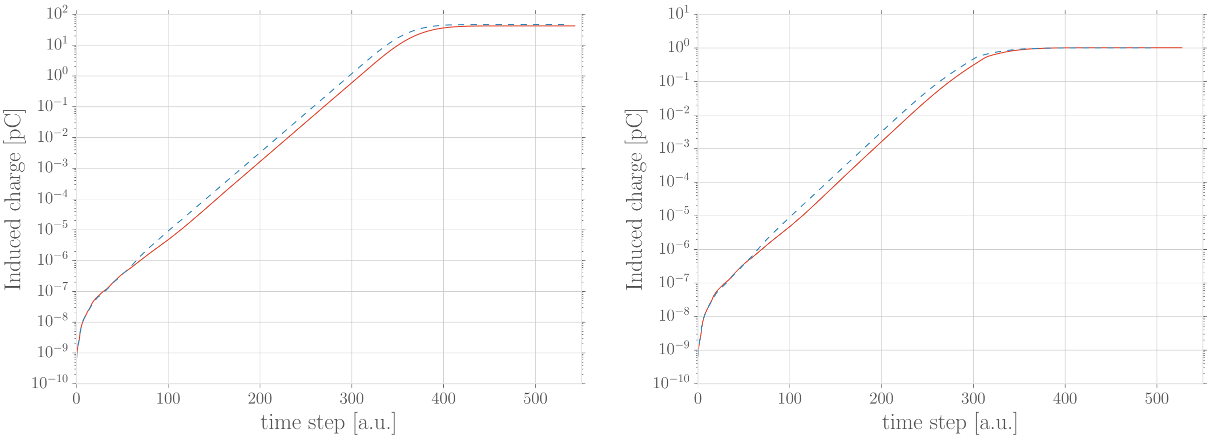

(a) **(b)**

Figure 5.7: Two distinct avalanches from a single electron in the 20-th bin. The 0.12 cm is divided in 200 steps and with an applied electric field of 54 kV/cm. (a) The space charge is not taken into account. (b) The space charge field is computed.

Figure 5.8 shows the charge distribution of an avalanche, along the electric field, in the detector at different time and illustrates the influence of the space charges during the development.

5.8a The charged particle (muon with momentum $p = 5\,\text{GeV}$) has ionised the gas and 28 free charges are distributed along the gap over different clusters. Some clusters have more electrons than others, mostly due to δ-electrons that ionise further (see section 2.2).

5.8b The clusters have grown and some have already reached the anode. Locally the charge density is important enough and begins to disturb the applied electric field.

5.8c At this stage the electric field is heavily modified by the space charges and has an important impact on the charge multiplication. Around position $z = 0.10\,\text{cm}$ the electric field is very high and the multiplication is also quite important but extremely localised. Whereas behind this position the field is lowered and so is the electron multiplication.

5.8d At the end of the avalanche, when no electron is present in the gas gap, the electric field is still quite perturbed. It is due to the negative and positive ion distributions, mostly concentrated in the vicinity of the anode, and the electrons present in the resistive anode that are yet to be relaxed (see 5.4).

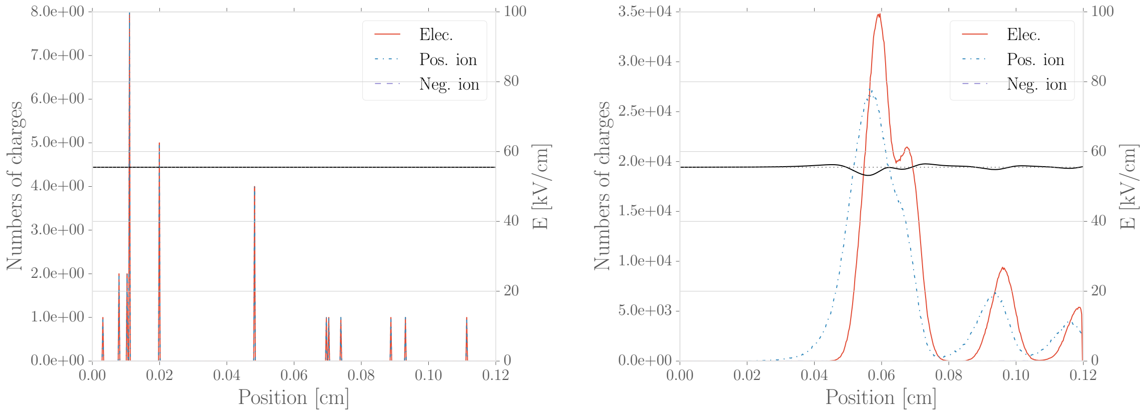

(a) timestep 0 ($t = 0\,\mathrm{ns}$) **(b)** timestep 399 ($t = 7.94\,\mathrm{ns}$)

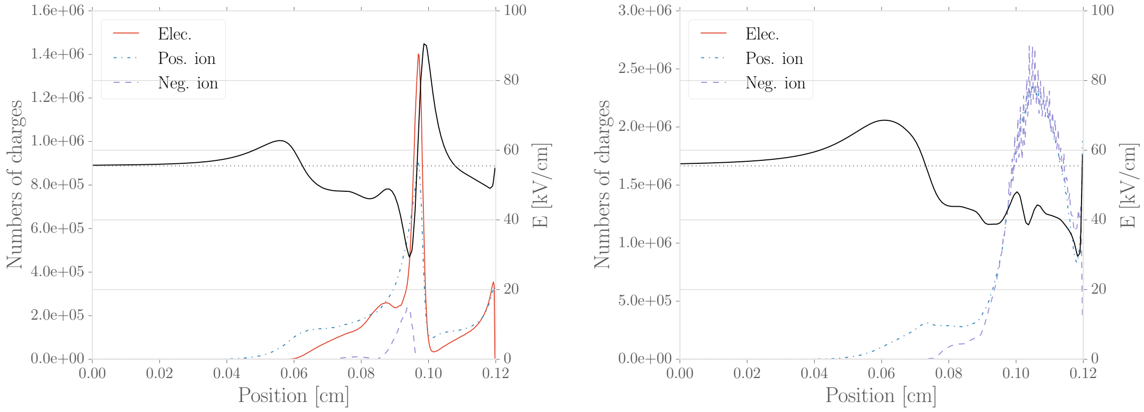

(c) timestep 449 ($t = 1.09\,\mathrm{ns}$) **(d)** timestep 1205 ($t = 23.9\,\mathrm{ns}$)

Figure 5.8: Electrons and ions distribution in the gas gap during an avalanche, at different timesteps, with the electric field. The gap width is 0.12 cm divided in 500 steps, the anode and cathode are respectively 0.07 and 0.11 cm wide with $\varepsilon_r = 7$. The external electric field is 55.5 kV/cm

An avalanche depicts a droplet-like shape, as shown on the figure 5.9. The electrons are located at the head of the droplet whereas the ions form the tail due to their much smaller drift velocity. The electrons located at the tip and the tail of the distribution are subject to an higher electric field than the applied one. The rise of the field at the tip is caused by the space charge of electrons, whereas at the tail it is due to the ions.

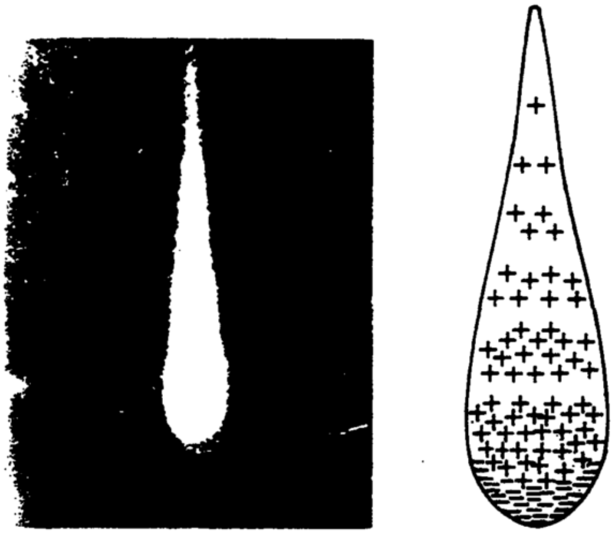

Figure 5.9: Droplet-like shape of an avalanche. The ions are left behind the fast moving electrons. The photography is from a cloud chamber. (From [93])

5.4 Relaxation of electrons in resistive layer

When electrons reach the resistive anode, they do not directly disappear and have an influence on the electric field inside the detector during a certain time. If we consider a charge Q_0 at the surface of a resistive material, the charge will evolve as

$$Q(t) = Q_0 \, e^{-t/\tau}. \tag{5.9}$$

The time constant τ is the electron relaxation time in the resistive material and is defined as [23]

$$\tau = \rho \, \varepsilon_0 \varepsilon_r, \tag{5.10}$$

with ρ the electric resistivity and $\varepsilon = \varepsilon_0 \varepsilon_r$ the dielectric permittivity of the resistive material.

A typical glass has a resistivity of $\rho = 10^{12}\,\Omega\,\text{cm}$ and a dielectric constant around $\varepsilon_r = 7$, leading to a relaxation time $\tau \approx 620\,\text{ms}$. The resistivity of Bakelite is about $\rho = 10^{11}\,\Omega\,\text{cm}$ with a dielectric constant around $\varepsilon = 5$, yielding a relaxation time $\tau \approx 44\,\text{ms}$. It is several orders of magnitude larger than a typical avalanche time, about 10 to 20 ns.

This difference in timing leads to an accumulation of charges at the surface of the resistive anode. Those electrons have an influence on the electric field, especially in the vicinity of the anode. In order to compute the electric field resulting of electrons on the anode we use eq. 5.6 $\overline{E}(z, l, z' = g)$. The electrons are still transversely distributed over a gaussian whose variance is linked to l, the total distance drifted by the electrons from the point of origin of the primary cluster to the anode.

5.5 Induced currents and charges

As they move in the electric field, the drifting electrons induce a current on the RPC electrodes (see section 3.5). Because of their small drift velocity, the negative and positive ions induce a much smaller signal than the electrons (see figure 3.6) and we neglect their contributions to the induced current.

In order to compute the induced currents and charges, we use eq. 3.40 with the expression of the weighting field associated to the detector's geometry. We consider a single-gap geometry described by figure 3.16, where the resistive layers are made of the same material and thus share the same dielectric constant. In this case we use eq. 3.45

$$I(t) = Q(t)\,v(t)\,\frac{E_w}{V_w}, \tag{5.11}$$

where $Q(t)$ is the number of charges in the detector at time t and v the drift velocity. $\frac{E_w}{V_w}$ represents the weighting field associated to the detector, which is a constant for a given geometry. In this case it is expressed by (see eq. 3.44)

$$\frac{E_w}{V_w} = \frac{\varepsilon_r}{d_1 + d_3 + d_2\varepsilon_r}. \tag{5.12}$$

In eq. 5.12 we have carried out the time integration of eq. 3.40, which only applies on the delta function of eq. 3.44. T0hus the time-independent expression for the weighing of eq. 5.12.

Assuming there is $N_i(\mathrm{t})$ electrons in the detector bin i at time t. They drift with a velocity $v_i(E_i(t))$, E_i being the electric field in bin i. Then the induced current in bin i at time t is

$$I_i(t) = N_i(t)\,e_0\,v_i(E_i(t))\,\frac{E_w}{V_w}. \tag{5.13}$$

The induced charge q_i is linked to the induced signal I_i through

$$q_i(t) = I_i(t)\,\delta t = N_i(t)\,e_0\,\delta z\,\frac{E_w}{V_w}, \tag{5.14}$$

where δt is the simulation time step and δz the detector step size. In order to have the total signal and charge induced at time t we sum eqs. 5.13 and 5.14 over the detector bins

$$I(t) = \sum_{i=1}^{N} N_i(t)\,e_0\,v_i(E_i(t))\,\frac{E_w}{V_w}, \tag{5.15a}$$

$$q(t) = \sum_{i=1}^{N} N_i(t)\,e_0\,\delta z\,\frac{E_w}{V_w}. \tag{5.15b}$$

The figure 5.10 exhibits the development of the induced signal over time.

5.6 Pseudo-random number generation and repeatability

As we have described in chapter 4, in any Monte-Carlo program it is vital to have a sound and efficient PRNG. We have decided to use well tested and documented generators:

- the classic Mersenne-Twister `MT19937` [82],
- the SIMD-oriented version of the Mersenne-Twister `SFMT` [91],
- the `RngStreams` package which implements the `MRG32k3a` generator [74].

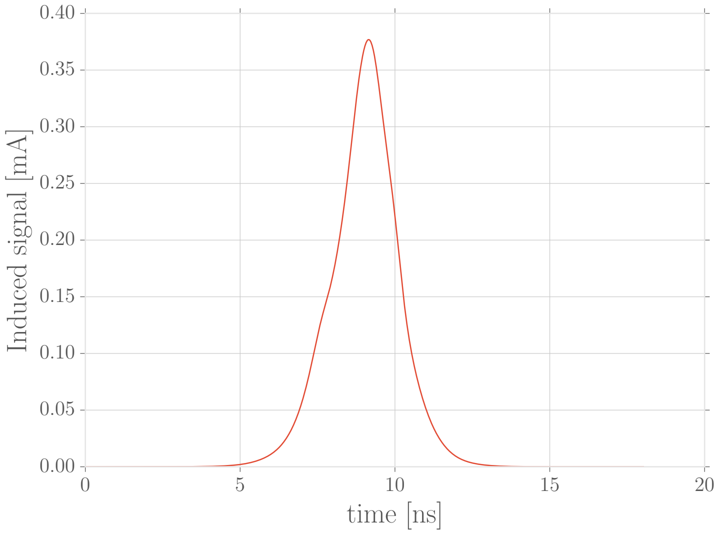

Figure 5.10: Signal induced on the electrode during an avalanche. The gap is 0.12 cm wide, the cathode and anode are 0.11 cm and 0.07 cm wide with a dielectric permittivity $\varepsilon_r = 7$. The applied tension is $57.5\,\mathrm{kV\,cm^{-1}}$.

We also need to create independent and non-overlapping stochastic sequences for parallel avalanches simulation. To do so we use different techniques adapted to the generator. With `MT19937` we make use of the `Dynamic Creator` algorithm [81] to produce parametrised streams. We use a jump-ahead algorithm [42] with `SFMT` to produce independent streams of sufficient length. And concerning `RngStreams`, it has its own sequence-splitting methods.

The `RngStreams` should definitely be the default generator in parallel environment for its ease of use. However it introduces some overhead when computing the output numbers and advancing the internal state, thus it may not be the best choice performance-wise. For this reason we have decided to use solely the Mersenne-Twister `MT19937` generator with `Dynamic Creator`. It offers the best performance and can easily create independent streams, from the avalanche simulation identifier for instance.

In the simulation, each stochastic physical process has its own random sequence. For example the electron multiplication method has its own parametrised generator which will yield random numbers only used in the electron multiplication computation. This is a necessary step to ensure the repeatability of the simulation results in a parallel environment [49].

We have tested the simulation on three different setups

- Intel i5-3230M running Ubuntu 15.04 64 bits, with `GCC` 4.9.2 and `ICC` 17.0.1
- Intel E5-4620 running CentOS 7.2.1511 64 bits, with `GCC` 4.8.5
- Intel E5-2698v3 running Scientific Linux 6.8 64 bits, with `GCC` 4.4.7 (CERN's lxplus machine)

To ensure the repeatability of the simulation, we compute the same avalanche (same geometry, same initial seed for `Garfield` and for our `Mersenne-Twister`) two times on each setup and compared the induced charges over time. In all cases we got the same results, i.e. the computed induced charge at each time step was the same on each run and on each setup. From these tests, we can conclude that the simulation is repeatable under different OS, compiler and hardware.

We use generators that have been thoroughly tested and are deemed repeatable and also portable. However repeatability issues may arise when using compiler and program of different architecture (for instance using a 64-bits generator with a 32-bits compiler) [33].

	i5-3230M		E5-4620	E5-2698v3
	`gcc`	`icc`		
`DCMT`	8.321 s	9.235 s	14.600 s	13.282 s
`MT19937`	7.032 s	6.262 s	8.4641 s	6.779 s
`SFMT`	1.248 s	1.713 s	2.747 s	2.383 s
`RngStreams`	27.803 s	30.240 s	39.302 s	37.935 s

Table 5.1: Time in seconds to generate 10^9 random numbers with the different generators.

Table 5.1 presents the performance of the different generators on the three setups. It was measured with the computing time needed to generate 10^9 random numbers. The `MRG32k3a` of `RngStreams` is the slowest of all, by about 3 to 4 times slower than `DCMT`, as we explained. Also one can remark a small overhead with `DCMT` compared to the classic `MT19937` due to the parametrisation. The fastest is clearly `SFMT` but is harder to implement in a parallel environment. In our case we make use of the jump-ahead algorithm [42] to distribute a sequence of 10^{20} to each thread. This sequence is then split, with the same algorithm, in several sequence of sufficient length for the different stochastic processes. It is important to note that this jump-ahead introduces some overhead while advancing the detector state. Though it should not have a too big impact on the performance (several milliseconds for a jump of 10^{20} random numbers) [79].

5.7 Organisation of the simulation

Concerning the simulation itself, we decided to develop it using object-oriented `C++` for performance. We tried to use as little as possible the `C++11` standard in order to run the simulation on clusters with old version of `gcc` (we tested down to `gcc 4.3.3` but not below).

Concerning the organisation of the code, we separated it in two big classes:

- All that is shared by the avalanches and relevant to the detector itself is handled by the class `TDetector`. This includes generating and reading gas tables from `Magboltz`, setting up the detector geometry and applied electric field, reading and computing $\bar{E}(z, l, z')$ tables ...
- The avalanche itself is handled by `TAvalanche1D` class, which gets a pointer to the `TDetector` instance. The `TDetector` instance is shared between all avalanches in order to optimise memory consumption. This class handles the avalanche itself: multiplication, propagation, diffusion, space charge effects ...

Once the detector instance is created and parametrised, the avalanches to simulate are distributed onto the several threads to use. To do that we used the `ThreadFactory`, which is part of the `HPCSim` framework [95, 48] and uses `POSIX Threads` standard. It takes into account the number of threads available on a system and seamlessly distribute the events to simulate on them.

The simulation runs on $N_t + 1$ threads, with one thread reserved to be the *master* thread. Its purpose is to spawn the worker threads and distribute the avalanches to compute, and to retrieve the results of finished avalanches and write them in an asynchronous way to a binary file.

The detector and simulation parameters are filled in an `xml` configuration file, which is parsed as an argument to the program. This file contains the geometry parameters (gap, anode and cathode width, plate permittivity, detection threshold), the gas informations (mixture compounds and percentage, temperature and pressure) and the simulation parameters such as the number of events to simulate, the number of thread to use and the random number generator seeds.

During the computations of $\bar{E}(z, l, z')$ we need to numerically evaluate semi-improper integrals (see section 5.3). At first we used the integration routines of `Gnu Scientific Library` which implements the `QUADPACK` methods [87] (Gauss-Konrod quadrature). However it sometimes had trouble converging. So we switched to a direct `C++` implementation of the Gauss-Legendre quadrature. It tends to be slower than the `GSL` but more robust in terms of convergence in our case.

Concerning the generation of standard normal random variables, we didn't want to rely on the `TRandom` classes of the `ROOT` framework. We directly implemented the same method [51], modified to accept any kind of PRNG.

The figure 5.11 shows the simulation profile, made using `gprof`. We can see that the computation of longitudinal diffusion is the most time-consuming, as individual electrons are relocated in the detector grid. The other time-consuming function is the interpolation from the $\bar{E}(z, l, z')$ table (though much less than the longitudinal diffusion). We used a simple and classic three dimensional interpolation method, so there is room for optimisations.

The figure 5.12 displays a class diagram of the program, highlighting the general layout of the code. Some helper classes as well as private attributes and methods are not displayed in order to improve visibility.

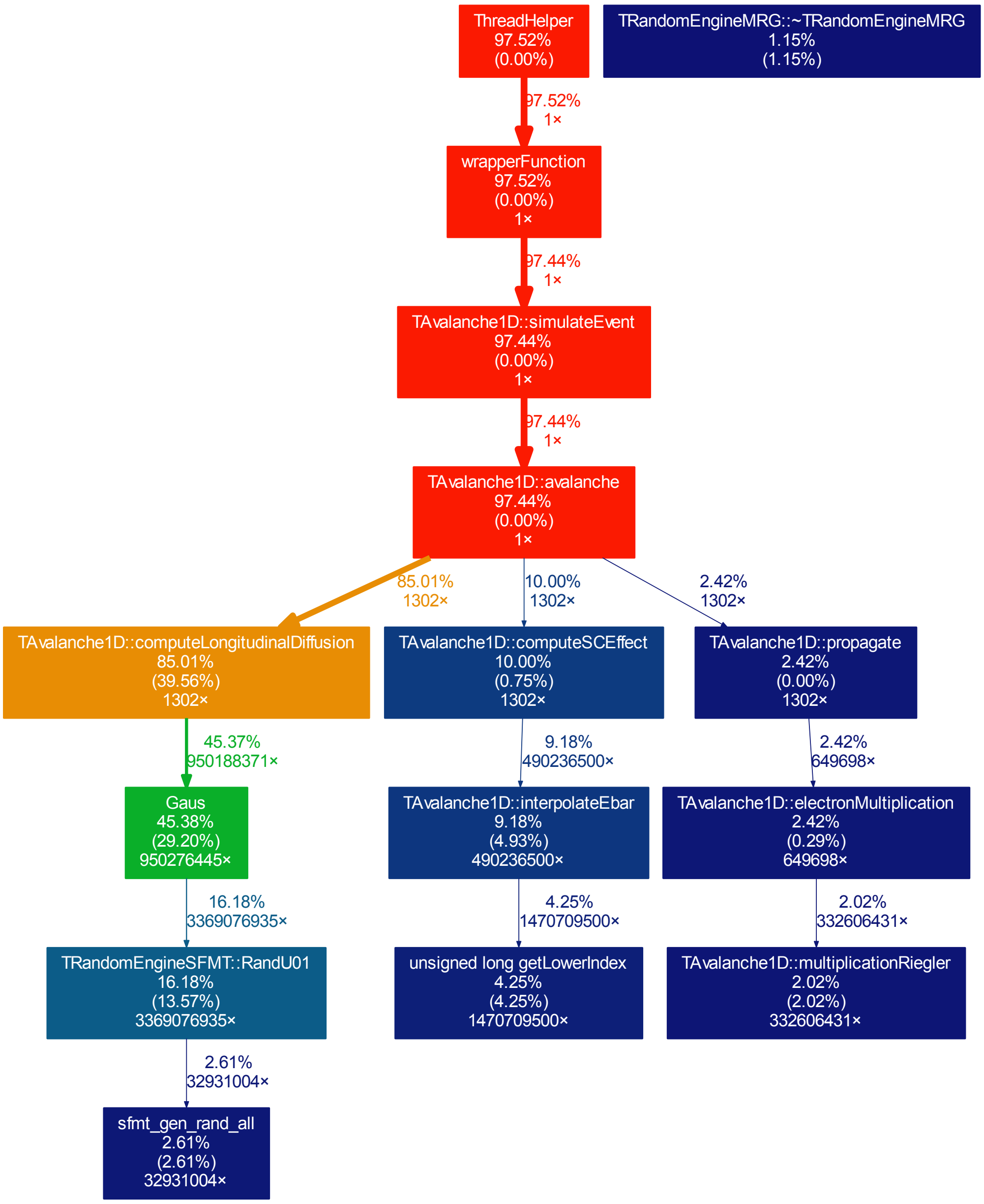

Figure 5.11: Profile of the simulation program obtained with `gprof`.

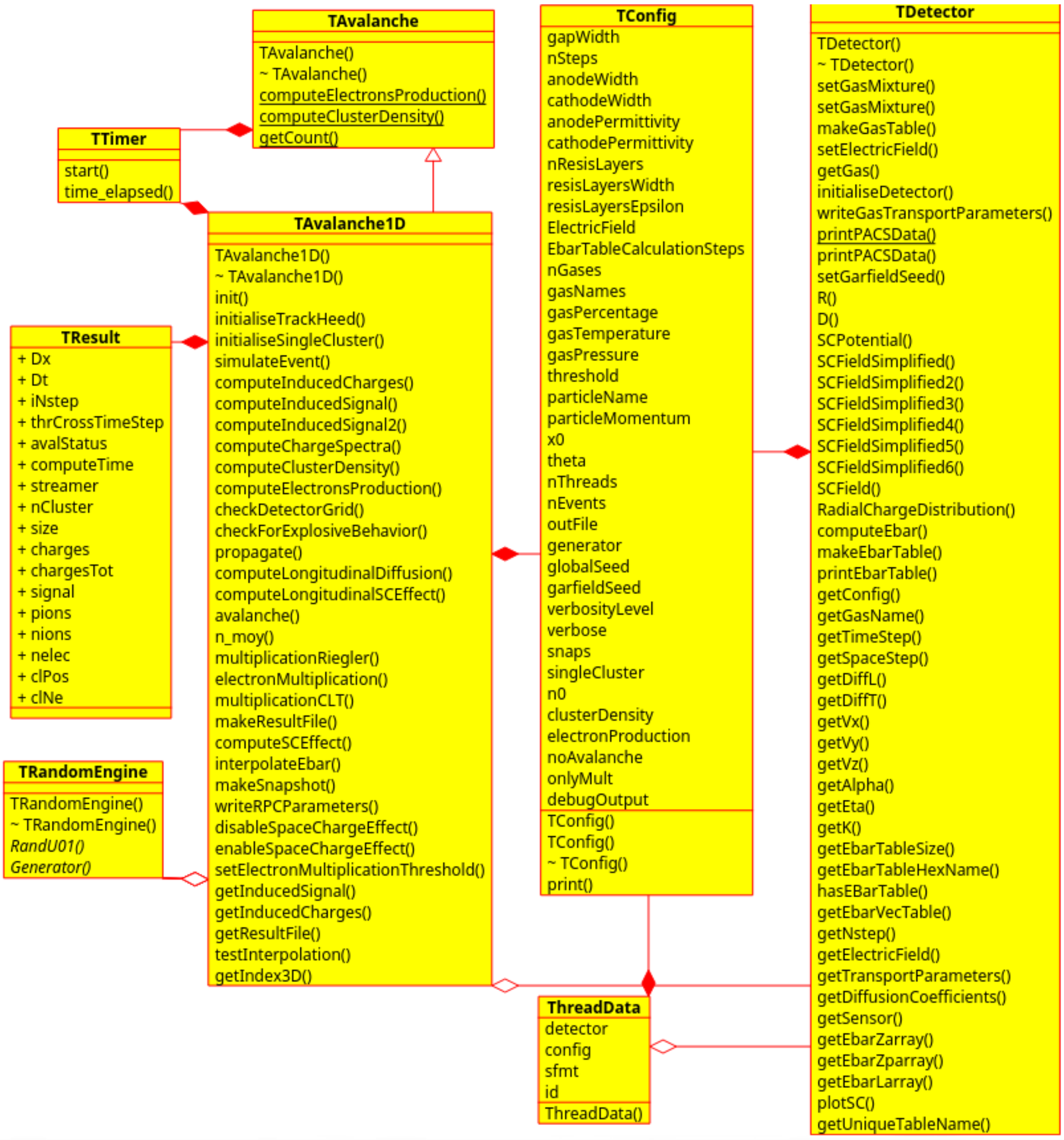

Figure 5.12: Class diagram of the simulation. Some helper classes and private attributes are not displayed.

Chapter 6

Results obtained with the simulation

In this chapter we first talk about expressions, that are derived in [90], used to compute analytically some RPC characteristics. Then we detail some results we obtained with the 1.5-dimensional simulation program, that has been described in chapter 5 using the model detailed in chapter 3.

6.1 Expected values from analytic expressions

We can calculate several expected detection parameters from analytic formulas. We consider the electron clusters exponentially distributed in the gas gap [90], thus the probability to find a cluster between x and $x + \mathrm{d}x$ is

$$P(x) = \frac{1}{\lambda} \exp\Big(-\frac{x}{\lambda}\Big). \tag{6.1}$$

λ is the average distance between clusters and $\lambda = \frac{1}{\bar{n}_{cl}}$, $\bar{n}_{cl}$ being the average number of clusters per unit of length (see figure 3.1). As we assumed the clusters are exponentially distributed in the gas gap, then the distribution of number of clusters is poissonian

$$P(n) = \frac{1}{n!}\Big(\frac{g}{\lambda}\Big)^n \exp\Big(-\frac{g}{\lambda}\Big), \tag{6.2}$$

where g is the gas gap length.

From these assumptions we can express the maximum efficiency reachable, by supposing that all the clusters produced are detected (that is impossible in practice, as it would involve an infinite gap length or a 0 Coulomb detection threshold). From eq. 6.2 the maximum efficiency is

$$\epsilon_{\mathrm{max}} = 1 - \exp\Big(-\frac{g}{\lambda}\Big), \tag{6.3}$$

where $\exp\big(-\frac{g}{\lambda}\big)$ is the probability to have no clusters in the gas gap $P(n = 0)$.

On average a single electron at the position x in the gas gap will induce a charge on the electrode given by

$$\bar{Q}_{ind}(x) = \frac{E_w}{V_w} \frac{e_0}{\alpha - \eta} e^{(\alpha-\eta)(g-x)} - 1. \tag{6.4}$$

Considering a detection threshold Q_t, the condition for a detected event is $\bar{Q}_{ind}(x) > Q_{\mathrm{thr}}$, this gives a condition on the position of generation of the electron $x < x_t$ [3]

$$x_t = g - \frac{1}{\alpha - \eta} \ln\left(1 + \frac{1}{\frac{E_w}{V_w}} \frac{\alpha - \eta}{e_0} Q_{\mathrm{thr}}\right). \tag{6.5}$$

The probability that the first cluster do not get attached and crosses the threshold is

$$P_1 = \left(1 - \frac{\eta}{\alpha}\right) \int_0^{x_t} \frac{1}{\lambda} \exp\left(-\frac{x}{\lambda}\right) \mathrm{d}x\,, \tag{6.6}$$

then the probability that the first cluster is attached but not the second and above the threshold is

$$P_2 = \int_0^{x_{t_1}} \int_0^{x_{t_2}} \frac{\eta}{\alpha} \frac{1}{\lambda} \exp\left(-\frac{x_1}{\lambda}\right) \times \left(1 - \frac{\eta}{\alpha}\right) \frac{1}{\lambda} \exp\left(-\frac{x_{t_2} - x_1}{\lambda}\right) \mathrm{d}x_1\, \mathrm{d}x_{t_2}\,. \tag{6.7}$$

Continuing the series to the n^{th} cluster we get the actual efficiency of a given RPC [90]

$$\epsilon = \sum_{n=1}^{\infty} P_n = 1 - e^{-\left(1-\frac{\eta}{\alpha}\right)\frac{g}{\lambda}} \left[1 + \frac{1}{\frac{E_w}{V_w}} \frac{\alpha - \eta}{e_0} Q_{\text{thr}}\right]^{\frac{1}{\alpha\lambda}}. \tag{6.8}$$

For this expression no space-charge effect is taken into account, that means that the value of η and α are constant. Also no diffusion is considered. Q_{thr} represents the detection threshold in Coulombs. In the case of an infinity gap length or a zero detection threshold, we find back the maximum efficiency eq. 6.3 as expected.

The induced signal of a RPC follows

$$I(t) = A\, e^{(\alpha-\eta)vt} \tag{6.9}$$

with A the signal amplitude. Setting up a detection threshold A_{thr}, this leads to an expression for the threshold crossing time

$$t(A) = \frac{1}{(\alpha - \eta)v_d} \ln\left(\frac{A_{\text{thr}}}{A}\right). \tag{6.10}$$

The distribution of threshold crossing time has the property that a shift in threshold correspond to a shift in time, meaning that the shape of the distribution is not influenced by the threshold [90]. From this distribution we have an expression for the time resolution of an RPC

$$\sigma_t = \frac{1.28}{(\alpha - \eta)v_d}. \tag{6.11}$$

Again no space-charge effect nor diffusion is accounted.

Figure 6.1 shows the maximum efficiency for different gap widths as a function of the muon momentum. As expected the curve has the shape of the Bethe formula, since the maximum efficiency is directly linked to the cluster density (see figure 3.1) $\bar{n}_{cl} = 1/\lambda$. The figure 6.2 exhibits the maximum efficiency as a function of the gap width for Argon and the CALICE sDHCAL mixture. As the Argon is less ionising the Forane (the cluster density is respectively 32.54 and 89.39 clusters per centimetre), it needs a wider gap to produce clusters.

gas	g [cm]	q [cm]	$p-g$ [cm]	ε_r	HV [kV/cm]	ϵ (ϵ_{max})	σ_t [ns]
$C_2H_2F_4/CO_2/SF_6$	0.12	0.11	0.07	7	57.5	97.6(99.9)	0.49

Table 6.1: Analytic performance for the CALICE sDHCAL RPC geometry.

Table 6.1 lists the CALICE sDHCAL RPC geometrical parameters along with the analytical performances.

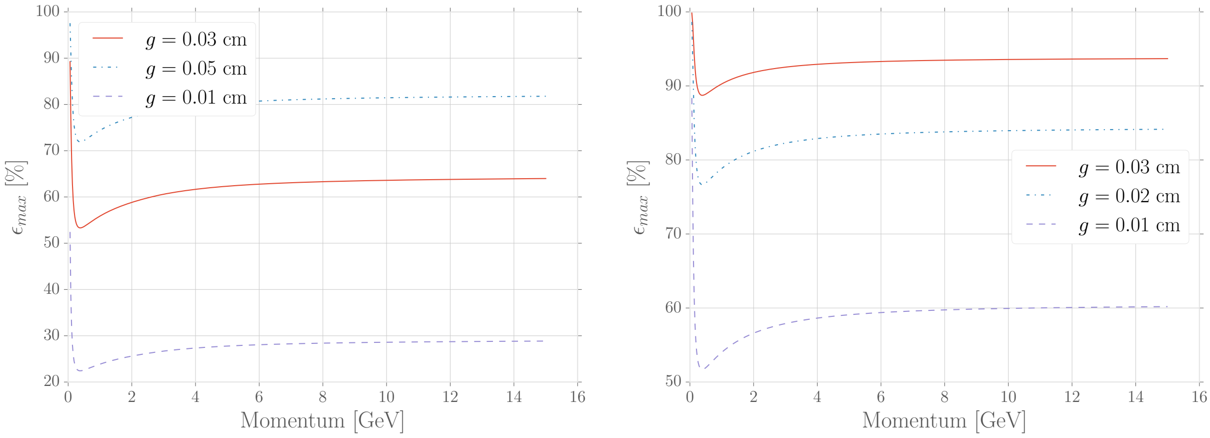

(a) Argon **(b)** $C_2H_2F_4/CO_2/SF_6$ 93%/5%/2%

Figure 6.1: The maximum efficiency (eq.6.3) as a function of the muon momentum, for different gap widths, in pure Argon and in the CALICE sDHCAL mixture.

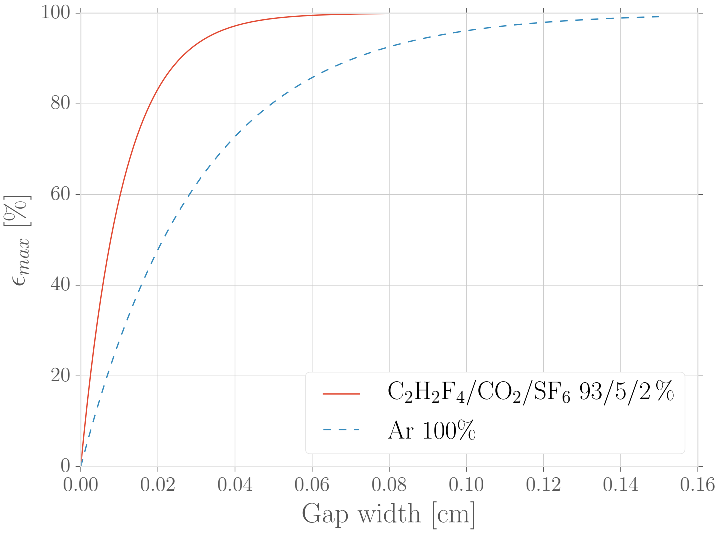

Figure 6.2: Maximum efficiency as a function of the gas gap width, for 5 GeV/c muon, in pure Argon and in the CALICE sDHCAL mixture.

6.2 Detection efficiency

Figure 6.3 shows the simulated efficiency for a CALICE sDHCAL RPC with 5 GeV/c muons. The gas gap is 0.12 cm and filled with a mixture of $C_2H_2F_4/SF_6/CO_2$ in the proportion 93/2/5% at temperature $T = 20\,°C$ and pressure $p = 760$ Torr (1 atm), the Bakelite anode and cathode width is respectively 0.07 cm and 0.11 cm with a dielectric permittivity $\varepsilon_r = 7$. The detection threshold is set to 0.1 pC. The analytic expression from eq. 6.8 is also plotted. The analytic formulation follows quite well the simulated results, though it underestimates the efficiency at the beginning of the plateau around $54\,\mathrm{kV\,cm^{-1}}$. Using eq. 6.3, the theoretical maximum efficiency reachable is $\varepsilon_{\max} = 99.99\%$, with $\bar{n}_{cl} = 91.85\,\mathrm{cm^{-1}}$.

The uncertainties are purely of statistical nature (Poissonian) in order to account

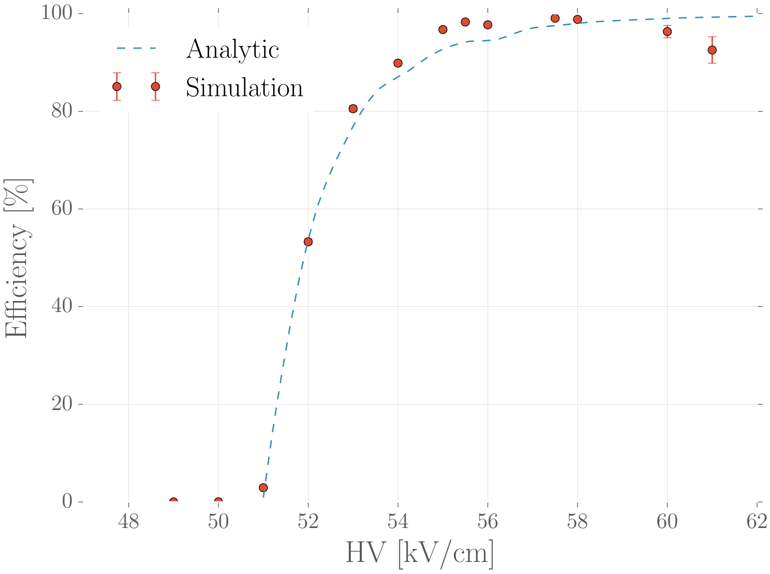

Figure 6.3: Simulated efficiency for a CALICE sDHCAL RPC with 5 GeV/c muons. The temperature is 293.15 K and the pressure is 760 Torr. The curve labeled Analytic represents eq. 6.8.

the poor statistics available towards high electric field, due to simulation instability (see section 6.2.1).

At the operation high tension of 57.5 kV cm^{-1} we obtain an efficiency of $99.06 \pm 1.19\%$, this is in good agreement with the experimental efficiency of around 96% measured during test beams [20]. The simulation gives only the intrinsic efficiency as the read-out electronics are not modelised, so it is expected to get a higher efficiency than the measurements.

Figure 6.4 shows the evolution of the efficiency with the detection threshold for two different applied electric fields. As expected, when the threshold augments the small avalanches that originated far from the cathode are not detected because they cannot develop enough before reaching the anode. It is as if the effective gas gap length was reduced. Using eq. 6.3 we can calculate the effective gap length for a given threshold. Figure 6.5 shows the effective gap length with the same RPC geometry, an electric field of 57.5 kV cm^{-1} and an average number of cluster $\bar{n}_{\text{cl}} = 89.37\,\text{cm}^{-1}$. At a detection threshold of 0.1 pC the effective gap length is only a little less than 45%. This would mean that any cluster produced farther than 0.54 mm of the cathode in this 1.2 mm gap would not be detected.

6.2.1 Simulation efficiency

One may notice the fluctuations when the efficiency plateau is reached. This comes from the fact that the simulation becomes less *efficient* at high fields, meaning that an avalanche computation may not be carried out to its end thus limiting the available statistic. The simulation tends to become unstable towards high applied voltage, when an exploding electric field may appear in the detector (very high and localised) leading to an important electron multiplication and thus an extremely long computing time. When such a behavior is detected, the simulation of the current avalanche is aborted.

Figure 6.6 shows the simulation efficiency, i.e. the ratio of the number of simulations carried out without error over the total number of avalanches simulated, as a function of the applied external electric field. The simulation exhibits an efficiency of almost 100%

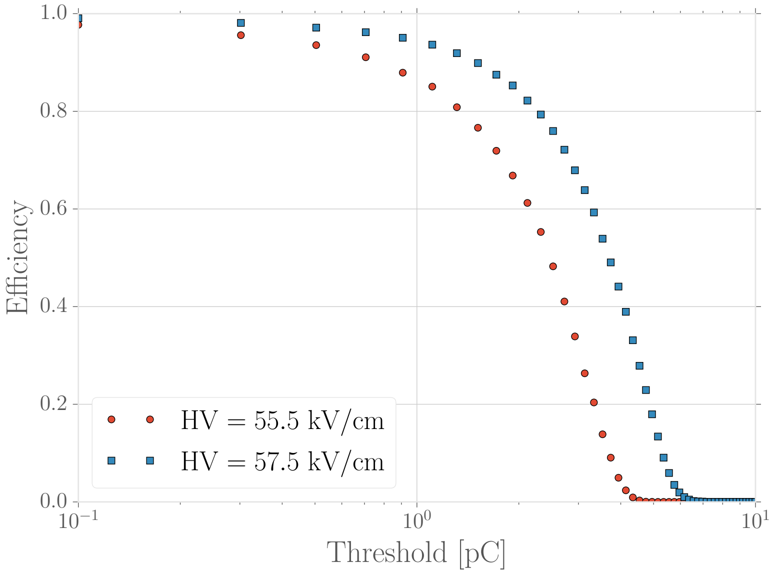

Figure 6.4: Efficiency as a function of the detection threshold. We used the CALICE RPC geometry and gas, with an applied electric field of 55.5 and 57.5 kV cm^{-1}

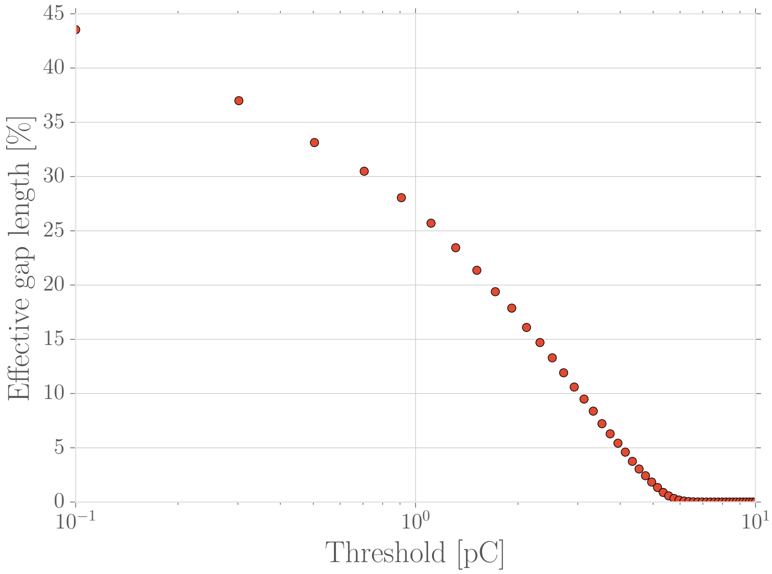

Figure 6.5: Effective gap length. We used the CALICE geometry, with an electric field of 57.5 kV cm^{-1} and 5 GeV/c muons.

at fields inferior to 56 kV cm^{-1} and then a quick and steady decrease, towards efficiencies below 10% from 60 kV. At the operation voltage of 57.5 kV cm^{-1} we have a simulation efficiency around 73%.

6.3 Threshold Crossing Time

We define the threshold crossing time as the time when the induced charge becomes superior to the detection threshold. The distribution of the threshold crossing time gives

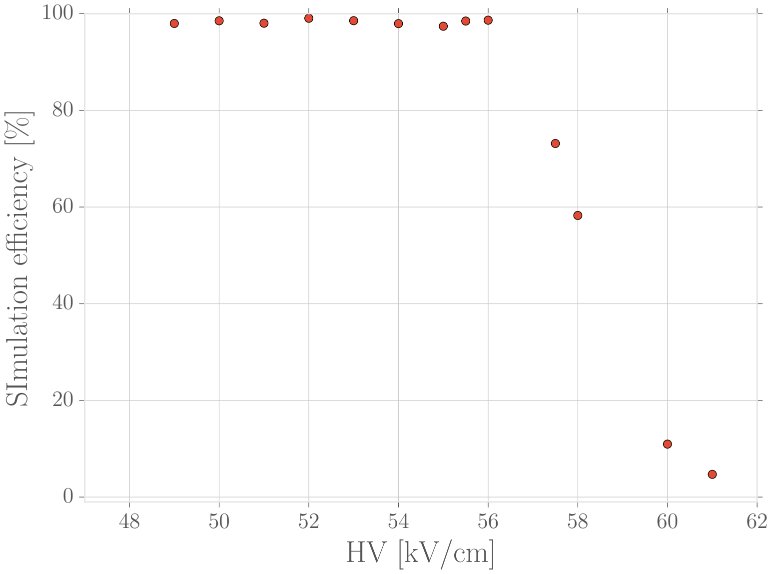

Figure 6.6: Simulation efficiency for the CALICE sDHCAL geometry.

the intrinsic time resolution of a RPC, i.e. the time resolution when no amplification or read-out electronics is taken into account.

Figures 6.7 show the distribution of the threshold crossing time for four different applied electric field, in a CALICE sDHCAL RPC with a detection threshold of 0.1 pC. A Gaussian is fitted to the distributions. As expected, the mean crossing time shifts towards smaller values when the applied electric field augments. A higher electric field means a higher electron multiplication gain and drift velocity, and thus the induced charge reaches the detection threshold faster.

One may notice that the distributions are not truly Gaussian, as they exhibit tails from either side. This can be explained by the fact that the primary ionisation, and thus the number of freed electrons in the gas gap, follows a Landau distribution with pronounced tails as it is depicted on figure 2.11.

The threshold crossing time is correlated to the initial number of electrons in the detector. A higher number of electrons implies an induced signal rising faster. This correlation is shown on figure 6.8. The exponential comes from the fact that the signal is proportional to the number of electrons present in the gap, which grows like $n_0 e^{(\alpha-\eta)z}$ where n_0 is the number of initial electrons.

The figure 6.9 shows the threshold crossing time as a function of the position of generation of the leading cluster. We define the leading cluster as the closest one to the anode. No correlation is visible, as expected, since all avalanches behave on average like a growing exponential. To be detected, an avalanche needs only one cluster far enough of the anode in order to induce a detectable signal.

6.4 Correlation between the charge and the threshold crossing time

The figure 6.10 exhibits the correlation between the intrinsic timing and the induced charge of a RPC. The vertical dashed line at the leftest part of the figure indicates the detection threshold of 0.1 pC, behind this line no avalanche can be detected and thus delimits the

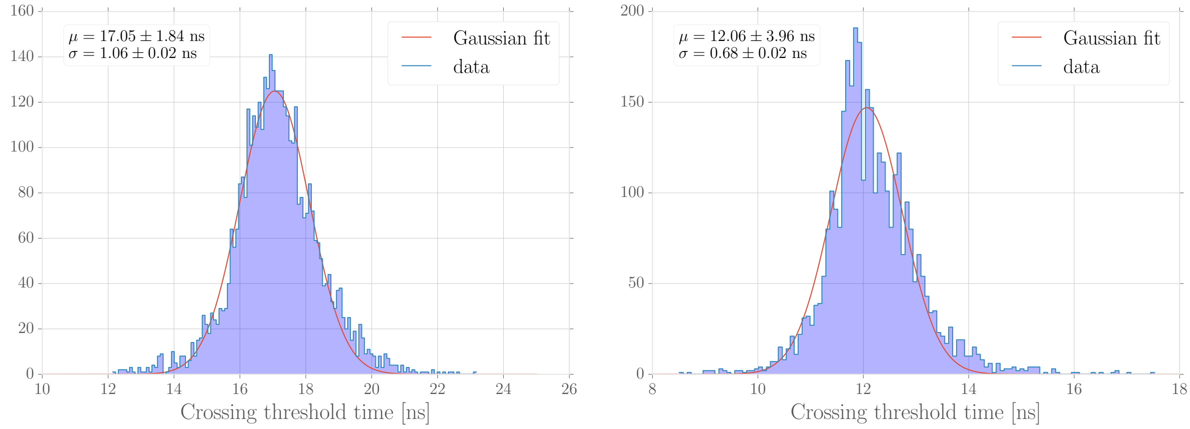

(a) 52 kV cm^{-1} **(b)** 54 kV cm^{-1}

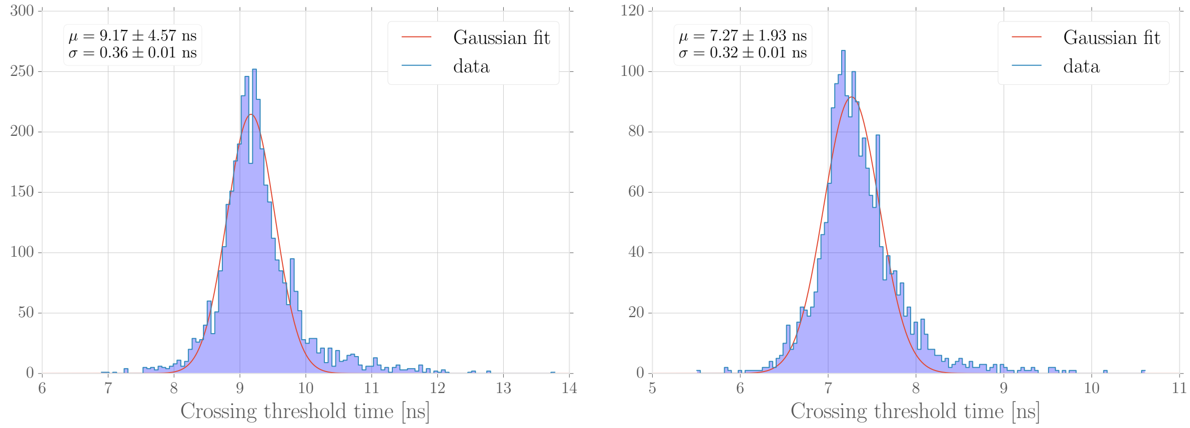

(c) 56 kV cm^{-1} **(d)** 58 kV cm^{-1}

Figure 6.7: Distributions of the threshold crossing times. We used the CALICE sDHCAL geometry and gas, the simulation was set to 500 steps and a detection threshold of 0.1 pC.

distribution.

The bottom part of the figure describes the avalanches that presented a fast induced signal development. But it is hard to distinguish a clear correlation. From figure 5.2 we know that the first stages of an avalanche determine its evolution and thus the time at which the threshold is crossed. The avalanches in this part of the plot may have been subject to an important initial electron multiplication. As we explained on section 6.3, the timing is correlated to the number of initial electrons: an avalanche with more initial electrons will crossed the detection threshold faster. The position of the leading cluster has an influence on the induced charge, as shown on figure 6.11b. A leading cluster generated close to the cathode will avalanche on a longer distance and thus induce a higher signal. However the number of initial electrons doesn't greatly influence the induced signal (see figure 6.11a), as the space charge effect kicks in.

On the upper part of the plot a clear correlation is visible between the intrinsic timing and the induced charge. In this part, the highest induced charges correspond to a leading cluster deposited close to the cathode with a high number of primary electrons or has undergone a quick multiplication in its early stage. By contrast, the avalanches with a slow induced signal development show a small induced charge. In this case one may picture a leading cluster close to the anode with a small number of primary electrons or a small

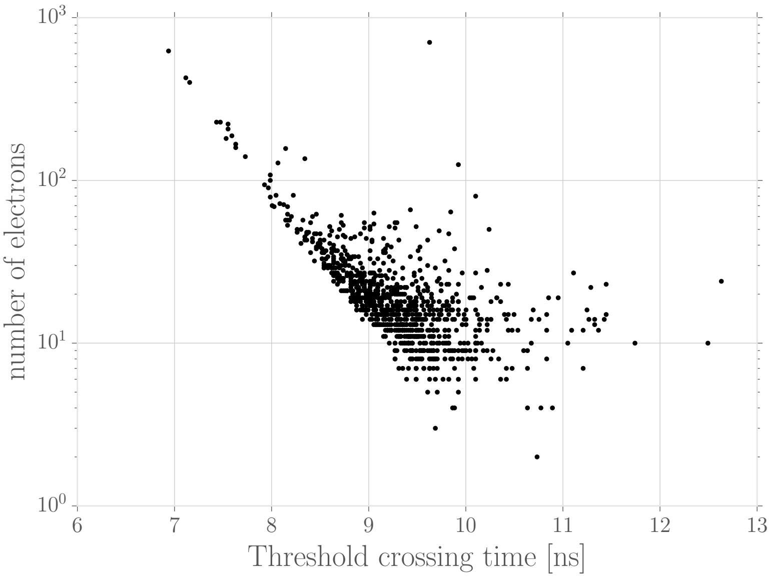

Figure 6.8: Correlation between the number of initial electrons and the threshold crossing time. The simulation was set to 500 steps with a detection threshold of 0.1 pC and an electric field of 56 kV cm^{-1}. We used the CALICE sDHCAL geometry.

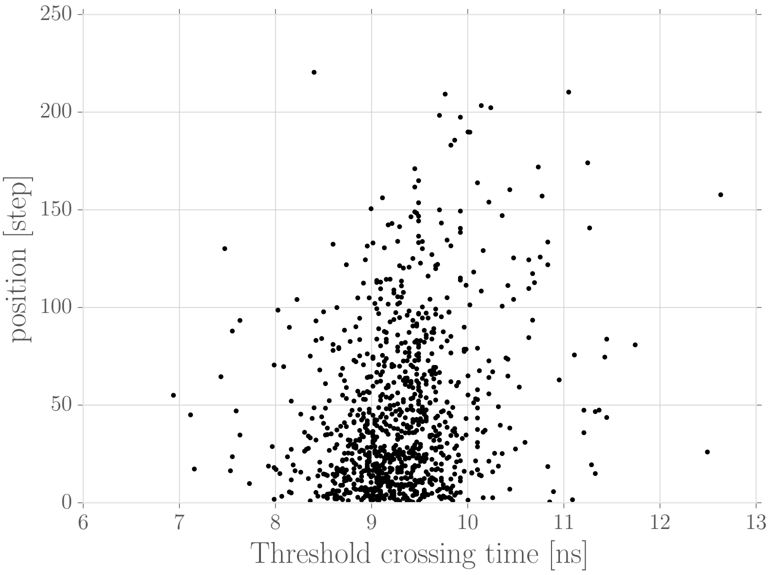

Figure 6.9: Threshold crossing time as a function of the position of generation of the leading cluster. The simulation was set to 500 steps with a detection threshold of 0.1 pC and an electric field of 56 kV cm^{-1}. We used the CALICE sDHCAL geometry.

early multiplication.

To further investigate this, the figure 6.12 shows the correlation of induced charge to the threshold crossing time for avalanche started by 1 electron, either at a random position or at the cathode. The avalanche that started at the cathode with a single electron exhibit the same behaviour than the avalanches that form the upper part of figure 6.11. So the fluctuations in the early development of an avalanche have a greater influence than the number of primary electrons on the intrinsic timing.

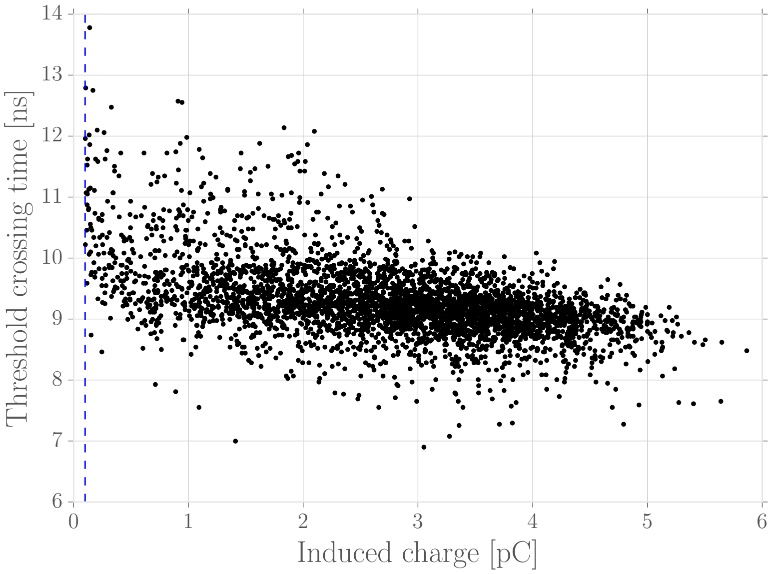

Figure 6.10: Correlation of the induced charge to the threshold crossing time. The detection threshold is 0.1 pC.

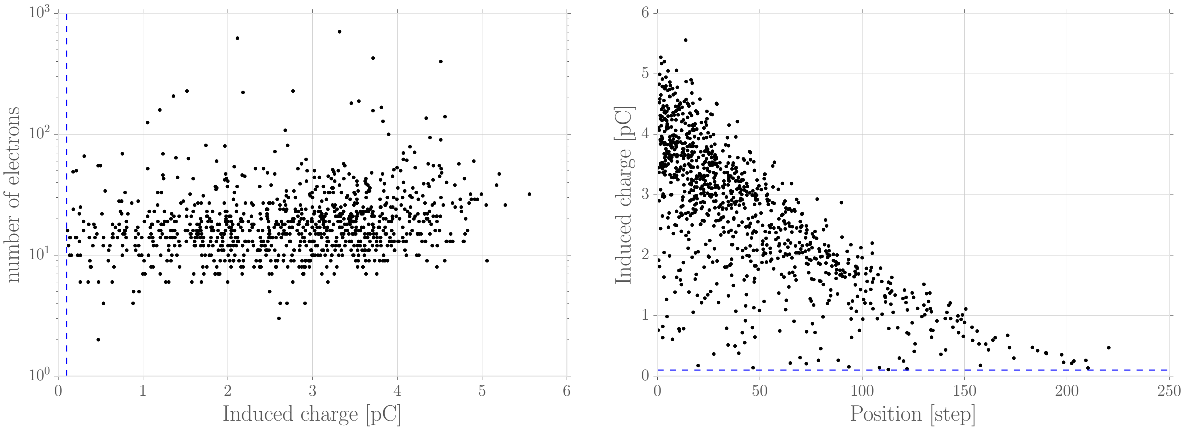

(a) **(b)**

Figure 6.11: Correlation of the number of electrons and position of leading cluster to the induced charge. The dashed vertical line represent the detection threshold.

6.5 Charge spectra

In this section we present the charge spectra obtained with our 1.5-D simulation. There are actually two kind of signal that are delivered by the RPC readout electrodes:

- the induced signal (also named fast signal) is, as described before, the signal induced by the movement of the electrons in the gap;
- the total signal is the charge induced by the slow moving ions.

Both signals appear on readout electrode on a different time scale, as shown on figure 6.13. In this model we have considered the ions stationary thus we cannot compute the value of the total signal charge. However by considering the charge of the positive ions left in

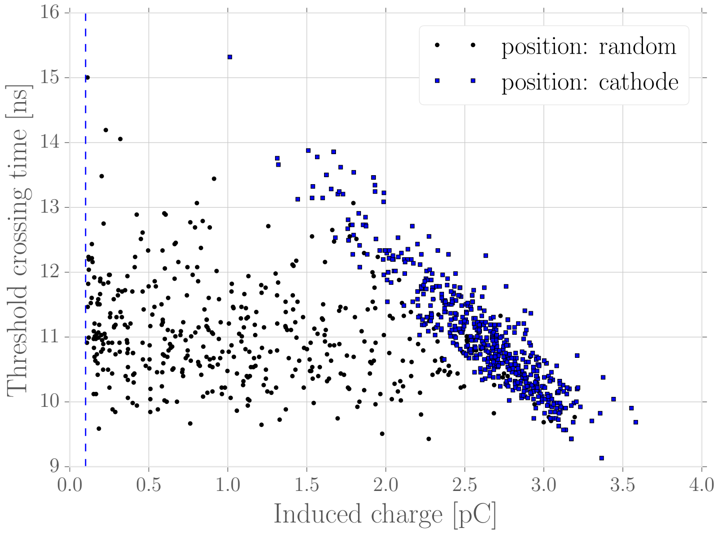

Figure 6.12: Correlation of the induced charge to the threshold crossing time in the case of avalanches started by one electrode, either at the cathode or at a random position in the gap. The detection threshold is 0.1 pC.

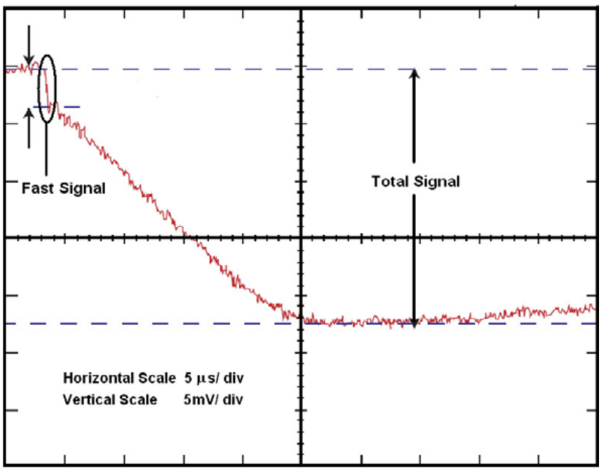

Figure 6.13: Typical signal detected on the readout electrodes of a RPC. The two different time scale represent the fast and total signal. (From [60]).

the gap at the end of the avalanche (i.e. when there are no electrons in the gap) we can get an insight of the induced charge on the cathode, and thus of the total signal.

Figure 6.14 and 6.15 show the accumulated induced and total charge spectra at three applied electric field (58, 56 and 54 kV cm^{-1}), for the CALICE sDHCAL geometry and gas. The simulation was set to 500 steps and a detection threshold at 0.1 pC. The following lists the mean induced and total charge, taking into account the non-detected events whose charge was inferior to the detection threshold:

- 54 kV cm^{-1} - $\langle Q_{ind} \rangle = 1.02\,\text{pC}$ $\quad \langle Q_{tot} \rangle = 7.48\,\text{pC}$,
- 56 kV cm^{-1} - $\langle Q_{ind} \rangle = 2.74\,\text{pC}$ $\quad \langle Q_{tot} \rangle = 31.3\,\text{pC}$,
- 58 kV cm^{-1} - $\langle Q_{ind} \rangle = 3.63\,\text{pC}$ $\quad \langle Q_{tot} \rangle = 71.9\,\text{pC}$.

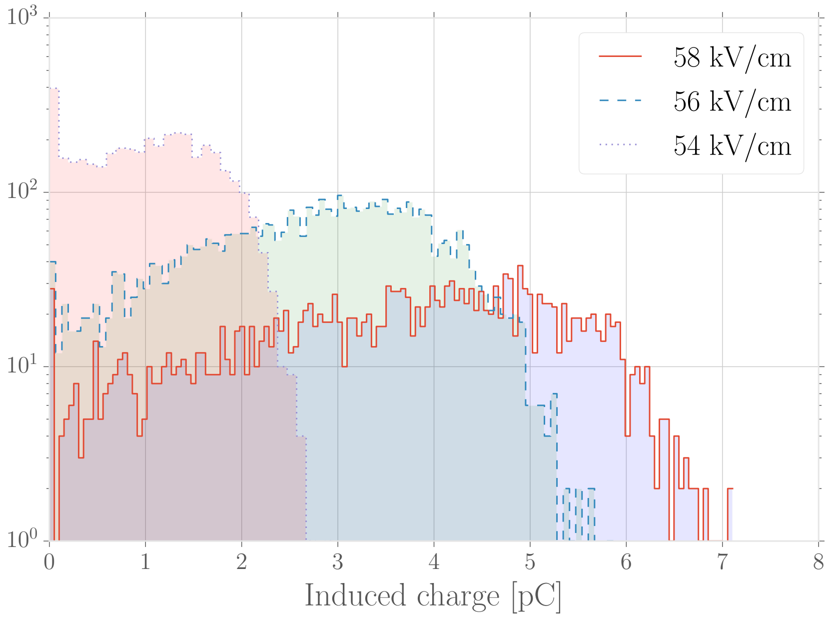

Figure 6.14: Induced charge spectra for the CALICE sDHCAL geometry.

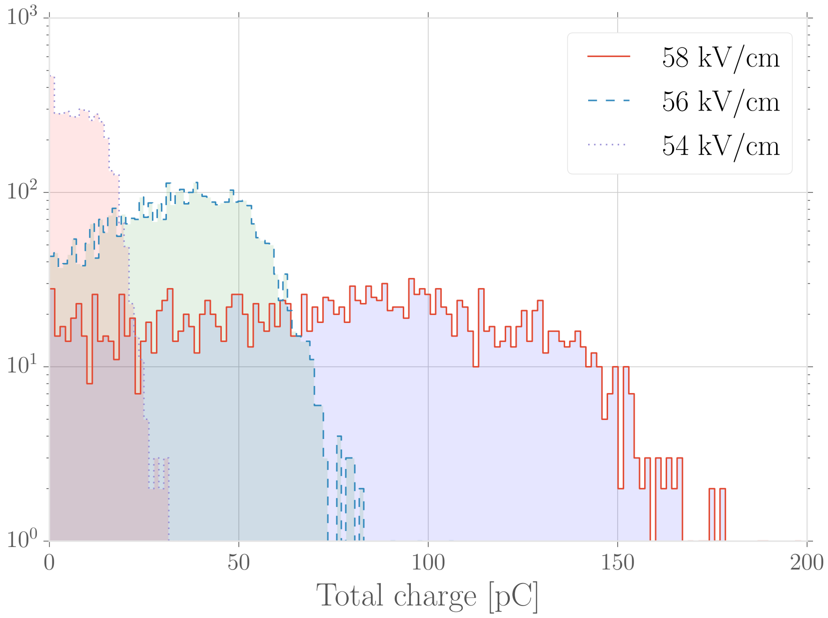

Figure 6.15: Total charge spectra for the CALICE sDHCAL geometry.

We find results that seem to be in agreement with experimental measurements, from [21, 6] for example.

6.6 Manifestation of the space charge on the signal development

The figure 6.16 exhibits the development of the induced signal on the anode over time for the same avalanche, with and without space charge effects, with an applied electric field of $56\,\mathrm{kV\,cm^{-1}}$. At the detection threshold of 0.1 pC the space charge effects already influence the avalanche electron production and thus the induced signal development. The detection time is shifted towards higher values with space charge effect as the multiplication gain gets, on average, lowered.

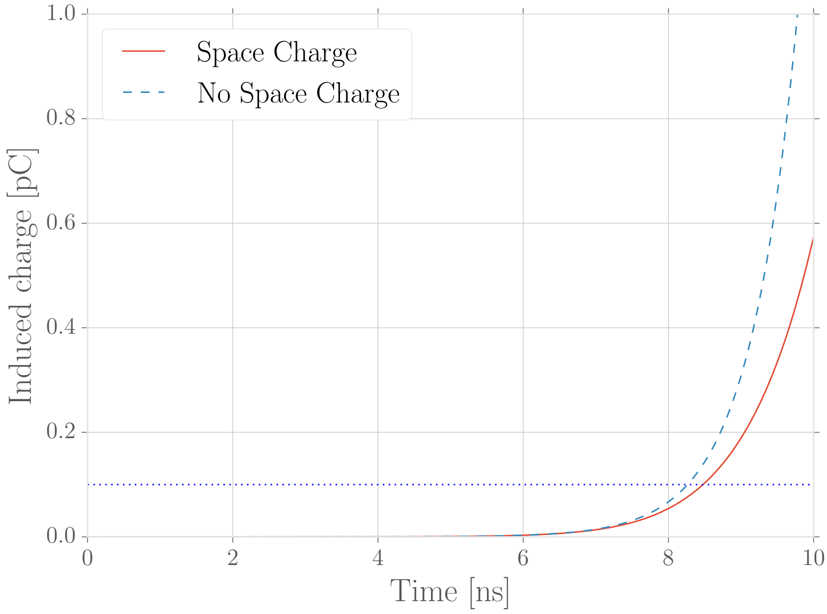

Figure 6.16: Development of the induced signal over time, with and without the space charge effects computed. We simulated the CALICE sDHCAL geometry on 500 steps at $56\,\mathrm{kV\,cm^{-1}}$. The dotted line represents the detection threshold of 0.1 pC.

The figure 6.17 presents the distribution of the threshold crossing time without the space charge effects, at $56\,\mathrm{kV\,cm^{-1}}$ and a detection threshold 0.1 pC. Compared to figure 6.7c, we do find that a mean crossing time shifted but we also have a slight increase of the standard deviation in the case of no space charge effects.

6.7 Intrinsic time resolution

The figure 6.18 shows the intrinsic time resolution of the CALICE sDHCAL RPC as a function of the applied electric field. The simulation is set to 500 steps with a detection threshold of 0.1 pC, at pressure 760 Torr and temperature 273.15 K. The time resolution is taken as the standard deviation of the distribution of the threshold crossing time (see figure 6.7). The analytical formulation eq. 6.11 is also plotted. We can see that the analytic expression doesn't match the simulated result. It underestimates the timings for electric field below the efficiency plateau and overestimates above. This may be explained by the fact that eq. 6.11 doesn't account the space charge effect nor the diffusion.

The time resolution obtained with this kind of RPC design is around 0.50 ns [49] at the operation of $57.5\,\mathrm{kV\,cm^{-1}}$, and our simulation gives a value around 0.30 ns. The

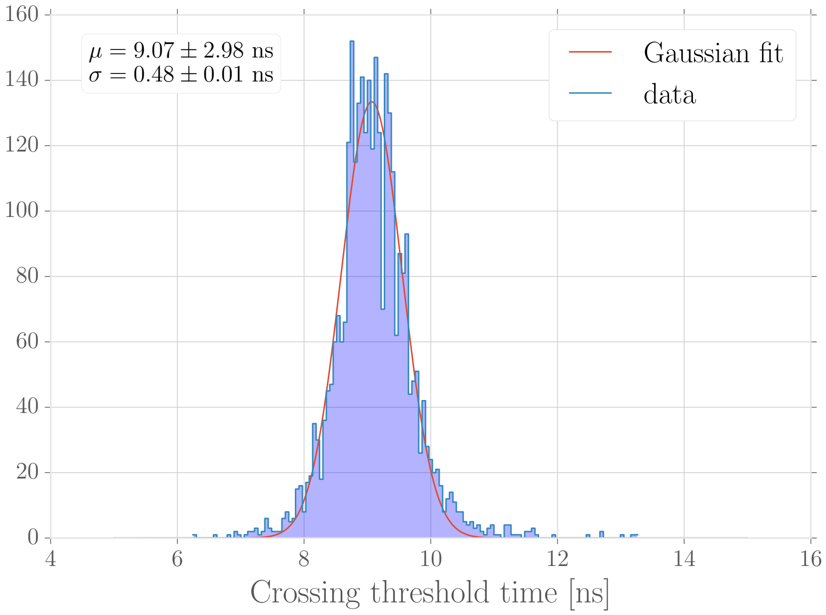

Figure 6.17: Distribution of the threshold crossing time without the space charge effects, at 56 kV cm^{-1}. The detection threshold is 0.1 pC.

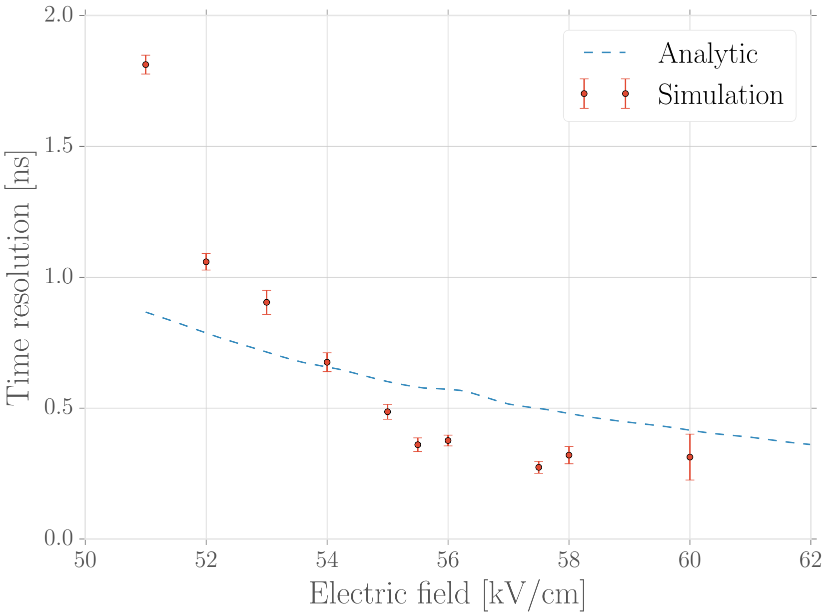

Figure 6.18: Simulated time resolution with the CALICE sDHCAL geometry. The simulation is set to 500 steps with a detection threshold of 0.1 pC, at pressure 760 Torr and temperature 273.15 K.

difference may be explained by the fact we measure the intrinsic time resolution, without any read-out and amplification electronics.

6.8 Streamer probability

We detailed the process of streamer formation on section 3.7. A streamer may appear as a consequence of two phenomenon:

- The remaining photons of a precursor avalanche may interact with the anode and cathode, generating knock-out electrons. Those electrons multiplies into an avalanche and merge together to form a streamer.

- The avalanche itself may evolve into a streamer under some conditions. The electron density and the space charge may reach a critical value where photons start to contributes to the avalanche by creating electron-ion pairs through photo-ionisation.

In the case a streamer reaches both the anode and cathode, a conductive channel is formed and provoke a spark discharge in the gas gap which is contained due to the high resistivity of the electrodes. Although rare in RPC operated in avalanche mode, a spark is an undesired effect as it reduces the rate capability but also may damage the read-out and amplification circuitry.

The streamer formation involves photonic processes that are note modelised in our simulation, thus we do not have access to the actual value of streamer occurrence. However we can consider an avalanche as evolved into a streamer if the number of electrons reaches $e^{20} \sim 4.85 \times 10^8$ [4, 22], thus giving a rough insight of the streamer probability.

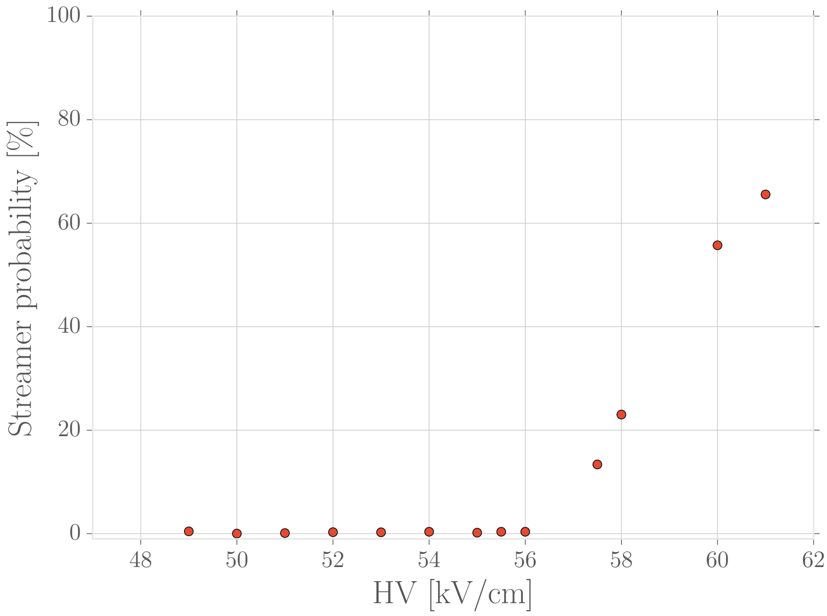

Figure 6.19: Simulated streamer probability with the CALICE sDHCAL geometry. The simulation is set to 500 steps with a detection threshold of 0.1 pC, at pressure 760 Torr and temperature 273.15 K.

The figure 6.19 shows the streamer probability in a CALICE sDHCAL RPC as a function of the applied electric field. Under 56 kV cm^{-1} the streamer probability is almost null, as the multiplication gain and space charge effects are not important enough. From this point the probability quickly rises. At the operating voltage of 57.5 kV cm^{-1} the probability is around 17%. At 61 kV cm^{-1} the streamer probability is over 61%.

6.9 Limits of the model and the simulation

We would like to point out the limitation of the model we used as well as the simulation towards high field.

- First of all, the simulation becomes heavily unstable because of the important number of electrons to modelise at high electric field (above around 59 kV cm^{-1}, see figure 6.6). This drastically limits the statistic we can accumulate on reasonable time.

- Secondly, in the Legler model, we make the assumption *that the ionisation probability is independent of the history of previous collisions* [90]. Considering U_i the ionisation potential and E the electric field, an electron has to travel $s = U_i/E$ to gain enough energy to ionise. The previous cited assumption is equivalent to the condition that s has to be small compared to the ionisation mean free path: $s \ll 1/\alpha$. This assumption does not hold any more at high fields, when s is comparable to $1/\alpha$ and the avalanche multiplication.

So in the end, when we tend toward high fields, the facts that the assumption behind the Legler model doesn't hold and the non-inclusion of the avalanche-to-streamer phenomenons (as it requires the knowledge of various photonic cross-sections and the inclusion of photo-ionisation models) make this simulation rather inadequate to the modelisation of RPC in avalanche mode. However, towards high fields, it is important to note that the RPC may not be operated in avalanche mode any more as we enter the streamer regime.

We would like to point out another limitation. Towards high electric fields the values given by `Magboltz` come with non-negligible uncertainties as measurements of α, η, drift velocity or diffusion coefficients are not available (see for example [35]).

Chapter 7

Conclusion

We have presented the fundamental physical processes underlying the ionisation of a gas by the passage of a charged particle, along with the development and propagation of an electronic avalanche in a Resistive Plate Chambers.

We have used a model first developed by Legler and continued by Rigler, Lippmann and Veenhof for the multiplication and propagation of electrons inside a Townsend avalanche. In this model the electric field is dynamically computed, with the contribution from all the charge carrier in the gas gap, thus modifying the avalanche dynamics. This is the so-called space charge effect. It turns out that these effects are essentials in the modelisation of avalanches inside RPC, as they account for a saturation in the multiplication processes at a certain point which is needed to find coherent induced signals.

With the developed simulation program, we computed several detection characteristics of a CALICE sDHCAL RPC. Although we did not modelise any amplification or read-out electronics, we have found coherent results in terms of detection efficiency and time resolution.

However the simulation tends to be unstable towards high electric field, because of the tremendous number of dynamically propagated electrons. In this regime, non-negligible uncertainties may arise from the values yielded by `Magboltz` as experimental measurements are unavailable. Moreover, when considering high fields, our simulation becomes unadapted as the assumptions behind the Legler model doesn't hold any more in addition to the non-inclusion of avalanche to streamer transition phenomena, which involves gas photo-ionisation modelisation.

A multi-thread simulation program of RPC has been developed during this thesis, implementing the Rigler-Lippmann-Veenhof model in the 1.5 dimension version. This allows to compute detection characteristics, such as induced signals spectra, efficiency or time resolution, with coherent results. In this model, the electrons are radially distributed following a Gaussian depending on the transverse diffusion coefficient of the gas. When computing the space charge field we only consider the centre of the Gaussian at $r = 0$, where the electron density is the highest. This leads to an overestimation of the saturation of electron multiplication in the space charge regime, compared to a 2 dimensional simulation [77].

A 2D model gives more precise result but on a different computation time scale. An avalanche with the 1.5D model takes some minutes, depending on the CPU and the simulation parameters, whereas a 2D avalanche computation would take around a day. In order to speed-up the simulation with this model one may consider the many-cores computer architecture, such as the Intel Xeon Phi, to compute a great number of avalanche in parallel. In this model, the propagation of electrons following the electric field lines takes the most time. In order to speed-up this process one may consider the vector nature of GPUs and use `OpenCl` or `CUDA` libraries. This could also give a non-negligible speed-up concerning random number generation, but one has to be extra careful about reproducibility in this case.

Concerning the gaseous mixture, which is the *heart* of a RPC, we rely on gas definitions of the `HEED` and `Magboltz` software. As new directives from the European Union will ban the use of high Global Warmth Potential gases in the near future, such as $C_2H_2F_4$ and SF_6, new gaseous mixtures are actively investigated for RPC use. However those alternative gases are not common in High Energy Physics experiment and gas definitions are not yet available in `Magboltz`, thus making the simulation of RPC with such gases impossible at the time.

Appendix A

Induced current in presence of resistive materials

Induced signal on a grounded electrode by a moving charge Q can be computed by use of Ramo's theorem (see eq. 3.39) assuming perfectly conducting electrodes surrounded by insulating materials, in which case electric fields are instantaneous. Considering a detector including resistive materials, time-dependent fields will arise and the Ramo theorem won't be applicable any more.

The derivation of the induced signal and charges is done in [89]. In this appendix we merely detail the calculus steps.

Maxwell's equations for medium with permittivity $\varepsilon(\vec{x},t)$ and conductivity $\sigma(\vec{x},t)$ are as follow

$$\vec{\nabla}\vec{D}=\rho, \qquad \vec{\nabla}\vec{B}=0, \tag{A.1}$$

$$\vec{\nabla}\wedge\vec{E}=-\tfrac{\partial\vec{B}}{\partial t}, \qquad \vec{\nabla}\wedge\vec{H}=\vec{j_e}+\sigma\vec{E}+\tfrac{\partial\vec{D}}{\partial t}. \tag{A.2}$$

with $\vec{D}=\varepsilon\vec{E}$, $\vec{B}=\mu\vec{H}$. $\vec{j_e}$ represents an external current generated by an external moving charge $\vec{\nabla}\vec{j_e}=-\frac{\partial\rho_e}{\partial t}$, and $\sigma\vec{E}$ arises from surface charges (conductors). We assume a weak conductivity, therefore

$$\vec{\nabla}\wedge\vec{E}=-\frac{\partial\vec{B}}{\partial t}=0 \;\Rightarrow\; \vec{E}=-\vec{\nabla}\Phi$$

Taking the divergence of the second relation in eq. A.2 we have

$$\vec{\nabla}\left[\vec{\nabla}\wedge\vec{H}\right]=-\frac{\partial\rho_e}{\partial t}-\vec{\nabla}\left[\sigma\vec{\nabla}\right]\Phi-\vec{\nabla}\left[\varepsilon\vec{\nabla}\right]\frac{\partial\Phi}{\partial t},$$

$$0=\frac{\partial\rho_e}{\partial t}+\vec{\nabla}\left[\sigma\vec{\nabla}\right]\Phi+\vec{\nabla}\left[\varepsilon\vec{\nabla}\right]\frac{\partial\Phi}{\partial t}. \tag{A.3}$$

In order to take into account the time-dependence of ε and σ we use the Laplace transform

$$\mathcal{L}\left[\Phi\left(\vec{x},t\right)\right]=\bar{\Phi}\left(\vec{x},s\right), \quad \mathcal{L}\left[\frac{\partial\Phi\left(\vec{x},t\right)}{\partial t}\right]=s\bar{\Phi}\left(\vec{x},s\right),$$

and so on. Eq. A.3 then becomes

$$-s\bar{\rho}_e\left(\vec{x},s\right)=\vec{\nabla}\left[\sigma\left(\vec{x},s\right)\vec{\nabla}\right]\bar{\Phi}\left(\vec{x},s\right)+\vec{\nabla}\left[\varepsilon\left(\vec{x},s\right)\vec{\nabla}\right]s\bar{\Phi}\left(\vec{x},s\right),$$

$$-\bar{\rho}_e\left(\vec{x},s\right)=\vec{\nabla}\left[\left(\varepsilon\left(\vec{x},s\right)+\frac{1}{s}\sigma\left(\vec{x},s\right)\right)\vec{\nabla}\right]\bar{\Phi}\left(\vec{x},s\right),$$

$$-\bar{\rho}_e\left(\vec{x},s\right)=\vec{\nabla}\left[\xi\left(\vec{x},s\right)\vec{\nabla}\right]\bar{\Phi}\left(\vec{x},s\right), \quad \bar{V}_i(s)=\bar{\Phi}(\vec{x},s)|_{\vec{x}=S_i}, \tag{A.4}$$

with $\xi\left(\vec{x},s\right) = \varepsilon\left(\vec{x},s\right) + \frac{1}{s}\sigma\left(\vec{x},s\right)$ and where V_i is the voltage on the i-th electrode. We use a modified Green's theorem [89]

$$\int_V \left\{\psi(\vec{x})\vec{\nabla}\left[f(\vec{x})\vec{\nabla}\right]\phi(\vec{x}) - \phi(\vec{x})\vec{\nabla}\left[f(\vec{x})\vec{\nabla}\right]\psi(\vec{x})\right\} \mathrm{d}^3x = \int_S \left\{\psi(\vec{x})f(\vec{x})\frac{\partial\phi(\vec{x})}{\partial\vec{n}} - \phi(\vec{x})f(\vec{x})\frac{\partial\psi(\vec{x})}{\partial\vec{n}}\right\} \mathrm{d}A \tag{A.5}$$

where surface S enclose the volume V. We replace $\phi(\vec{x})$ by $\bar{\Phi}(\vec{x},s)$, $f(\vec{x})$ by $\xi(\vec{x},s)$ and ψ can still be arbitrary chosen. We it as the potential if we remove the charge $\bar{\Psi}$ and we have

$$\vec{\nabla}\left[\xi(\vec{x},s)\vec{\nabla}\right]\bar{\Psi}(\vec{x},s) = 0, \quad \bar{v}_i(s) = \bar{\Psi}(\vec{x},s)|_{\vec{x}=S_i}.$$

We replace in eq. A.5 where the volume V is enclosed by the surface of the electrodes $S = \sum S_i$

$$\int_V \left\{\bar{\Psi}(\vec{x},s)\vec{\nabla}\left[\xi(\vec{x},s)\vec{\nabla}\right]\bar{\Phi}(\vec{s},s)\right\} \mathrm{d}^3x = \int_S \left[\bar{\Psi}(\vec{x},s)\xi(\vec{x},s)\frac{\partial\bar{\Phi}(\vec{x},s)}{\partial\vec{n}} - \bar{\Phi}(\vec{x},s)\xi(\vec{x},s)\frac{\partial\bar{\Psi}(\vec{x},s)}{\partial\vec{n}}\right] \mathrm{d}A \tag{A.6}$$

The charges on electrodes surface and the current are defined by

$$\begin{aligned} Q_i(s) &= \int_{S_i} \varepsilon(\vec{x},s)\frac{\partial\bar{\Phi}(\vec{x},s)}{\partial\vec{n}}\,\mathrm{d}\vec{A} \\ I_i(s) &= \int_{S_i} \sigma(\vec{x},s)\frac{\partial\bar{\Phi}(\vec{x},s)}{\partial\vec{n}}\,\mathrm{d}\vec{A}\,. \end{aligned} \tag{A.7}$$

We assume the electrodes grounded, so $V_i(t) = 0$ and the time-dependent charge density induces currents flowing between electrodes and ground $I_i^G(t)$ satisfying

$$\frac{dQ_i(t)}{dt} + I_i(t) = I_i^G(t) \;\rightarrow\; s\bar{Q}_i(s) + \bar{I}_i(s) = \bar{I}_i^G(s). \tag{A.8}$$

Combining eqs. A.6, A.7 and A.8 we obtain

$$-\int_V s\bar{\Psi}(\vec{x},s)\bar{\rho}(\vec{x},s)\,\mathrm{d}^3x = \sum_i \bar{v}_i(s)\bar{I}_i^G(s). \tag{A.9}$$

By defining Ψ by applying a voltage pulse $v_1(t) = v_0\delta t \rightarrow \bar{v}_1(s) = v_0$ on electrode 1 and leaving the others grounded we get the relation for induced current on the electrode

$$-\int_V s\bar{\Psi}(\vec{x},s)\bar{\rho}(\vec{x},s)\,\mathrm{d}^3x = v_0\bar{I}_1^G(s),$$

and switching back to the time domain using the inverse Laplace transform we get

$$v_0 I_1^G(t) = -\int_V\int_0^t \Psi(\vec{x},t-t')\frac{\partial\rho(\vec{x},t-t')}{\partial t'}\,\mathrm{d}^3x\,\mathrm{d}t'\,. \tag{A.10}$$

If the medium conductivity σ is null the time dependence of Ψ translates into $\Psi(\vec{x},t) = \Psi(\vec{x})\delta(t)$, and we have

$$\begin{aligned} v_0 I_1^G(t) &= -\int_V\int_0^t \Psi(\vec{x})\delta(t-t')\frac{\partial\rho(\vec{x},t-t')}{\partial t'}\,\mathrm{d}^3x\,\mathrm{d}t'\,, \\ v_0 I_1^G(t) &= -\int_V \Psi(\vec{x})\frac{\partial\rho(\vec{x},t')}{\partial t}\,\mathrm{d}^3x\,, \\ I_1^G(t) &= -\frac{1}{v_0}\int_V \vec{E}_\Psi(\vec{x})\vec{j}_e(\vec{x},t)\,\mathrm{d}^3x\,. \end{aligned} \tag{A.11}$$

with $\vec{E}_\Psi(\vec{x}) = -\vec{\nabla}\Psi(\vec{x})$ and $\vec{\nabla}\vec{j}_e(\vec{x},t) = -\frac{\partial\rho_e(\vec{x},t)}{\partial t}$. One can see Ramo's theorem in eq. A.11.

In gaseous detectors the charge creation happens through ionisation, so a created electron is always accompanied by an ion and they both move in opposite directions. The charge density then becomes

$$\rho(\vec{x},t) = Q\Theta(t)\left\{\delta^3\left[\vec{x}-\vec{x}_1(t)\right] - \delta^3\left[\vec{x}-\vec{x}_2(t)\right]\right\} \tag{A.12}$$

with $\vec{x}_1(0) = \vec{x}_2(0)$. Using this charge density with eq. A.10 we get

$$I_1^G(t) = \frac{1}{v_0}\int_0^t\int_V \Psi(\vec{x}',t-t')\frac{\partial}{\partial t'}\left(Q\Theta(t')\left\{\delta^3\left[\vec{x'}-\vec{x'}_1(t')\right] - \delta^3\left[\vec{x'}-\vec{x'}_2(t')\right]\right\}\right)\mathrm{d}^3x'\,\mathrm{d}t',$$

$$\begin{aligned}I_1^G(t) = {} & \frac{Q}{v_0}\int_0^t\int_V \Psi(\vec{x}',t-t')\frac{\partial\Theta(t')}{\partial t'}\left(\delta^3\left[\vec{x'}-\vec{x'}_1(t')\right] - \delta^3\left[\vec{x'}-\vec{x'}_2(t')\right]\right)\mathrm{d}^3x'\,\mathrm{d}t' \\ & + \frac{Q}{v_0}\int_0^t\int_V \Psi(\vec{x}',t-t')\Theta(t')\frac{\partial}{\partial t'}\left(\delta^3\left[\vec{x'}-\vec{x'}_1(t')\right] - \delta^3\left[\vec{x'}-\vec{x'}_2(t')\right]\right)\mathrm{d}^3x'\,\mathrm{d}t'.\end{aligned}$$

As $\partial\Theta(t')/\partial t' = \delta t'$ the first half of the equation becomes

$$\frac{Q}{v_0}\int_V \Psi(\vec{x}',t)\left(\delta^3\left[\vec{x'}-\vec{x'}_1(0)\right] - \delta^3\left[\vec{x'}-\vec{x'}_2(0)\right]\right)\mathrm{d}^3x' = 0.$$

Using the property $\frac{\partial}{\partial t} = \frac{\partial}{\partial\vec{x}_1(t)}\cdot\frac{d\vec{x}_1(t)}{dt}$, the relation for $I_1^G(t)$ reads as

$$\begin{aligned}I_1^G(t) = {} & \frac{Q}{v_0}\int_0^t\int_V \Psi(\vec{x}',t-t')\frac{\partial}{\partial\vec{x}_1(t')}\left(\delta^3\left[\vec{x}'-\vec{x}_1(t')\right]\right)\dot{x}_1(t')\,\mathrm{d}^3x'\,\mathrm{d}t' \\ & - \frac{Q}{v_0}\int_0^t\int_V \Psi(\vec{x}',t-t')\frac{\partial}{\partial\vec{x}_2(t')}\left(\delta^3\left[\vec{x}'-\vec{x}_2(t')\right]\right)\dot{x}_2(t')\,\mathrm{d}^3x'\,\mathrm{d}t'.\end{aligned}$$

Using the properties of the Dirac δ distribution we have

$$\begin{aligned}I_1^G(t) = {} & \frac{Q}{v_0}\int_0^t\int_V \Psi(\vec{x}',t-t')\frac{\partial}{\partial\vec{x}_1(t')}\left(\delta^3\left[\vec{x}'-\vec{x}_1(t')\right]\right)\dot{x}_1(t')\,\mathrm{d}^3x'\,\mathrm{d}t' \\ & + \frac{Q}{v_0}\int_0^t\int_V \Psi(\vec{x}',t-t')\frac{\partial}{\partial\vec{x}_2(t')}\left(\delta^3\left[\vec{x}'-\vec{x}_2(t')\right]\right)\dot{x}_2(t')\,\mathrm{d}^3x'\,\mathrm{d}t'.\end{aligned}$$

Distributional derivative of the Dirac's delta gives $\delta'[\varphi] = -\delta[\varphi']$ where φ is a test function,

$$\begin{aligned}I_1^G(t) &= -\frac{Q}{v_0}\int_0^t\frac{\partial}{\partial\vec{x}_1(t')}\int_V \Psi(\vec{x}',t-t')\left(\delta^3\left[\vec{x}'-\vec{x}_1(t')\right]\right)\dot{x}_1(t')\,\mathrm{d}^3x'\,\mathrm{d}t' \\ &\quad -\frac{Q}{v_0}\int_0^t\frac{\partial}{\partial\vec{x}_2(t')}\int_V \Psi(\vec{x}',t-t')\left(\delta^3\left[\vec{x}'-\vec{x}_2(t')\right]\right)\dot{x}_2(t')\,\mathrm{d}^3x'\,\mathrm{d}t', \\ I_1^G(t) &= -\frac{Q}{v_0}\int_0^t\frac{\partial}{\partial\vec{x}_1(t')}\Psi(\vec{x}_1(t'),t-t')\dot{x}_1(t')\,\mathrm{d}t' - \frac{Q}{v_0}\int_0^t\frac{\partial}{\partial\vec{x}_2(t')}\Psi(\vec{x}_2(t'),t-t')\dot{x}_2(t')\,\mathrm{d}t'.\end{aligned}$$

With $\vec{E}_\Psi = -\vec{\nabla}\Psi$ we obtain the relation for the current induced by a moving charge composed of an electron and an ion. The induced signal is only due to the motion of the charges:

$$I_1^G(t) = \frac{Q}{v_0}\int_0^t E_\Psi(\vec{x}_1(t'),t-t')\dot{x}_1(t')\,\mathrm{d}t' + \frac{Q}{v_0}\int_0^t E_\Psi(\vec{x}_2(t'),t-t')\dot{x}_2(t')\,\mathrm{d}t'. \tag{A.13}$$

In gaseous detectors, the ions move very slowly in the gas: their drift velocity is negligible before that of electrons. In fact, the induced signals on RPC electrodes develop on two time-scale: first the fast ions induce charges on the electrodes (called the *fast signal*), then the ions will induce a signal on the cathode which develop much slower (called the *total signal*). So from eq A.13 the signals induced by an electron (fast) and an ion (total) moving in the gas are given by

$$
\begin{aligned}
I_{\text{fast}}(t) &= \tfrac{Q_e}{v_0} \int_0^t E_\Psi(\vec{x}_e(t'), t - t')\dot{x}_e(t')\,\mathrm{d}t'\,, && \text{(A.14)} \\
I_{\text{tot}}(t) &= \tfrac{Q}{v_0} \int_0^t E_\Psi(\vec{x}_i(t'), t - t')\dot{x}_i(t')\,\mathrm{d}t'\,. && \text{(A.15)}
\end{aligned}
$$

List of Figures

Bibliography

[1] G. Aad et al. "Observation of a new particle in the search for the Standard Model Higgs boson with the ATLAS detector at the LHC". In: *Physics Letters B* 716.1 (Sept. 2012), pp. 1–29. DOI: 10.1016/j.physletb.2012.08.020. arXiv: 1207.7214.

[2] S Abachi et al. "Search for high mass top quark production in pp-bar collisions at sqrt s=1.8 TeV." In: *Physical review letters* 74.13 (Mar. 1995), pp. 2422–2426. DOI: 10.1103/PhysRevLett.74.2422.

[3] M. Abbrescia, A. Colaleo, and G. Iaselli. "Progresses in the simulation of Resistive Plate Chambers in avalanche mode". In: *Nuclear Physics B- . . .* 78 (1999), pp. 459–464. DOI: 10.1016/S0920-5632(99)00587-3.

[4] M Abbrescia et al. "The simulation of resistive plate chambers in avalanche mode: charge spectra and efficiency". In: *Nuclear Instruments and Methods in Physics Research Section A: Accelerators, Spectrometers, Detectors and Associated Equipment* 431.3 (1999), pp. 413–427. DOI: 10.1016/S0168-9002(99)00374-5.

[5] F Abe et al. "Observation of Top Quark Production in p-barp Collisions with the Collider Detector at Fermilab." In: *Physical review letters* 74.14 (Apr. 1995), pp. 2626–2631. DOI: 10.1103/PhysRevLett.74.2626. arXiv: 9503002 [hep-ex].

[6] K. Abe et al. "Performance of glass RPC operated in streamer mode with SF 6 gas mixture". In: *Nuclear Instruments and Methods in Physics Research Section A: Accelerators, Spectrometers, Detectors and Associated Equipment* 455.2 (2000), pp. 397–404. DOI: 10.1016/S0168-9002(00)00518-0.

[7] W. W. M. Allison. "The physics of charged particle identification". In: *Experimental techniques in high energy physics*. 1987, pp. 371–418.

[8] W. W. M. Allison and J. H. Cobb. "Relativistic charged particle identification by energy loss". In: *Annual Review of Nuclear and Particle Science* 30.1 (1980), pp. 253–298. ISSN: 0163-8998. DOI: 10.1146/annurev.ns.30.120180.001345. URL: http://www.annualreviews.org/doi/pdf/10.1146/annurev.ns.30.120180.001345.

[9] J Apostolakis et al. "An implementation of ionisation energy loss in very thin absorbers for the GEANT4 simulation package". In: *Nuclear Instruments and Methods in Physics Research Section A: Accelerators, Spectrometers, Detectors and Associated Equipment* 453.3 (2000), pp. 597–605. DOI: 10.1016/S0168-9002(00)00457-5.

[10] Alan Astbury et al. *A 4 pi solid angle detector for the SPS used as a proton-antiproton collider at a centre of mass energy of 540 GeV*. Tech. rep. CERN, 1978.

[11] J. J. Aubert et al. "Experimental Observation of a Heavy Particle J". In: *Physical Review Letters* 33.23 (Dec. 1974), pp. 1404–1406. DOI: 10.1103/PhysRevLett.33.1404.

[12] J. -E. Augustin et al. "Discovery of a Narrow Resonance in e+e- Annihilation". In: *Physical Review Letters* 33.23 (Dec. 1974), pp. 1406–1408. DOI: 10.1103/PhysRevLett.33.1406.

[13] L. Benussi et al. "A study of HFO-1234ze (1,3,3,3-Tetrafluoropropene) as an eco-friendly replacement in RPC detectors". In: *arXiv* (May 2015). arXiv: 1505.01648.

[14] L. Benussi et al. "Properties of potential eco-friendly gas replacements for particle detectors in high-energy physics". In: *arXiv* (May 2015). arXiv: 1505.00701.

[15] H. Bethe. "Zur Theorie des Durchgangs schneller Korpuskularstrahlen durch Materie". In: *Annalen der Physik* 397.3 (1930), pp. 325–400. DOI: 10.1002/andp.19303970303.

[16] S. F. Biagi. "Monte Carlo simulation of electron drift and diffusion in counting gases under the influence of electric and magnetic fields". In: *Nuclear Instruments and Methods in Physics Research, Section A: Accelerators, Spectrometers, Detectors and Associated Equipment* 421.1-2 (1999), pp. 234–240. ISSN: 01689002. DOI: 10.1016/S0168-9002(98)01233-9.

[17] Hans Bichsel. "Straggling in thin silicon detectors". In: *Reviews of Modern Physics* 60.3 (July 1988), pp. 663–699. DOI: 10.1103/RevModPhys.60.663.

[18] S. Biswas et al. "Performances of linseed oil-free bakelite RPC prototypes with cosmic ray muons". In: *Nuclear Instruments and Methods in Physics Research, Section A: Accelerators, Spectrometers, Detectors and Associated Equipment* 602.3 (2009), pp. 749–753. ISSN: 01689002. DOI: 10.1016/j.nima.2008.12.131. arXiv: 0907.2976.

[19] Rene Brun and Fons Rademakers. "ROOT - An Object Oriented Data Analysis Framework". In: *Nucl. Inst. & Meth. in Phys. Res. A* 389 (1997), pp. 81–86. URL: http://root.cern.ch/.

[20] V. Buridon et al. "First results of the CALICE SDHCAL technological prototype". In: *Journal of Instrumentation* 11.04 (Apr. 2016), P04001–P04001. DOI: 10.1088/1748-0221/11/04/P04001. arXiv: 1602.02276. URL: http://arxiv.org/abs/1602.02276%20http://dx.doi.org/10.1088/1748-0221/11/04/P04001.

[21] P Camarri et al. "Streamer suppression with SF6 in RPCs operated in avalanche mode". In: *Nuclear Instruments and Methods in Physics Research Section A: Accelerators, Spectrometers, Detectors and Associated Equipment* 414.2 (1998), pp. 317–324. DOI: 10.1016/S0168-9002(98)00576-2.

[22] R Cardarelli, V Makeev, and R Santonico. “Avalanche and streamer mode operation of resistive plate chambers”. In: *Nuclear Instruments and Methods in Physics Research Section A: Accelerators, Spectrometers, Detectors and Associated Equipment* 382.3 (1996), pp. 470–474. DOI: `10.1016/S0168-9002(96)00811-X`.

[23] R. Cardarelli et al. “Progress in resistive plate counters”. In: *Nuclear Inst. and Methods in Physics Research, A* 263.1 (1988), pp. 20–25. DOI: `10.1016/0168-9002(88)91011-X`.

[24] E. Cerron Zeballos et al. “A new type of resistive plate chamber: The multigap RPC”. In: *Nuclear Instruments and Methods in Physics Research, Section A: Accelerators, Spectrometers, Detectors and Associated Equipment* 374.1 (1996), pp. 132–135. DOI: `10.1016/0168-9002(96)00158-1`.

[25] G. Charpak and F. Sauli. “The multistep avalanche chamber: A new high-rate, high-accuracy gaseous detector”. In: *Physics Letters B* 78.4 (Oct. 1978), pp. 523–528. ISSN: 03702693. DOI: `10.1016/0370-2693(78)90502-6`.

[26] G. Charpak et al. “The use of multiwire proportional counters to select and localize charged particles”. In: *Nuclear Instruments and Methods* 62.3 (July 1968), pp. 262–268. DOI: `10.1016/0029-554X(68)90371-6`.

[27] S. Chatrchyan et al. “Observation of a new boson at a mass of 125 GeV with the CMS experiment at the LHC”. In: *Physics Letters B* 716.1 (Sept. 2012), pp. 30–61. DOI: `10.1016/j.physletb.2012.08.021`. arXiv: `1207.7235`.

[28] G. Chiodini et al. “Measurements of drift velocity in the ATLAS RPC gas mixture”. In: *Nuclear Physics B - Proceedings Supplements* 158 (2006), pp. 133–136. DOI: `10.1016/j.nuclphysbps.2006.07.004`.

[29] S Colafranceschi et al. “Performance of the Gas Gain Monitoring system of the CMS RPC muon detector and effective working point fine tuning”. In: *Journal of Instrumentation* 7.12 (2012), P12004–P12004. DOI: `10.1088/1748-0221/7/12/P12004`.

[30] Jack Collins. *Construction of a Prototype Spark Chamber*. 2009.

[31] M Conversi and A Gozzini. “The “Hodoscope chamber”: a new instrument for nuclear research”. In: *Il Nuovo Cimento (1955-1965)* 2.1 (1955), pp. 189–191. DOI: `10.1007/BF02856027`.

[32] A H Cookson and T J Lewis. “Variations in the Townsend first ionization coefficient for gases”. In: *British Journal of Applied Physics* 17.11 (1966), pp. 1473–1481. DOI: `10.1088/0508-3443/17/11/312`.

[33] Van Toan Dao et al. “Numerical reproducibility, portability and performance of modern pseudo random number generators”. 2014.

[34] A. De Matteis and S. Pagnutti. “Long-range correlations in linear and nonlinear random number generators”. In: *Parallel Computing* 14.2 (1990), pp. 207–210. DOI: `10.1016/0167-8191(90)90108-L`.

[35] P. Fonte et al. “A dedicated setup for the measurement of the electron transport parameters in gases at large electric fields”. In: *Nuclear Instruments and Methods in Physics Research Section A: Accelerators, Spectrometers, Detectors and Associated Equipment* 613.1 (Jan. 2010), pp. 40–45. ISSN: 01689002. DOI: 10.1016/j.nima.2009.11.019. URL: http://linkinghub.elsevier.com/retrieve/pii/S016890020902169X.

[36] Vincent Français. *RPCSim*. 2016. URL: https://github.com/vincentFrancais/RPCSim.

[37] W. H. Furry. “On Fluctuation Phenomena in the Passage of High Energy Electrons through Lead”. In: *Physical Review* 52.6 (Sept. 1937), pp. 569–581. DOI: 10.1103/PhysRev.52.569.

[38] *GARFIELD framework*. URL: http://garfieldpp.web.cern.ch/garfieldpp/.

[39] Herald Genz. “Single electron detection in proportional gas counters”. In: *Nuclear Instruments and Methods* 112.1 (1973), pp. 83–90. DOI: 10.1016/0029-554X(73)90778-7.

[40] V.M. Grishin, V.K. Ermilova, and S.K. Kotelnikov. “Fast particle identification based on the relativistic increase of the threshold efficiency in multilayer proportional detectors”. In: *Nuclear Instruments and Methods in Physics Research Section A: Accelerators, Spectrometers, Detectors and Associated Equipment* 307.2-3 (Oct. 1991), pp. 273–278. DOI: 10.1016/0168-9002(91)90192-S.

[41] Claus Grupen and Boris Shwartz. *Particle detectors*. 2000, pp. 1003–1063. DOI: 10.1088/0034-4885/43/8/002.

[42] Hiroshi Haramoto et al. “Efficient Jump Ahead for F2-Linear Random Number Generators”. In: *INFORMS Journal on Computing* 20.3 (2008), pp. 385–390. DOI: 10.1287/ijoc.1070.0251.

[43] F.J. Hasert et al. “Observation of neutrino-like interactions without muon or electron in the Gargamelle neutrino experiment”. In: *Nuclear Physics B* 73.1 (Apr. 1974), pp. 1–22. DOI: 10.1016/0550-3213(74)90038-8.

[44] P. Hellekalek. “Don’t trust parallel Monte Carlo!” In: *Proceedings. Workshop on Parallel and Distributed Simulation* 28.1 (1998), pp. 82–89. DOI: 10.1109/PADS.1998.685273.

[45] S. W. Herb et al. “Observation of a dimuon resonance at 9.5 GeV in 400-GeV proton-nucleus collisions”. In: *Physical Review Letters* 39.5 (1977), pp. 252–255. ISSN: 00319007. DOI: 10.1103/PhysRevLett.39.252.

[46] T. Heubrandtner et al. “Static electric fields in an infinite plane condenser with one or three homogeneous layers”. In: *Nuclear Instruments and Methods in Physics Research Section A: Accelerators, Spectrometers, Detectors and Associated Equipment* 489.1 (2001), pp. 439–443. DOI: 10.1016/S0168-9002(02)00805-7. URL: https://cds.cern.ch/record/525925/files/open-2001-074.pdf.

[47] T. Heubrandtner et al. “Static electric fields in an infinite plane condenser with one or three homogeneous layers”. In: *Nuclear Instruments and Methods in Physics Research Section A: Accelerators, Spectrometers, Detectors and Associated Equipment* 489.1 (2002), pp. 439–443. DOI: https://doi.org/10.1016/S0168-9002(02)00805-7.

[48] David R C Hill. “Parallel Random Numbers, Simulation, and Reproducible Research”. In: *Computing in Science and Engineering* 17.4 (2015), pp. 66–71. ISSN: 15219615. DOI: 10.1109/MCSE.2015.79.

[49] David R. C. Hill and Imad Laktineh. *Private conversation.* 2016.

[50] David R C Hill et al. “Distribution of random streams for simulation practitioners”. In: *Concurrency Computation Practice and Experience* 25 (2013), pp. 1427–1442.

[51] W Hormann and G Derflinger. “The ACR method for generating normal random variables”. In: *Operations-Research-Spektrum* 12.3 (1990), pp. 181–185. ISSN: 304. DOI: 10.1007/BF01719718.

[52] Mitio Inokuti. “Inelastic Collisions of Fast Charged Particles with Atoms and Molecules—The Bethe Theory Revisited”. In: *Reviews of Modern Physics* 43.3 (July 1971), pp. 297–347. DOI: 10.1103/RevModPhys.43.297.

[53] Nuclear Instruments, P Schildt, and N Wermes. “An on-line track following microprocessor for the petra experiment tasso”. In: 178 (1980), pp. 571–579.

[54] International Commision on Radiation Units and Measurements. *ICRU Report 31: Average Energy Required To Produce An Ion Pair.* Tech. rep. 1979. URL: http://www.icru.org/home/reports/average-energy-required-to-produce-an-ion-pair-report-31.

[55] John David Jackson. *Classical electrodynamics.* Wiley, 1999. ISBN: 978-0-471-30932-1.

[56] A. Jash et al. “Effect of plate roughness on the field near RPC plates”. In: *J. Instrum.* 11.06 (June 2016), pp. C06010–C06010. DOI: 10.1088/1748-0221/11/06/C06010.

[57] William P. Jesse and John Sadauskis. “Alpha-Particle Ionization in Pure Gases and the Average Energy to Make an Ion Pair”. In: *Physical Review* 90.6 (June 1953), pp. 1120–1121. DOI: 10.1103/PhysRev.90.1120.

[58] Nabil Kemerchou. “Logiciel de g{é}n{é}ration de nombres al{é}atoires dans OpenCL”. PhD thesis. 2015.

[59] J W Keuffel. “Parallel-plate counters and the measurement of very small time intervals”. In: *PHYSICAL REVIEW.* Vol. 73. 5. AMERICAN PHYSICAL SOC ONE PHYSICS ELLIPSE, COLLEGE PK, MD 20740-3844 USA. 1948, p. 531.

[60] L. Khosravi Khorashad, A. Moshaii, and S. Hosseini. “Fast and total charges in a resistive plate chamber: A numerical approach”. In: *EPL (Europhysics Letters)* 96.4 (2011), p. 45002. DOI: 10.1209/0295-5075/96/45002.

[61] I. Kitayama et al. “Optical observation of discharge in resistive plate chamber”. In: *Nuclear Instruments and Methods in Physics Research Section A: Accelerators, Spectrometers, Detectors and Associated Equipment* 424.2 (1999), pp. 474–482. DOI: 10.1016/S0168-9002(98)01379-5.

[62] Pierre L’ Ecuyer. “Uniform random number generation”. In: *Annals of Operations Research* 1 (2006), pp. 93–137. DOI: 10.1002/9780470172445.ch4.

[63] Imad Laktineh. “Large size and fine time resolution RPC and RPC industrialization”. In: *talk at AIDA annual meeting* June (2016).

[64] L Landau. “On the energy loss of fast particles by ionization”. In: *Journal of Physics* (1944).

[65] L. D. Landau and E. M. Lifshitz. *Electrodynamics of Continuous Media*. 1960. DOI: `10.1119/1.1937882`.

[66] F. Lapique and F. Piuz. “Simulation of the Measurement By Primary Cluster Counting of the Energy Lost By a Relativistic Ionizing Particle in Argon.” In: *Nuclear instruments and methods* 175.2-3 (1980), pp. 297–318. DOI: `10.1016/0029-554X(80)90744-2`.

[67] P L'Ecuyer. “Fast combined multiple recursive generators with multipliers of the form a = \pm 2^{q} \pm 2^{r}”. In: *Proceedings of the 32nd conference on Winter* 1993 (2000), pp. 683–689.

[68] Pierre L'Ecuyer. “Random Number Generation with Multiple Streams for Sequential and Parallel Computing”. In: *Proceedings of the 2015 Winter Simulation Conference*. 2015, pp. 31–44. ISBN: 9781467397438. URL: `https://hal.inria.fr/hal-01240131`.

[69] Pierre L'Ecuyer. “Random numbers for simulation”. In: *Communications of the ACM* 33.10 (1990), pp. 85–97. DOI: `10.1145/84537.84555`. arXiv: `arXiv:1011.1669v3`.

[70] Pierre L'Ecuyer and Raymond Couture. “An implementation of the lattice and spectral tests for multiple recursive linear random number generators”. In: *INFORMS Journal on Computing* 9.2 (1997), pp. 206–217. DOI: `10.1287/ijoc.9.2.206`.

[71] Pierre L'Ecuyer and Peter Hellekalek. “Random Number Generators: Selection Criteria and Testing Random and Quasi-Random Point Sets.” In: *Lecture Notes in Statistics* 138 (1998), pp. 223–265.

[72] Pierre L'Ecuyer and Pierre L'Ecuyer. “Good parameters and implementations for combined multiple recursive random number generators”. In: *Operations Research* 47.1 (1999), pp. 158–164.

[73] Pierre L'Ecuyer and Richard Simard. “TestU01: A C Library for Empirical Testing of Random Number Generators”. In: *ACM Transactions on Mathematical Software* 33.4 (2007), 22–es. DOI: `10.1145/1268776.1268777`.

[74] Pierre L'Ecuyer et al. “An Object-Oriented Random-Number Package with Many Long Streams and Substreams”. In: *Operations Research* 50.6 (2002), pp. 1073–1075. DOI: `10.1287/opre.50.6.1073.358`.

[75] Pierre L'Ecuyer et al. “Random numbers for parallel computers: Requirements and methods, with emphasis on gpus”. In: *Mathematics and Computers in Simulation* (2015).

[76] Werner Legler. “Die statistik der elektronenlawinen in elektronegativen gasen, bei hohen feldstarken und bei grosser gasverstarkung”. In: *Zeitschrift f{ü}r Naturforsch. A* 16 (1960), pp. 253–261. DOI: `10.1515/zna-1961-0308`.

[77] Christian Lippmann. “Detector Physics of Resistive Plate Chambers”. In: 2003 (2003), p. 179.

[78] Christian Lippmann and Werner Riegler. "Space charge effects in Resistive Plate Chambers". In: *Nuclear Instruments and Methods in Physics Research, Section A: Accelerators, Spectrometers, Detectors and Associated Equipment* 517.1-3 (2004), pp. 54–76. ISSN: 01689002. DOI: 10.1016/j.nima.2003.08.174.

[79] Makoto Matsumoto. *SFMT web page*. URL: http://www.math.sci.hiroshima-u.ac.jp/%7B~%7Dm-mat/MT/SFMT/JUMP/index.html.

[80] Makoto Matsumoto and Yoshiharu Kurita. "Twisted GFSR generators". In: *ACM Transactions on Modeling and Computer Simulation* 2.3 (1992), pp. 179–194. DOI: 10.1145/146382.146383.

[81] Makoto Matsumoto and Takuji Nishimura. "Dynamic creation of pseudorandom number generators". In: *Monte Carlo and Quasi-Monte Carlo Methods* 1.1 (2000), pp. 56–69. DOI: 10.1017/CBO9781107415324.004. arXiv: arXiv:1011.1669v3.

[82] Makoto Matsumoto and Takuji Nishimura. "Mersenne-Twister: a 623-dimensionally equidistributed uniform pseudorandom number generator". In: *ACM Transactions on Modeling and Computer Simulations* (1998).

[83] Harald Niederreiter. "Quasi-Monte Carlo methods and pseudo-random numbers". In: *Bulletin of American Mathematical Society* 84.6 (1978), pp. 957–1041. DOI: 10.1090/S0002-9904-1978-14532-7.

[84] NIST. *X-Ray Mass Attenuation Coefficients*. URL: http://physics.nist.gov/PhysRefData/XrayMassCoef/tab1.html.

[85] K A Olive et al. "Review of Particle Physics". In: *Chin. Phys.* C38 (2014), p. 90001. DOI: 10.1088/1674-1137/38/9/090001.

[86] V. V. Parkhomchuck, Yu N. Pestov, and N. V. Petrovykh. "A spark counter with large area". In: *Nuclear Instruments and Methods* 93.2 (1971), pp. 269–270. DOI: 10.1016/0029-554X(71)90475-7.

[87] Robert Piessens et al. *QUADPACK: A subroutine package for automatic integration*. Vol. 1. Springer Science & Business Media, 2012.

[88] Simon Ramo. "Currents Induced by Electron Motion". In: *Proc. IRE* 27.9 (1939), pp. 584–585. DOI: 10.1109/JRPROC.1939.228757.

[89] Werner Riegler. "Induced signals in resistive plate chambers". In: *Nuclear Instruments and Methods in Physics Research Section A: Accelerators, Spectrometers, Detectors and Associated Equipment* 491.1 (2002), pp. 258–271. DOI: 10.1016/S0168-9002(02)01169-5.

[90] Werner Riegler, Christian Lippmann, and Rob Veenhof. "Detector physics and simulation of resistive plate chambers". In: *Nuclear Instruments and Methods in Physics Research, Section A: Accelerators, Spectrometers, Detectors and Associated Equipment* 500.1-3 (2003), pp. 144–162. DOI: 10.1016/S0168-9002(03)00337-1.

[91] Mutsuo Saito and Makoto Matsumoto. "SIMD-Oriented Fast Mersenne Twister: a 128-bit Pseudorandom Number Generator". In: *Monte Carlo and Quasi-Monte Carlo Methods 2006* (2008). Ed. by Alexander Keller, Stefan Heinrich, and Harald Niederreiter, pp. 607–622. DOI: 10.1007/978-3-540-74496-2_36. URL: http://dx.doi.org/10.1007/978-3-540-74496-2%7B%5C_%7D36.

[92] R. Santonico and R. Cardarelli. “Development of resistive plate counters”. In: *Nuclear Instruments and Methods* 187.2-3 (1981), pp. 377–380. ISSN: 0029554X. DOI: `10.1016/0029-554X(81)90363-3`.

[93] F. Sauli. “Principles of operation of multiwire proportional and drift chambers”. In: May (1977).

[94] Fabio Sauli. *Report 77-09:Principles of operation of multiwire proportional and drift chambers*. 1977. DOI: `10.5170/CERN-1977-009`.

[95] P Schweitzer. *HPCSim*. 2016.

[96] A Semak et al. “Properties of discharge in the narrow gap glass RPC”. In: *Nuclear Instruments and Methods in Physics Research Section A: Accelerators, Spectrometers, Detectors and Associated Equipment* 456.1 (2000), pp. 50–54. DOI: `10.1016/S0168-9002(00)00961-X`.

[97] I. B. Smirnov. “Modeling of ionization produced by fast charged particles in gases”. In: *Nuclear Instruments and Methods in Physics Research, Section A: Accelerators, Spectrometers, Detectors and Associated Equipment* 554.1-3 (2005), pp. 474–493. ISSN: 01689002. DOI: `10.1016/j.nima.2005.08.064`.

[98] Igor Smirnov. *HEED++ simulation program*. 2010. URL: `http://ismirnov.web.cern.ch/ismirnov/heed`.

[99] E A Uehling. “Penetration of Heavy Charged Particles in Matter”. In: *Annual Review of Nuclear Science* 4.1 (1954), pp. 315–350. DOI: `10.1146/annurev.ns.04.120154.001531`.